The University Of Sheffield.

NEW TOOLS FOR MODELLING SOIL-FILLED MASONRY ARCH BRIDGES

By

Michał Pytlos

Supervisors:
Dr Colin Smith
Professor Matthew Gilbert

A thesis submitted in partial fulfilment of the requirements for the degree of Doctor of Philosophy

The University of Sheffield
Department of Civil and Structural Engineering
October 2015

Abstract

This study is concerned with the development of new numerical and physical tools suitable for modelling soil-filled masonry arch bridges. Firstly, a novel modelling approach is presented which makes use of the Box2D rigid body physics engine, widely used in the computer games industry. A description of the simulation method implemented in Box2D is provided and it is shown that this tool is capable of accurately simulating disc and block interaction dynamics, and can successfully capture the critical state response of granular media. Four Box2D based computer programs, constituting a 'virtual laboratory', are presented and are shown to be capable of accurately simulating load tests to failure on both bare and soil-filled masonry arches. It is also demonstrated that the macro-scale properties of a virtual soil material, modelled as an assembly of randomly shaped polygons, are independent of the simulated scenario. Practical issues associated with the use of Box2D as a modelling tool are considered and advantages compared with the traditional distinct element method are discussed. Secondly, an innovative experimental facility developed by the author and suitable for testing medium-scale sand-filled masonry arch bridges is described. The test facility features a novel sand conveyance and pouring system which provides very good control over backfill properties and significantly speeds up the deposition process. Initial test results from the test facility are described and recommendations for future work are made.

Acknowledgements

Firstly, I would like to acknowledge my supervisory team of Dr Colin Smith and Professor Matthew Gilbert. Colin and Matthew have always been generous with their time, full of ideas and provided support and inspiration when it was needed.

I would like to thank the technical staff from the Department of Civil and Structural Engineering for their hard work in the development process of the experimental facility. In particular, I wish to acknowledge Dr Paul Bentley for his help in the development of the sand conveyance and pouring system and wiring of the instrumentation, Kieran Nash for fabricating the voussoirs, Chris Todd for help with the Kelsey actuator, Mark Foster, Alex Cargill and David Callaghan for their substantial help throughout the whole development process and Paul Blackbourn and Paul Osborne for their technical advice. Special thanks go to Martin Taylor for his participation in the crucial process of fine-tuning of the sand conveyance and pouring system, his enthusiasm and technical knowledge were of enormous help.

I would like to thank Sebastian Buccello, Richard Osborne and Nadine Fecht for their help in conducting the laboratory test.

I am grateful to the EPSRC for funding my PhD research for three years.

Finally, I would like to thank my family, and in particular my parents and my sister Marysia, for all their love and support over the years.

Contents

1. Introduction

There are over 70,000 highway and railway masonry arch spans in the UK. The main period of arch building in this country lasted from the second half of the 18th to the beginning of the 20th century when canal, railway and road infrastructures were subject to rapid expansion. There are relatively few masonry arch bridges built nowadays but the existing stock forms a vital part of the UK's national infrastructure.

Over the centuries masonry arch bridges have proven to be extremely versatile and sustainable structures, with many of them far surpassing the original design assumptions, both in terms of lifespan and in terms of load capacity. Yet, in order to cope with material deterioration and ever increasing demands on performance, the existing stock requires careful management. Specifically, considering the continuing crucial role of masonry arch bridges in the UK's transport networks, the large number of spans still in service, and the limited budgets available for repair and maintenance, it is very important that engineers have access to reliable assessment methods, capable of identifying which bridges require attention.

Masonry arch bridges have been the subject of research for well over two centuries, yet their behaviour is still not fully understood. In particular soil-arch interaction, three-dimensional effects and behaviour under cyclic loading require further investigation. The present research is concerned with the first of these issues, soil-arch interaction under quasi-static loading conditions.

1.1. Aims and objectives

The overall aim of the present work is to develop new physical and numerical modelling tools which facilitate in-depth study of the behaviour of soil-filled masonry arch bridges. In order to achieve this aim the following objectives were set:

(i) To develop a laboratory test rig capable of modelling quarter scale models of 3m span bridges being simultaneously tested at the University of Salford. The rig should allow collection of high quality data on soil kinematics and soil pressures, provide repeatable test results and allow the density of the (frictional) backfill materials employed to be varied.

(ii) To develop a numerical tool for the analysis of masonry arch bridges capable of modelling frictional backfill materials directly, offering the benefits associated with the well known distinct element method but without its main drawbacks.

(iii) To evaluate the performance of the newly developed tools from (i) and (ii) when used to model soil-filled masonry arch bridges.

1.2. Thesis structure

Chapter 2 provides background information that led to the stated aims and the objectives. The structural behaviour of masonry arch bridges is discussed, a short review of the current methods of analysis is given and the relevant physical studies conducted to date are summarized.

Chapters 3, 4 and 5 are concerned with a novel numerical tool for modelling masonry arch bridges backfilled with frictional soil. Chapter 3 provides a description of the simulation method and discusses the practical side of modelling. Results from a series of validation problems are also presented. Chapter 4 discusses modelling of soil. The adopted soil model is presented and results from two biaxial compression tests, designed to determine the macro-scale properties of virtual soil materials, are presented and discussed. Chapter 5 discusses modelling of bare and backfilled masonry arch bridges. Results from a series of tests designed to allow validation against limit analysis software programs are presented and the concept of a virtual laboratory is discussed. Techniques to determine the required accuracy settings, decrease runtime of simulations and determine the minimum required number of soil particles in the backfilled arch model are proposed and tested.

Chapter 6 presents the developed innovative facility for testing of sand-filled medium-scale models of masonry arch bridges. Results from a series of bare arch tests exploring the influence of compressive strength of joints on the behaviour of the arch are discussed. Sample results from a backfilled arch test are also presented.

Chapter 7 summarizes the outcomes and the key findings from the research presented. The recommendations for further work on, and with, the tools developed are given in Chapter 8.

2. Background

2.1. Structural behaviour of masonry arch bridges

2.1.1. Typical structural details

An overview of a single span square masonry arch bridge is shown in Figure 2.1. Due to the terrain conditions specific to a given site as well as the lack of design codes and material standards at the time of construction, UK masonry arch bridges vary considerably in shape, structural details and materials. From a statistical point of view the majority of railway masonry arch bridges are of brickwork with segmental profiles and consist of single or multiple spans below 10 metres (Page, 1993).

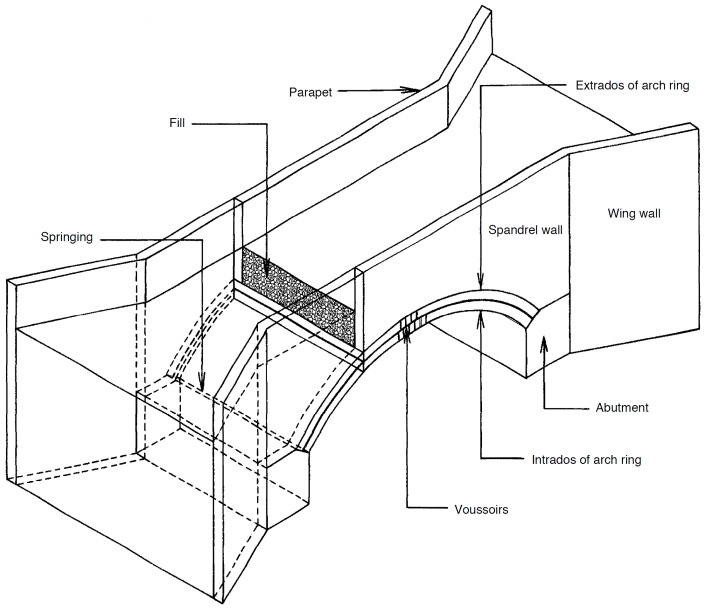

Figure 2.1.: General arrangement of a masonry arch bridge (after Hughes and Blackler (1997))

2.1.2. Arch barrel

The arch barrel is the main load bearing element of a masonry arch bridge. It is usually built either of stone or brickwork; the possible shapes include semicircle, circular segment, pointed arch, parabola, ellipse and a combination of a number of circular segments.

Stone barrels typically consist of a single ring. Stone units can be either square and dressed (ashlar) or irregular in shape and size (rubble). The latter material often gives a varying arch thickness.

Brickwork arch barrels usually consist of multiple concentric rings. Typical bonding styles are shown in Figure 2.2. Bridges in the UK were usually built using the stretcher bonding style (Melbourne et al., 2007).

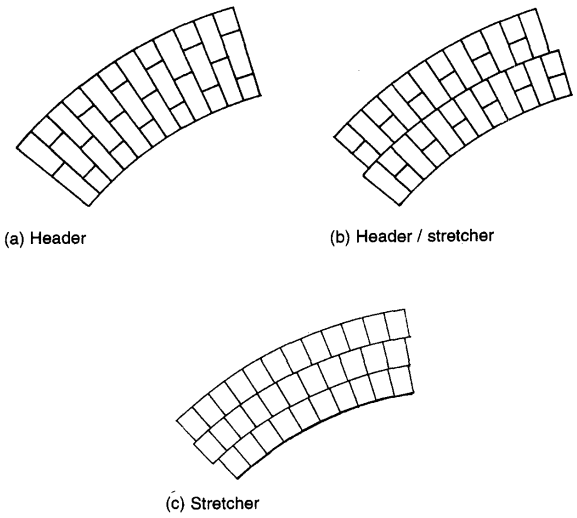

Figure 2.2.: Typical bonding styles (after Melbourne and Gilbert (1995))

Material

Masonry is essentially a collection of stiff and strong units bonded with a relatively weak and soft material. Due to its composite nature, it exhibits a complex anisotropic behaviour. Masonry is strong in compression and weak (with a brittle response) in tension. In shearing, once the bond between the mortar and the units is broken, it exhibits a frictional response.

Line of thrust

In masonry structures the internal forces are often visualized using a line of thrust, defined as the eccentricity of the compressive force (eccentricity = moment / axial force). If the line of thrust lies entirely within the masonry, the forces can be transmitted purely by compressive action. It cannot pass outside the cross section as this would mean that tensile forces are being developed. Assuming infinite compressive strength of the masonry, the limit occurs when the thrust line just touches the external surface of the masonry; the force is then transmitted at a strip of an infinitesimal width and the rest of the cross section is at zero stress. At this point a hinge is formed, allowing plastic bending of the structure. Figure 2.3 illustrates the concept of the line of thrust in an arch. It has to be noted that masonry arches are statically indeterminate structures and the actual line of thrust can be determined only at the point of failure.

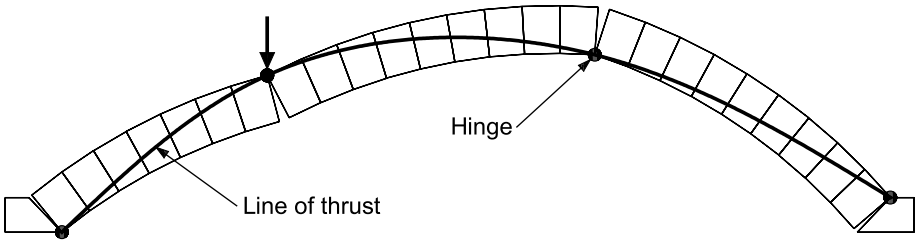

Figure 2.3.: Thrust line concept

Load response

In the load response of a masonry arch the material strength usually plays a secondary role. Compared to working stresses, compressive strength is usually very high and tensile strength very low. Under working stresses masonry arches behave approximately elastically, returning to their original shape upon unloading. Several failure modes are possible, with reduction to a hinged mechanism being the most common mode observed in both field and laboratory experiments. The failure modes described in literature (Hughes and Blackler (1997), McKibbins et al. (2006) and Gilbert (2007)) are listed below. Note that real failures of masonry arch bridges might involve a combination of the listed modes.

(i) Hinged mechanism

In a well proportioned arch, the line of thrust under the dead load lies close to the centre of the barrel thickness. The eccentricity of the line of thrust increases with increases in the external load, eventually causing hinges to form progressively. For a single span fixed ended arch, four hinges are required to form a mechanism. The critical load position depends on the geometry of the arch; it is close to the quarter span point for shallow arches and close to the third span point for deep arches. Assuming the configuration shown in Figure 2.4a, the first hinge usually forms under the load, the second around the three-quarter point and the last two close to the abutments. Under displacement-control loading the response is usually ductile (i.e. after reaching the ultimate load the structure is able to undergo relatively large deformations without significant loss of load carrying capacity). Four hinge failure mechanism was observed, for example, in the field tests to collapse on the Prestwood and Shinafoot bridges (Page (1987) and Page (1988) respectively) and in the test on a full scale model conducted at the Bolton Institute of Higher Education (Melbourne and Walker, 1990).

(ii) Hinges and sliding mechanism

An excessive lateral movement of the abutment may lead to a mechanism involving three hinges as shown in Figure 2.4c. In principle shallow arches are more prone to this type of failure as they produce greater horizontal thrust.

(iii) Shear

The ratio of shear to axial force in masonry arches is low and punching failure is therefore unlikely in a well designed and maintained structure. Punching failure may occur

as a result of substantial lateral movement of the abutment (see Figure 2.4b) or where loss of mortar leaves individual blocks unsupported by the axial thrust.

(iv) Snap-through

Snap-through is a hybrid failure mode. As the arch moves towards the mechanism state concentrated rotations at the hinge under the load produce local instability leading to a section of the arch snapping through; in order to occur, the snap-through failure mode requires crushing of the masonry at the hinges and/or elastic or inelastic shortening of the segments of masonry between the hinges. Shallow thin arches are considered more prone to this type of failure. This failure mode was observed, for example, in the field tests to collapse on the Torksey (shown in Figure 2.5) and Barlae bridges (Page (1988) and Page (1989) respectively).

(v) Crushing

Collapse initiated purely by overstressing of the material is very unlikely in masonry arches. Crushing failure of the masonry usually occurs in combination with the development of a hinged failure mechanism; as the eccentricity of the thrust line is increased, part of the cross-section which has to carry the axial thrust is reduced, reducing the load required to initiate a global hinged failure mechanism. Crushing of the masonry contributed to the failure modes observed, for example, in the field tests to collapse on the Bargower and Preston bridges (Hendry et al. (1986) and Page (1987) respectively).

(vi) Ring-separation

In multi-ring arches built using stretcher bonded brickwork shear stresses between the adjacent rings are carried only by the mortar joints. This makes the barrel prone to the separation of the individual rings. In case of ring-separation the structure will behave more like a stack of thin arches rather than a unit and have a reduced load carrying capacity. An example of the hinge failure mechanism with ring separation is shown in Figure 2.4d. Note that ring-separation is usually a brittle phenomenon. For more information on this failure mode see e.g. Melbourne and Gilbert (1995).

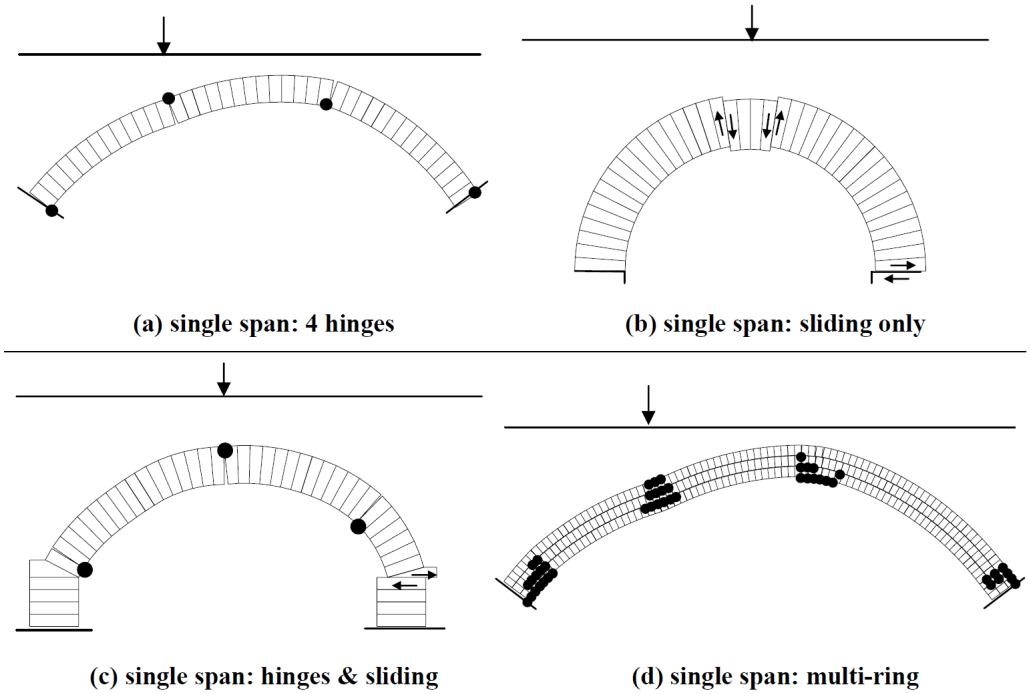

Figure 2.4.: Selection of potential failure modes of a single span arch (after LimitState (2011))

Figure 2.5.: Snap-through failure mode - Torksey bridge (after Page (1988))

2.1.3. Spandrel walls

The main function of the spandrel walls is to laterally contain the backfill. From a structural point of view spandrel walls increase the stability of the structure by: (i) imposing an additional, relatively uniform, load on the arch barrel, ii) constraining arch barrel movements

and (iii) interaction with the backfill. These favourable effects are however, usually ignored in the analysis. This is because the effect of (ii) is arguably often lost in practice due to the separation from the barrel and (i) and (iii) are three-dimensional effects which are difficult to quantify and model.

Instability of spandrel walls is a common problem affecting masonry arch bridges (McKibbins et al., 2006). Spandrel walls need to resist lateral forces, transferred through the backfill, from dead load, live load and, during freezing conditions, generated by swelling of the backfill; possible failure modes include toppling, sliding and splitting of the arch ring in the longitudinal direction.

2.1.4. Backfill

The presence of backfill has a significant influence on the behaviour of a masonry arch bridge; it was shown in laboratory experiments that it can increase the ultimate load bearing capacity of an arch bridge by as much as a factor of 10 (Smith et al., 2004). Aside from the increased stability due to the additional weight of the structure, the main mechanisms of interaction with the arch are dispersal of the applied loading and restraint to the arch barrel movement caused by mobilization of passive soil pressures.

Load dispersal in different types of soil is a generic geotechnical problem and its detailed consideration is beyond the scope of the present study (practical issues associated with quantifying this effect are discussed briefly in the section on methods of analysis).

Passive soil pressures are mobilized in a similar way in masonry arch bridges as they are in retaining walls. Consider a single span arch failing in the four hinge mechanism, as shown in Figure 2.6. Prior to loading, the arch is undeformed and the soil is in an at-rest condition, with zero strains (if the backfill is compacted, some stresses will be 'locked in'). Once the load is applied, the loaded side of the arch moves away from the soil and active soil pressures will be mobilized. On the unloaded side, the arch moves into the soil and passive soil pressures will be mobilized. Quantifying the passive soil pressures at the soil-structure interface is not straightforward. The classical earth pressure theories allow calculation of the passive soil pressures in frictional soils at failure but the values obtained cannot be used directly in the analysis of masonry arch bridges. The main problem is that full passive pressures are not usually mobilized. This is because arch barrel deformations corresponding to the peak strength of the bridge usually do not lead to soil strains which are large enough to mobilize peak passive soil pressures. The mobilization level depends not only on the amount of movement of the barrel but also on the soil type and and on its density (e.g. see Fang et al. (2002)). Quantifying the active soil pressures is usually relatively simple on the other hand, because much smaller strains are required to mobilize them fully.

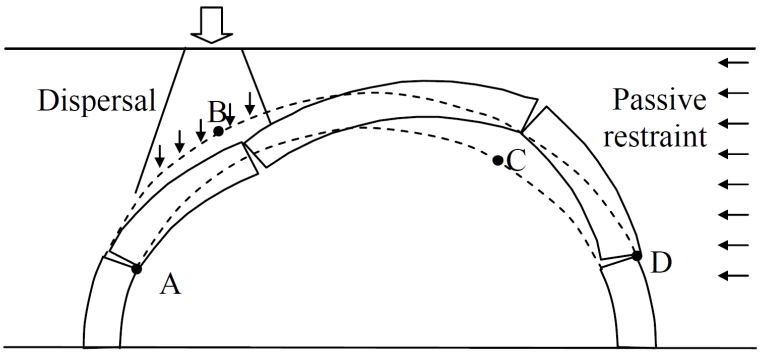

Figure 2.6.: Mobilization of soil passive pressures (after LimitState (2011))

Backfill materials

In the periods when most masonry arch bridges were constructed, backfill was regarded mainly as a means of providing a level road or rail surface. As a result masonry arch bridges are often backfilled with material that was readily available at the time of construction, including anything from ash to concrete (McKibbins et al., 2006). Callaway (2007) compiled a list of backfill materials reported in the literature; for a group of 43 bridges sand, clay, gravel and rubble were the most common backfill materials.

2.2. Methods of analysis

Considering that masonry arch bridges are rarely built nowadays, the purpose of a structural analysis is usually to assess the load carrying capacity of an existing structure. If the structure has to be repaired or strengthened, the additional task is to determine the best method of doing this.

The behaviour of masonry arch bridges is complex and it is not possible to describe it mathematically as a problem with a closed-form solution; there are, however, several modelling approaches available. They vary in cost, complexity and the extent to which they are capable of capturing the actual behaviour of the structure. The choice of the most appropriate modeling approach depends on the particular bridge being assessed; the following factors should be considered:

(i) **Cost:** there are over 70,000 masonry arch spans in the UK alone. With such a large number of structures requiring assessment, the cost of an analysis is an important factor to consider.

(ii) **Input parameters:** the material properties of masonry arch bridges have to be established, rather than defined through a manufacturing process. Obtaining some of these properties is expensive and difficult. Moreover, the quantity and quality of such data will never be perfect and additional sensitivity studies might be required.

(iii) **Accuracy:** the behaviour of a masonry arch bridge is complex and modelling all of its aspects is not feasible in practice. It is therefore very important to know what the

chosen method does and does not take into account and where the possible sources of inaccuracy are, e.g. in the form of empirical factors or high sensitivity to the quality of the input data.

(iv) **Flexibility:** more general methods of analysis allow the user to incorporate more details, such as complex geometry, defects or more refined material models. This allows one to understand the behaviour of the structure better, for example by performing sensitivity studies.

A selection of the methods of analysis available for the assessment of masonry arch bridges is presented below. The list is intended to be representative rather than exhaustive. Note that for all methods of analysis commonly used in practice it is usual to neglect spandrel walls and to model the structure as a two-dimensional plane-strain problem.

2.2.1. MEXE

MEXE is a semi-empirical assessment method, developed during and just after the second world war by the Military Engineering Experimental Establishment, used to estimate the service load capacity of masonry arch bridges. The method evolved from the work undertaken by Pippard and colleagues in the 1930s (Pippard et al., 1936). The researchers demonstrated by experiment that, until the mechanism is formed, voussoir arch ribs behave elastically and that, in this range and under certain assumptions, Castigliano's energy methods can be used to calculate the stress levels in the arch rib due to the load effects.

The method uses a nomograph to calculate the provisional axle load which is then modified with a series of factors in order to obtain the maximum axle load the bridge can carry safely. The nomograph is based on the elastic analysis of an arch used in conjunction with the results of full-scale field tests undertaken by the Building Research Station (Wang and Melbourne, 2010); the assumptions of the elastic analysis are as follows: the arch contains two pins formed at the abutments, is of parabolic shape, has span to rise ratio of 4, is loaded at the crown and the final criterion is the limiting value of the compressive stress in the arch. The fill density is assumed to be the same as the density of masonry and its strength is ignored.

In the assessment code BA16/97 (Highways Agency, 2001*a*) the input parameters for the nomograph are the arch span and the sum of the ring thickness and the backfill height above the crown. There are five modifying factors which take into account the following properties of the bridge: the actual span to rise ratio of the arch, the actual shape of the arch, the properties of the masonry units and of the backfill, the thickness and condition of the masonry joints and the overall condition of the structure.

A computer version of the MEXE method has also been developed which removes some of the limitations of the nomograph approach, namely: the shape of the arch is modelled directly; the loading position, the backfill density and the masonry compressive strength can be specified; the load dispersal model is improved.

The results of a MEXE assessment are generally considered to be conservative (McKibbins et al., 2006); possible exceptions include: small span arches (the method appears to be

calibrated as to be most accurate in the assessment of mid-range spans of about 12m and as a result, when compared to the Pippard's elastic method, it significantly overestimates the permissible axle loads of bridges spanning less than 5m (Wang et al., 2013)), arches where the cover of the crown is greater than the ring thickness (the method does not distinguish between these two parameters and instead uses their sum, the total crown thickness, as the input), multi-ring brickwork arches where ring separation is suspected (this defect is not specifically mentioned in the MEXE method (McKibbins et al., 2006)) and misshapen arches. For more information on the MEXE method see e.g. Wang and Melbourne (2010) or Page (1993).

Cost: MEXE is the simplest and cheapest tool for analysis of masonry arch bridges.

Input parameters: For the nomograph version, the only input parameters required are the geometry of the structure and qualitative description of the material properties.

Accuracy: The load capacity obtained using the MEXE method can only be considered to be a rough estimate. Firstly, masonry arch bridges are statically indeterminate structures and the equilibrium state considered in any elastic analysis may not be the actual state. Secondly, the method assumes that the arch fails in compression whilst retaining its original geometry; the most common failure mode, a hinged mechanism, is not considered directly. Moreover, the method is oblivious to the shear strength of masonry and any failure mode involving sliding of the masonry blocks is not catered for. Thirdly, the theoretical background of the material and joint factors remains unknown. As it stands these factors can only be treated as a very crude tool to take into account the material properties into the analysis. Finally, the strength of backfill and therefore the beneficial influence of the passive earth pressures is not modelled. Whilst it is a safe assumption, such simplification might lead to a significant underestimation of the bearing capacity of the structure.

Flexibility: Because of its semi-empirical nature, MEXE offers very limited flexibility in modelling. It can be used only to estimate load carrying capacity and gives no information on stresses, strains or the critical mode of failure of the structure. The method is intended for single span arches, spanning less than 18m which are not flat or appreciably deformed (Highways Agency, 2001*a*). Some researchers argue that the applicability of MEXE should be limited even more as it might overestimate the load carrying capacity of short span bridges (Wang et al., 2013).

2.2.2. Rigid-block analysis

The rigid-block analysis method (Gilbert and Melbourne, 1994) is the most popular limit analysis approach used in the assessment of masonry arch bridges. It is perhaps best to first introduce the concept of the limit analysis before discussing the specifics of the rigid-block method.

Limit analysis is an analysis approach which, based on a set of theorems, directly determines the collapse load of a structure under consideration. In the context of masonry arch

bridges, limit analysis is based on the plastic theorems which can be formulated as follows:

(i) The lower bound (safe) theorem: If an equilibrium between the internal and external loads can be found which nowhere violates the yield criterion, the structure will not fail.

(ii) The upper bound (unsafe) theorem: If in any postulated mechanism of the structure the work done by the external loads is greater than the work done in plastic energy dissipation, the structure will collapse.

In the classical limit analysis of masonry arches (Heyman, 1966) only a hinged failure mechanism is considered and the material yield conditions for the masonry are as follows:

(i) Zero tensile strength

(ii) Infinite compressive strength; based on the assumption that the stress levels involved are low compared to the actual compressive strength of the masonry

(iii) Infinite shear strength i.e. the masonry blocks cannot slide upon each other

In the rigid-block method the masonry is discretized into a series of rigid blocks and the problem is posed in the kinematic form (upper bound). In LimitState:RING (LimitState, 2014*a*), a widely used software program utilizing the rigid-block method, the critical failure mechanism and the failure load are then found using a linear programming optimization technique. The method can take into account the actual compressive (Gilbert, 1998) and shear (Gilbert et al., 2006) strength of the masonry, the latter in the from of friction between the blocks, allowing for mechanisms involving crushing and sliding. The soil-structure interaction is modelled indirectly, i.e. the dispersion of live loads using truncated Boussinesq or uniform distribution models and the passive soil pressures using one-dimensional bar elements with empirical modification factors designed to account for additional effects not represented by the simple model employed, including dependency of the mobilized pressures on the strains (LimitState, 2014*b*).

Cost: With the readily available software the analysis is quick and simple. If the default material properties are used, the cost in terms of time is only marginally higher than for the MEXE method.

Input parameters: The geometry of the structure and basic material properties are required to run the analysis. The material properties include the density of the masonry and the backfill, the compressive strength of the masonry blocks, the coefficient of friction for the masonry, the cohesion and angle of friction for the soil backfill and an empirical mobilization factor for modelling of the passive soil pressures.

Accuracy: For a masonry arch without backfill and unusual defects the rigid-block method gives an accurate estimation of the load carrying capacity (e.g. see Appendix G in LimitState (2014*b*)). The major limitation of the method lies in the approach to modelling the soil-structure interaction. Firstly, as mentioned before, the soil is modelled indirectly. Secondly, the mobilization of soil passive pressures is strain dependant and, as in any limit

analysis approach, empirical mobilization factors have to be used. There is nothing wrong with the use of empirical factors per se but there is insufficient laboratory data to cover different simulation scenarios; also use of a single global mobilization factor provides a rather crude approximation of real soil behaviour. Regarding the masonry, the method is not recommended for structures where stress-related failures are of concern, i.e. long span and/or flat arches. Also, as pointed out by Gilbert (2007), it is potentially unsafe if brittle fracture is likely to play an important factor.

Flexibility: The method is intended for non-flat single and multi-span masonry arch bridges with short to medium span lengths (LimitState, 2014*b*). It automatically determines the critical failure mode and can be used for a basic sensitivity study. Strengthening in the form of reinforcement can also be modelled.

2.2.3. Other limit analysis methods

In the context of soil-arch interaction, it is worth mentioning the discontinuity layout optimization and finite element limit analysis approaches. Both approaches are capable of modelling soil directly, e.g. masonry arch bridges are modelled using each of these methods respectively in Gilbert et al. (2010) and Cavicchi and Gambarotta (2005). Although it is a step forward when compared to the rigid-block method, accurate modelling of the passive soil pressures still requires the use of empirical mobilization factors.

2.2.4. Elasto-plastic finite element

The basic concept of any finite element (FE) approach is to treat the model as a continuum and to discretize this in order to approximate its global behaviour. The geometry of the structure is divided into a number of subregions or elements of a simple shape connected at discrete points called nodes. The unknown function, u_i^e, over each element is approximated through a function of its nodal values of the system unknowns, u_i^j, from:

$$u_i^e = \sum_{j=1}^{M} N_{ij} u_i^j \tag{2.1}$$

where N_{ij} is the shape function and M is the order of the element. The global partial differential equation describing the problem is then approximated with:

$$\sum_{i=1}^{N} [K_{ij}^e]\{u_j^e\} = \sum_{i=1}^{N} \{f_i^e\} \tag{2.2}$$

where $[K_{ij}^e]$ is the coefficient matrix, $\{u_j^e\}$ is the vector containing the unknown values of the nodal variables and $\{f_i^e\}$ is the vector containing body forces and boundary conditions (mathematical formulation after Jing (2003)).

The elasto-plastic finite element analysis involves the use of an iterative solution strategy. The live load is applied incrementally and at each iteration, Equation 2.2 is solved and

the normal and shear stresses at the nodes are compared with the material yield criteria. If the stresses are below the failure criteria, the element behaves elastically. If a yield criterion is violated, the element behaves in a perfectly plastic manner. If a sufficient number of elements have yielded to develop a mechanism, the structure fails.

The elasto-plastic finite element modelling of masonry arch bridges is discussed for example in Choo et al. (1991). Modelling soil with this method is a generic geotechnical problem; for more information see e.g. Griffiths and Lane (1999).

Cost: Some of the input parameters can be expensive and difficult to obtain. Considerable amount of time and expertise is also usually required to create a model and evaluate the results; this makes the method suited more for analysis of particularly complicated problems rather than routine assessment.

Input parameters: Apart from the geometry of the structure and strength of the materials, knowledge of their elastic properties is also required. Assuming the simplest model, the additional properties when compared to the rigid-block method are the Young's modulus and Poisson's ratio for the masonry and the backfill and the dilation angle if frictional soil is being modelled.

Accuracy:The method is capable of modelling the exact geometry of the structure, its defects and the soil-structure interaction. Its accuracy however, can be very sensitive to the quality of the input data, e.g. see the analysis of a masonry arch bridge described by Ponniah et al. (1997). In this case the FE model showed significantly higher stress levels in the soil and at the soil-structure interface when compared to the physical test measurements. This was attributed to the difference in stiffness between the model and the real soil-arch system. Considering that the structure was newly built and the information on its properties must have been much better than for a typical masonry arch bridge in the field, it is a useful reminder that high accuracy of an FE analysis should not be taken for granted.

Regarding soil, as pointed out by Cundall (2001), all continuum constitutive models are phenomenological, i.e. the stress-strain relations used in the model are not based on physical laws but are chosen to match to the response observed in the laboratory. The elasto-plastic model is a fairly simplistic approximation of real soil behaviour, derived usually from a simple shear or triaxial test, and the analyst should be aware of that. Some finite element material models are better at mimicking soil behaviour but they usually require the use of invented, often non-physical, parameters.

Another issue is the stability of the simulation. Because of the displacement compatibility condition, large local deformations, which are usually present in the failure mechanisms of masonry arch bridges, can sometimes break the simulation.

Flexibility: The finite element method is the most popular numerical method of analysis used in engineering, mainly due to its versatility. In case of masonry arch bridges it permits a very detailed model of features of the structure to be developed, and allows in-depth sensitivity analyses and experiments with various repair or strengthening options to be performed if required.

2.2.5. Distinct element method

The distinct element method (Cundall and Strack, 1979) is a discrete element method (DEM) approach with applications mainly in rock mechanics, soil mechanics and granular materials. The main concept of DEM is to model the problem domain as an assemblage of discrete bodies and simulate their dynamic interaction using a time-stepping scheme. The contact patterns in DEM are continuously changing; the bodies are allowed to detach and form new contacts in each time step. Interaction between bodies is governed by the contact model. In the distinct element method the contact model is based on the penalty method. In a simulation, the free body motion is governed by the Newton-Euler equations; if two bodies come into contact, force displacement laws are used to add forces to the system to limit interpenetration and to simulate friction. In soil mechanics the particles are usually modelled as rigid bodies (e.g. PFC2D and PFC3D codes) whilst in rock mechanics the blocks are often allowed to deform (e.g. UDEC and 3DEC codes). In the context of masonry arch bridges, the main advantages of DEM compared to FE are (i) its ability to model large local deformations without encountering numerical stability problems, and (ii) in case of granular backfill, its potential ability to model the material directly, without the need for constitutive models.

The distinct element method has been used in the analysis of masonry arch bridges, for example by Thavalingam et al. (2001) and Tóth et al. (2009); the former work was done with the particle code PFC3D and the latter with UDEC.

Cost: If stability of a bare arch is considered, the analysis is quick. If backfill is to be modelled as an assembly of large number of rigid bodies, the analysis becomes computationally very expensive, rendering the approach not useful in practice.

Input parameters: Geometric properties of the structure. Assuming rigid bodies, the basic material properties are specified for each body in terms of density, cohesion, shear stiffness and normal stiffness. Additional properties in form of the contact and global damping are also required to ensure stability of the simulation. In practice most of the input parameters do not represent real physical properties of the structure but are instead 'tuned' in order to achieve the desired macro-level behaviour (O'Sullivan, 2011).

Accuracy: The method can be considered accurate in determining the stability of a bare arch comprised of rigid blocks. The accuracy in modelling the strength of masonry depends on the scheme used to model the deformability. Regarding the modelling of frictional soil, the method is capable of capturing many features of the macro-scale behaviour (O'Sullivan, 2015), but it requires 'tuning' of model parameters in order to achieve this. However, the aim of modelling masonry arch bridges is not to replicate the known behaviour of the structure but rather to predict it; in this context the distinct element method may not be a reliable tool.

Flexibility: Discrete element methods permit modelling of any problem geometry. They can be combined with continuum methods such as FE, if structural strength of masonry is of concern. They can accommodate large local deformations and do not rely on soil constitutive

models. Unfortunately, with regards to modelling soil the benefits are rather theoretical at the moment due to the accuracy and speed issues outlined above.

2.2.6. Assessment in practice

In practice a multi-level assessment procedure is usually employed. The primary assessment tools used are currently MEXE and limit analysis methods. Only if the bridge has unusual geometry, long span, is significantly skewed or damaged, or fails the basic analysis, are more complex methods such as elasto-plastic finite elements employed. See e.g. McKibbins et al. (2006) for more details on the multi-level assessment approach.

2.2.7. Limitations of current methods of analysis

In the context of soil-structure interaction, currently there is no good method to model the backfill. On the one hand limit analysis approaches require use of empirical mobilization factors and therefore rely on scarce experimental test results. On the other hand elasto-plastic finite element approaches rely heavily on the availability of accurate material characterization data, which is difficult to obtain in practice. Note that in a masonry arch bridge analysis, use of an accurate value for the backfill stiffness is perhaps even more important than in most typical geotechnical problems because the capacity of the arch peaks before that of the backfill. DEM appears to be a good solution for the systems with purely frictional backfill materials but current accuracy and speed limitations arguably render it not useful in practice.

2.3. Physical modelling

The main purpose of physical modelling is to provide validation data for use in analysis models. This section briefly discusses masonry arch bridge physical modelling studies reported in the literature, focusing particularly on aspects relevant to soil-structure interaction.

2.3.1. Full scale tests

Field tests

In 1980s a series of eight tests to collapse on redundant masonry arch bridges was conducted by the Transport Research Laboratory (TRL). The bridges varied in structural details but the majority were below 10m span (7), segmental (6), square (5) and had either non-cohesive backfill (4) or a mixture of cohesive and non-cohesive backfill materials (4). All tested systems included not only the barrel, abutments and backfill but also the spandrel walls, sub-base material and surfacing layer. The backfill pressures and the backfill kinematics were not recorded. Although, of limited potential for validation of the analytical models, the tests provided a qualitative overview of the behaviour of masonry arch bridges in their full complexity. Test results were used to justify limiting the serviceability load to half of the ultimate failure load in the assessment code BD21/01 (Highways Agency, 2001*b*). For more

details on these tests see Hendry et al. (1985), Hendry et al. (1986), Page (1987), Page (1988) and Page (1989) .

Bolton tests

In 1990s a series of full-scale tests on soil-filled masonry arch bridges was conducted at the Bolton Institute. Four tests on 3m span and three tests on 5m span bridges were performed. The arch bridges were segmental with span to rise ratio of 4:1 and square. All bridges were backfilled with crushed limestone. However, the tests were primarily designed to investigate the ring separation phenomenon rather than soil-structure interaction. The models featured spandrel walls and the only information about the backfill movements was registered by the cameras above the test chamber. Soil pressures on the extrados and within the soil mass were measured but their interpretation is difficult (firstly, the presence of the spandrel walls makes the soil-structure interaction much more complicated and secondly, neither soil kinematics nor information on the repeatability of the readings is available). For more details on these tests see e.g. Melbourne and Gilbert (1995).

Salford tests

The most notable series of full scale tests investigating the soil-structure interaction in masonry arch bridges was conducted at the University of Salford in 2000s. The 3m span bridge models were segmental with span to rise ratio of 4:1 and square. The tests were conducted in plane-strain conditions. Spandrel walls were not featured in the models. Instead, the backfill was contained directly between transparent, low-friction side walls of the test chamber. A total of six tests were conducted; the models incorporated various backfill materials: three tests involved the use of crushed limestone, two tests clay and one test ‘hoggin’, a cohesive-frictional material widely used in the East of England. The tests with ‘hoggin’ and clay had also a near surface layer of crushed limestone to prevent a local soil failure. Apart from the barrel deformations, the soil pressures at the extrados and the soil kinematics were also captured throughout the tests (see Smith et al. (2006) for a detailed description of the test chamber). The results from these tests were used for validation of e.g. the rigid-block method (LimitState, 2014*b*) and the discontinuity layout optimization method (Gilbert et al., 2010).

2.3.2. Model scale tests

Full scale tests are very expensive and time consuming; for these reasons it is usually not feasible to perform repeat tests, to check for repeatability. It is also not usually practical to perform in-depth parameter studies. The alternative is to use small scale testing. In general, it is accepted that scaled models can indicate the behaviour of the full scale prototypes and under certain conditions predict their failure load. The main problem in scaled models is that the stress levels are much lower compared to the prototypes, thus for example the crushing strength of the masonry is not modelled correctly and any parts of the system relying on

cohesion (e.g. mortar joints or cohesive soil), will effectively be much stronger. The stress-strain response of frictional backfill materials is usually linear in the stress range considered, and therefore poses no problem in small scale modelling. For more information on small scale geotechnical modelling see e.g. Wood (2004)

Edinburgh tests

An extensive study of soil-structure interaction in masonry arch bridges using scaled models was conducted in Edinburgh in the early 1990s. In total, 88 tests on model arches were conducted. The arches were square and had a span of 700 mm which is close to the quarter-scale of the 3m span Salford and Bolton barrels. Two arch geometries were modelled, one semicircular and the other segmental with 4:1 span to rise ratio. All model bridges were backfilled with silica sand; the sub-base material and the surfacing were not featured in the models. Similarly to the Salford tests, the models had no spandrel walls and the backfill was contained directly between the side walls of the test chamber. The tests were conducted under close to plane-strain conditions. The voussoirs were made of timber and there was no jointing material between them. The soil kinematics were recorded throughout the tests with a camera; unfortunately, the relatively primitive photographic technology available at the time and the lack of data on soil pressures, meant that only observations on the general patterns of soil movement could be made. The main tested parameters were the backfill height above the crown and the load position; there was also a small study on the effect of backfill density on the collapse load but the density variation achieved was very small. In all the tests a local bearing failure of the backfill occurred prior to the collapse of the arch (note that local bearing failure is unlikely in real bridges since they usually feature a strong near-surface layer and if possible, local bearing failure should be prevented in laboratory tests since it changes the subsequent soil-structure interaction to some degree). The repeatability of the tests, in terms of the failure load, was within $\pm$14%. The study showed that the presence of backfill significantly contributed to the load capacity of the bridge; based on the results it can also be concluded that: (i) the critical load position for the semicircular arch, measured from the mid-span, was between 0.15 and 0.35 of the span and appeared to be independent of the backfill height, (ii) the critical load position for the arch with span to rise ratio of 4, measured from the mid-span, was between 0.23 and 0.4 of the span and appeared to move towards the mid-span as the backfill height increased and (iii) the density of backfill had significant influence on the load capacity of the arch-soil system. For more information on this test series see Fairfield and Ponniah (1994).

Sheffield tests

Masonry arch bridge soil-structure interaction studies were also conducted at the University of Sheffield in the 2000s. The test chamber used had similar capabilities to the one used in the Edinburgh tests series, though was smaller. The bridge models were segmental with span to rise ratio of 76:17, square and had a span of 380 mm. The voussoirs were made of acrylic and there was no jointing material between them. The bridge was backfilled with

silica sand. The models did not feature sub-base material, surfacing or spandrel walls. The backfill was contained between acrylic walls. The soil kinematics were recorded with a camera; no information on the soil pressures was collected. The tests were conducted under close to plane-strain conditions. The researchers managed to isolate the effects of load distribution and passive pressure development on the collapse load. Although the results are relevant only to one backfill type and only with the density as used in the tests, they provide useful validation data for analytical models of masonry arch bridges with cohesionless backfill material. For more information on this test series see e.g. Callaway et al. (2012) and Callaway (2007).

Also, using the same basic testing rig, it is also worth mentioning the study on the effect of flooding on the collapse load undertaken by Hulet et al. (2006).

2.3.3. Centrifuge tests

Centrifuge testing allows the use of small models of bridges to represent full scale prototypes without the problem of stress scaling. Centrifuge increases the apparent density of materials by centrifugal acceleration; e.g. a 1/4 scale model tested at the centrifugal acceleration of 4g will experience same stress levels as the full scale prototype. This allows correct modelling of the material strength of both the masonry and the cohesive backfill materials (for more information on geotechnical modelling using a centrifuge see e.g. Wood (2004)). Compared to the scaled 1g modelling, centrifuge testing offers better representation of the real structures but at a cost. Firstly, the tests are much more expensive and time consuming; secondly, it is an option only for institutions with the access to large centrifuge facility; thirdly, obtaining high quality data on the soil kinematics is problematic; fourthly, constructing very small model bridges under 1g conditions, particularly the masonry elements, is difficult and may not lead to representative material properties; finally, the model has to fit within the centrifuge strongbox. The last condition usually either forces the model to be very small or limits the space for the soil wedge to form on the passive side.

Cardiff tests

A series of centrifuge tests on soil-filled masonry arch bridges was conducted at Cardiff University in the early 2000s; the study is described in Burroughs et al. (2002). The bridge models were square and had span of 500 mm. Two geometries were modelled, one segmental with span to rise ratio of 4:1 and the other semicircular. The barrel consisted of 3 rings laid in stretcher bonding style, with brick units cut from full scale bricks and bonded with mortar joints. The arches were backfilled with graded granular limestone. The models did not feature sub-base material, surfacing or spandrel walls. The tests were conducted under close to plane-strain conditions. The soil pressures at the extrados were measured with miniature pressure sensors cast into the brick units. The soil kinematics were also captured but the results were not used in the published study. The model bridges were first loaded by a roller (14 passes), simulating a given axle load, and then tested to failure with load applied via a strip footing. The main focus of this test series was the development of passive earth

pressures with arch movement. The rolling load caused additional compaction of the backfill (and as a result increased its stiffness); no damage to the bridge models was reported. Considering the response in the strip loading phase of the test, the readings from the pressure sensors indicated that locally passive soil pressures were fully mobilized at relatively low radial deflections of the barrel. On the other hand, globally, passive soil pressures reached a maximum of only about a third of the theoretical values calculated from the Rankine soil pressure theory. This behaviour is hard to explain without a good quality data on the soil kinematics. It also has to be noted that soil pressure measurement, especially at this scale, requires special consideration due to the phenomena of, for example, soil arching or point loading which may affect the readings (see Weiler and Kulhawy (1982) for more details); this was not discussed by the authors.

Earlier tests on masonry arch bridges using this facility are described e.g. in Hughes et al. (1998) and Davies et al. (1998).

2.4. Knowledge gap

Physical studies on soil-structure interaction conducted to date, provide basic validation data for analytical models but are hardly exhaustive. There is a need for a test series featuring:

(i) various backfill types, i.e. a representative frictional backfill material(s), clay and well characterized mixture of cohesive and non-cohesive materials. The tests with frictional backfill should study the effect of the material density on the overall behaviour of the system.

(ii) good quality data on soil kinematics and soil pressures, that can be cross referenced.

(iii) repeatability checks.

Based on this knowledge gap and on the limitations of the current methods of analysis summarized in Section 2.2.7 it was decided that the overall aim of this study will be to develop new physical and numerical tools for the study of soil-filled masonry arch bridges, and specifically to:

(i) Develop a rig, capable of modelling quarter scale models of the 3m span bridges tested at the University of Salford. The rig should: allow collection of high quality data on soil kinematics and soil pressures, provide high test repeatability and allow the density of the frictional backfill materials to be varied.

(ii) Develop a numerical tool for the analysis of masonry arch bridges capable of modelling frictional backfill materials directly, ideally in the manner similar to the DEM approach but without its main limitations.

(iii) Test the performance of the newly developed tools from (i) and (ii) in modelling masonry arch bridges.

3. Box2D physics engine

The purpose of this chapter is to describe and validate a novel method of analysis with potential to be used in the assessment of masonry arch bridges with frictional backfill. The method is a combination of simulation techniques stemming from the field of computer science, brought together by Erin Catto in the Box2D physics engine.

3.1. Method description

Box2D is a program for two-dimensional simulation of dynamic interaction between discrete bodies. The continuous motion of bodies is discretized over the time domain and the simulation progressed using a time-stepping scheme. Each time step can be viewed as a subproblem where the task is to first calculate the rate of change of movement and then update the variables describing the state of each body. Objects are idealized as rigid bodies. The free body motion is governed by the Newton-Euler equations. When two or more bodies come into contact the equations of motion are augmented in order to incorporate friction and prevent bodies from inter-penetration; this is achieved via the contact model.

Whereas a traditional DEM code based on the distinct element method (Cundall and Strack, 1979) uses a penalty based contact model, in Box2D a constraint based contact model is used, which is more akin to the 'contact dynamics' approach considered by Jean (1999) and Radjai and Richefeu (2009). This can be considered to be the main difference between Box2D and traditional DEM approaches.

The information available in the literature does not contain full in depth description of the simulation method used in Box2D. For this reason the underlying concepts and the simulation cycle are described below. For information on the simulation method provided by Erin Catto, the author of Box2D, see Catto (2006), Catto (2009), Catto (2014) and the source code. For general information on the simulation of rigid bodies see e.g. Baraff (1997*a*), Baraff (1997*b*) and Bender et al. (2012).

3.1.1. A bigger picture: physics engines

Box2D is a physics engine. Physics engines are physics-based animation tools used in the computer games and film industries. The employed simulation techniques might vary considerably between different physics engines; considering rigid body simulation, a good overview was provided by Erleben (2005), and, more recently, by Bender et al. (2014). For games the simulation needs to be real-time; thus traditionally physics engines favour speed, robustness and stability over accuracy. There is however a demand for more physical realism in video games and simulation methods are continually being improved; as it will be shown

in this chapter, the accuracy can sometimes match or even beat the existing methods used in the field of engineering. The original motivation for the study of the potential of physics engines as modelling tools for masonry arch bridges came from the good results of the simulations of masonry walls with the Box2D physics engine (Catto, 2011) and the Bullet physics engine (Coumanns, 2012) described in the technical report LimitState (2013).

Physics engines are usually available in the form of a generic numerical library; often a lot of work is required before the given engine can be used for modelling of particular problems. For this reason, it was decided to focus on one physics engine and study it thoroughly rather than testing several ones but to a lesser depth. A list of commercial and open-source physics engines is provided by Bender et al. (2012). Box2D was considered to be the best choice for the following reasons: (i) it was proven previously to accurately model an assembly of rigid blocks (LimitState, 2013), (ii) it is two-dimensional which makes the analysis much simpler and fits the widely accepted approach to modelling of masonry arch bridges and (iii) it is open-source, has an active community of users and is still being improved.

3.1.2. Rigid body

A rigid body is an idealized solid body in which deformations are neglected i.e. the distance between any two points on the body is constant regardless of the forces acting on the body.

A rigid body is defined in terms of: (i) the geometrical description of its shape in the local space (in a simulation, in addition to the world space, every rigid body has its own local space with a local coordinate system) and (ii) its density. Based on these properties, the body mass m and the moment of inertia about the origin point of the local coordinate system I_0 can be computed. The origin point of the local coordinate system is taken as the position of the center of mass of the body. The state of the body defined with the position of the center of mass $\mathbf{x}$ in world space, linear velocity of the center of mass $\mathbf{v}$, rotation of the body around the center of mass Ω and angular velocity ω.

The state of any point on the body can be calculated using the body state variables. Consider an arbitrary point P on the body defined with the position $\mathbf{p}_0$ in the local space. The position of the point in the world space is calculated from:

$$\mathbf{p} = \mathbf{x} + \mathbf{R}\mathbf{p}_0 \tag{3.1}$$

where $\mathbf{R}$ is the two-dimensional rotation matrix. In the cartesian coordinate system Equation 3.1 has the following form:

$$\mathbf{p} = \begin{bmatrix} p_x \\ p_y \end{bmatrix} = \begin{bmatrix} x_x \\ x_y \end{bmatrix} + \begin{bmatrix} \cos(\Omega) & -\sin(\Omega) \\ \sin(\Omega) & \cos(\Omega) \end{bmatrix} \begin{bmatrix} p_{0x} \\ p_{0y} \end{bmatrix} \tag{3.2}$$

The linear velocity of the point P is calculated from:

$$\dot{\mathbf{p}} = \mathbf{v} + \omega \mathbf{r}^{\perp} \tag{3.3}$$

where $\mathbf{r} = \mathbf{p} - \mathbf{x}$ and $\perp$ is the perp operator which takes a vector and rotates it counterclockwise by 90 degrees.

3.1.3. Unconstrained motion

Simulation of the free body motion from time t to time $t + \Delta t$ is carried out in the following steps:

(i) Calculate the total external force $\mathbf{F}(t)$ and the total external torque $\tau(t)$ acting on the body:

$$\mathbf{F}(t) = \sum_{i=1}^{n} \mathbf{F}_i \tag{3.4}$$

$$\tau(t) = \sum_{i=1}^{n} \tau_i = \sum_{i=1}^{n} (\mathbf{f}_i - \mathbf{x}(t))^{\perp} \cdot \mathbf{F}_i \tag{3.5}$$

where $\mathbf{f}_i$ is the point of application of the force $\mathbf{F}_i$ in world space.

(ii) Calculate the new velocities:

$$\mathbf{v}(t + \Delta t) = \mathbf{v}(t) + \Delta t \frac{\mathbf{F}(t)}{m} \tag{3.6}$$

$$\omega(t + \Delta t) = \omega(t) + \Delta t \frac{\tau(t)}{I_0} \tag{3.7}$$

(iii) Calculate the new position variables:

$$\mathbf{x}(t + \Delta t) = \mathbf{x}(t) + \Delta t \mathbf{v}(t + \Delta t) \tag{3.8}$$

$$\Omega(t + \Delta t) = \Omega(t) + \Delta t \omega(t + \Delta t) \tag{3.9}$$

Note that in Box2D, the rate of change of the velocity is evaluated at time t whilst the rate of change of the position is evaluated at time $t + \Delta t$; this is the so called semi-implicit Euler integration scheme which is widely used in physics engines. Compared to the explicit Euler method, where both the rate of change of the velocity and the rate of change of the position are evaluated at time t, the semi-implicit Euler has the same low computational cost but is much more stable and preserves the energy of the system. See Catto (2015) for Erin Catto's comment on this subject.

3.1.4. Contact model

In a simulation involving interaction between bodies the equations of motion are augmented with constraints in order to incorporate friction and prevent bodies from inter-penetration. Contacts between bodies are detected in the collision detection phase of the simulation.

Consider two bodies in contact as shown in Figure 3.1b; the collision detection phase provides the following information about the contact: the contact normal unit vector $\hat{\mathbf{n}}$, the contact tangential unit vector $\hat{\mathbf{t}}$ and, for both bodies, the position of the contact point in the world space $\mathbf{p}_i$.

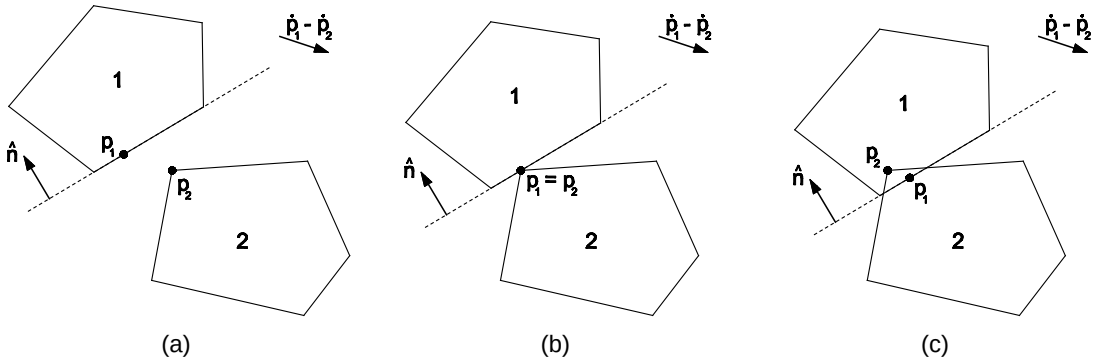

Figure 3.1.: Non-penetration constraint: (a) $C_n > 0$; (b) $C_n = 0$; (c) $C_n < 0$

Non-penetration constraint

The non-penetration constraint, graphically shown in Figure 3.1, is formulated as follows:

$$C_n = (\mathbf{p}_1 - \mathbf{p}_2) \cdot \hat{\mathbf{n}} \geq 0 \tag{3.10}$$

its derivative is:

$$\dot{C}_n = (\dot{\mathbf{p}}_1 - \dot{\mathbf{p}}_2) \cdot \hat{\mathbf{n}} + (\mathbf{p}_1 - \mathbf{p}_2) \cdot \dot{\hat{\mathbf{n}}} \geq 0 \tag{3.11}$$

assuming that, within a given tolerance, the points $\mathbf{p}_1$ and $\mathbf{p}_2$ are coincident, i.e. $(\mathbf{p}_1 - \mathbf{p}_2) = 0$, the derivative can be simplified to:

$$\dot{C}_n = (\dot{\mathbf{p}}_1 - \dot{\mathbf{p}}_2) \cdot \hat{\mathbf{n}} \geq 0 \tag{3.12}$$

The mechanism of the non-penetration constraint is conceptually described in Algorithm 1.

A formula for the scalar j_n is derived below; the steps to a large extent follow the three-dimensional derivation from Baraff (1997*b*). In the derivation below, the '$-$' superscript indicates a pre-impulse quantity and the '$+$' superscript indicates a post-impulse quantity.

Consider two bodies in contact with relative velocity at the contact point in the negative $\hat{\mathbf{n}}$ direction ($\dot{C}_n < 0$) as shown in Figure 3.1b. In order to satisfy the non-penetration constraint ($\dot{C}_n \geq 0$), the relative velocity has to be changed instantly; this is achieved with a quantity called impulse $\mathbf{J}$. In a time stepping scheme, an impulse is simply a force multiplied by the time step size ($\mathbf{J} = \mathbf{F}\Delta t$). Let j_n be the magnitude of the impulse J_n enforcing the non-penetration constraint:

$$J_n = j_n \hat{\mathbf{n}} \tag{3.13}$$

if $C_n \leq 0$ **then**
  bodies are in contact;
  if $\dot{C}_n < 0$ **then**
    this a colliding contact;
    compute an impulse j_n to instantly change the relative velocity $(\dot{\mathbf{p}}_1 - \dot{\mathbf{p}}_2) \cdot \hat{\mathbf{n}}$;
    if $|(\dot{\mathbf{p}}_1 - \dot{\mathbf{p}}_2) \cdot \hat{\mathbf{n}}| < v_{thr}$ **then**
      treat this as a resting contact;
      make $(\dot{\mathbf{p}}_1 - \dot{\mathbf{p}}_2) \cdot \hat{\mathbf{n}} = 0$ so there is no further inter-penetration;
    else if $|(\dot{\mathbf{p}}_1 - \dot{\mathbf{p}}_2) \cdot \hat{\mathbf{n}}| \geq v_{thr}$ **then**
      treat this as a colliding contact;
      use restitution law to compute the target, post-collision, relative velocity;
  else if $\dot{C}_n = 0$ **then**
    this is a resting contact;
    do nothing;
  else if $\dot{C}_n > 0$ **then**
    this is a separating contact;
    do nothing;
end

Algorithm 1: Mechanism of the non-penetration constraint where v_{thr} is a threshold magnitude of the relative velocity set by the user

The change in body velocities caused by J_n acting at the contact point is given by:

$$\Delta v = \frac{j_n \hat{\mathbf{n}}}{m} \tag{3.14}$$

$$\Delta \omega = \frac{\mathbf{r}^{\perp} \cdot j_n \hat{\mathbf{n}}}{I} \tag{3.15}$$

where $\mathbf{r}$ is the vector from the center of mass to the contact point ($\mathbf{r} = \mathbf{p} - \mathbf{x}$) and I is the moment of inertia about the contact point. Let $v_{rel,n}$ be the magnitude of the relative velocity in the normal collision direction:

$$v_{rel,n} = (\dot{\mathbf{p}}_1 - \dot{\mathbf{p}}_2) \cdot \hat{\mathbf{n}} \tag{3.16}$$

In a simulation, the velocity is defined for a body rather than for a contact point. The relation between the body velocities and the linear velocity of the contact point for the pre-impulse and the post-impulse state are given by:

$$\dot{\mathbf{p}}_i^- = \mathbf{v}_i^- + \omega^- \mathbf{r}_i^{\perp} \tag{3.17}$$

$$\dot{\mathbf{p}}_i^+ = \mathbf{v}_i^+ + \omega^+ \mathbf{r}_i^{\perp} \tag{3.18}$$

The post-impulse velocities of the body 1 are given by:

$$\mathbf{v}_1^+ = \mathbf{v}_1^- + \frac{j_n \hat{\mathbf{n}}}{m_1} \tag{3.19}$$

$$\omega_1^+ = \omega_1^- + \frac{\mathbf{r}_1^\perp \cdot j_n \hat{\mathbf{n}}}{I_1} \tag{3.20}$$

Combining 3.18 with 3.19, 3.20 and 3.17 yields:

$$\begin{aligned} \dot{\mathbf{p}}_1^+ &= \mathbf{v}_1^- + \frac{j_n \hat{\mathbf{n}}}{m_1} + \omega_1^- \mathbf{r}_1^\perp + \frac{\mathbf{r}_1^\perp \cdot j_n \hat{\mathbf{n}}}{I_1} \cdot \mathbf{r}_1 \\ &= \dot{\mathbf{p}}_1^- + j_n (\frac{\hat{\mathbf{n}}}{m_1} + \frac{\mathbf{r}_1^\perp \cdot \hat{\mathbf{n}}}{I_1} \cdot \mathbf{r}_1^\perp) \end{aligned} \tag{3.21}$$

An opposite impulse $-j_n \hat{\mathbf{n}}$ acts on the body 2, thus:

$$\dot{\mathbf{p}}_2^+ = \dot{\mathbf{p}}_2^- - j_n (\frac{\hat{\mathbf{n}}}{m_2} + \frac{\mathbf{r}_2^\perp \cdot \hat{\mathbf{n}}}{I_2} \cdot \mathbf{r}_2^\perp) \tag{3.22}$$

Substituting 3.21 and 3.22 into 3.16 yields:

$$\begin{aligned} v_{rel,n}^+ &= (\dot{\mathbf{p}}_1^+ - \dot{\mathbf{p}}_2^+) \cdot \hat{\mathbf{n}} \\ &= \hat{\mathbf{n}} \cdot (\dot{\mathbf{p}}_1^- + j_n (\frac{\hat{\mathbf{n}}}{m_1} + \frac{\mathbf{r}_1^\perp \cdot \hat{\mathbf{n}}}{I_1} \cdot \mathbf{r}_1^\perp) - \dot{\mathbf{p}}_2^- + j_n (\frac{\hat{\mathbf{n}}}{m_2} + \frac{\mathbf{r}_2^\perp \cdot \hat{\mathbf{n}}}{I_2} \cdot \mathbf{r}_2^\perp)) \end{aligned} \tag{3.23}$$

Regrouping, using 3.16 and taking into account that $\hat{\mathbf{n}} \cdot \hat{\mathbf{n}} = 1$:

$$\begin{aligned} v_{rel,n}^+ &= (\dot{\mathbf{p}}_1^- - \dot{\mathbf{p}}_2^-) \cdot \hat{\mathbf{n}} + j_n (\frac{\hat{\mathbf{n}}}{m_1} + \frac{\mathbf{r}_1^\perp \cdot \hat{\mathbf{n}}}{I_1} \cdot \mathbf{r}_1^\perp + \frac{\hat{\mathbf{n}}}{m_2} + \frac{\mathbf{r}_2^\perp \cdot \hat{\mathbf{n}}}{I_2} \cdot \mathbf{r}_2^\perp) \cdot \hat{\mathbf{n}} \\ &= v_{rel,n}^- + j_n (\frac{1}{m_1} + \frac{1}{m_2} + \frac{(\mathbf{r}_1^\perp \cdot \hat{\mathbf{n}})^2}{I_1} + \frac{(\mathbf{r}_2^\perp \cdot \hat{\mathbf{n}})^2}{I_2}) \end{aligned} \tag{3.24}$$

The j_n is then given by:

$$j_n = \frac{v_{rel,n}^+ - v_{rel,n}^-}{\frac{1}{m_1} + \frac{1}{m_2} + \frac{(\mathbf{r}_1^\perp \cdot \hat{\mathbf{n}})^2}{I_1} + \frac{(\mathbf{r}_2^\perp \cdot \hat{\mathbf{n}})^2}{I_2}} \tag{3.25}$$

In colliding contacts ($|v_{rel,n}| \geq |v_{thr}|$) the target post-impulse relative velocity $v_{rel,n}^+$ is calculated from:

$$v_{rel,n}^+ = -e v_{rel,n}^- \tag{3.26}$$

where e is the contact coefficient of restitution calculated from: $e = \max(e_1, e_2)$. Note that $v_{rel,n}^+$ is positive and therefore it satisfies the non-penetration constraint. Substituting 3.26 and 3.16 into 3.25 yields the final formula for j_n in colliding contacts:

$$j_n = \frac{-(e+1)(\dot{\mathbf{p}}_1^- - \dot{\mathbf{p}}_2^-) \cdot \hat{\mathbf{n}}}{\frac{1}{m_1} + \frac{1}{m_2} + \frac{(\mathbf{r}_1^\perp \cdot \hat{\mathbf{n}})^2}{I_1} + \frac{(\mathbf{r}_2^\perp \cdot \hat{\mathbf{n}})^2}{I_2}} \tag{3.27}$$

In resting contacts ($|v_{rel,n}| \leq |v_{thr}|$) the target post-impulse relative velocity is zero:

$$v_{rel,n}^+ = 0 \tag{3.28}$$

Substituting 3.28 and 3.16 into 3.25 yields the final formula for j_n in resting contacts:

$$j_n = \frac{-(\dot{\mathbf{p}}_1^- - \dot{\mathbf{p}}_2^-) \cdot \hat{\mathbf{n}}}{\frac{1}{m_1} + \frac{1}{m_2} + \frac{(\mathbf{r}_1^\perp \cdot \hat{\mathbf{n}})^2}{I_1} + \frac{(\mathbf{r}_2^\perp \cdot \hat{\mathbf{n}})^2}{I_2}} \tag{3.29}$$

Friction

If the bodies are in contact ($C_n \leq 0$) the tangential constraint, which is used in conjunction with the Coulomb friction law to simulate friction, is defined as:

$$C_t = (\mathbf{p}_1 - \mathbf{p}_2) \cdot \hat{\mathbf{t}} = 0 \tag{3.30}$$

At the velocity level it is:

$$\dot{C}_t = (\dot{\mathbf{p}}_1 - \dot{\mathbf{p}}_2) \cdot \hat{\mathbf{t}} + (\mathbf{p}_1 - \mathbf{p}_2) \cdot \dot{\hat{\mathbf{t}}} = 0 \tag{3.31}$$

Assuming $(\mathbf{p}_1 - \mathbf{p}_2) = 0$ the derivative can be simplified to:

$$\dot{C}_t = (\dot{\mathbf{p}}_1 - \dot{\mathbf{p}}_2) \cdot \hat{\mathbf{t}} = 0 \tag{3.32}$$

The solver works only with the constraint formulated at the velocity level. If the bodies are in contact and $\dot{C}_t \neq 0$ then an impulse j_t is computed to instantly zero the relative velocity $(\dot{\mathbf{p}}_1^- - \dot{\mathbf{p}}_2^-) \cdot \hat{\mathbf{t}}$. The formula for j_t is analogous to the formula for j_n in resting contacts:

$$j_t = \frac{-(\dot{\mathbf{p}}_1^- - \dot{\mathbf{p}}_2^-) \cdot \hat{\mathbf{t}}}{\frac{1}{m_1} + \frac{1}{m_2} + \frac{(\mathbf{r}_1^\perp \cdot \hat{\mathbf{t}})^2}{I_1} + \frac{(\mathbf{r}_2^\perp \cdot \hat{\mathbf{t}})^2}{I_2}} \tag{3.33}$$

where $\hat{\mathbf{t}}$ is in the direction of sliding. The impulse j_t is limited in magnitude by the Coulomb's friction law:

$$-\mu j_n \leq j_t \leq \mu j_n \tag{3.34}$$

where μ is the contact coefficient of friction calculated from: $\mu = \sqrt{\mu_1 \mu_2}$. If j_t calculated in Equation 3.33 is outside the friction limit, its value is reduced and the tangential constraint will not be satisfied (the bodies will slide).

3.1.5. Constrained motion

For clarity the complete simulation cycle from time t to time $t + \Delta t$ is described below. The '$-$' superscript indicates, as before, a pre-impulse quantity, the '$+$' superscript indicates a post friction impulse quantity and '$++$' superscript indicates a post non-penetration impulse quantity.

(i) Calculate the total external force $\mathbf{F}(t)$ and the total external torque $\tau(t)$ acting on each body:

$$\mathbf{F}(t) = \sum_{i=1}^{n} \mathbf{F}_i \tag{3.35}$$

$$\tau(t) = \sum_{i=1}^{n} \tau_i = \sum_{i=1}^{n} (\mathbf{f}_i - \mathbf{x})^{\perp} \cdot \mathbf{F}_i \tag{3.36}$$

(ii) Calculate the tentative velocities at time $t + \Delta t$ for each body:

$$\mathbf{v}^{-} = \mathbf{v}(t) + \Delta t \frac{\mathbf{F}(t)}{m} \tag{3.37}$$

$$\omega^{-} = \omega(t) + \Delta t \frac{\tau(t)}{I_0} \tag{3.38}$$

(iii) If a pair of bodies is in contact ($C_n \leq 0$) enforce the friction constraint. If $\dot{C}_t \neq 0$ compute an impulse j_t to zero the relative velocity $(\dot{\mathbf{p}}_1^{-} - \dot{\mathbf{p}}_2^{-}) \cdot \hat{\mathbf{t}}$ from:

$$j_t = \frac{-(\dot{\mathbf{p}}_1^{-} - \dot{\mathbf{p}}_2^{-}) \cdot \hat{\mathbf{t}}}{\frac{1}{m_1} + \frac{1}{m_2} + \frac{(\mathbf{r}_1^{\perp} \cdot \hat{\mathbf{t}})^2}{I_1} + \frac{(\mathbf{r}_2^{\perp} \cdot \hat{\mathbf{t}})^2}{I_2}} \tag{3.39}$$

The magnitude of the impulse is limited by the Coulomb's friction law:

$$-\mu j_n \leq j_t \leq \mu j_n \tag{3.40}$$

where j_n in the first iteration is 0 for a new contact or has value taken from the previous time step if the contact is persistent. In the subsequent iterations the value of j_n is known from the step (v) of the previous iteration.

(iv) Calculate the post-j_t velocities for each body:

$$\mathbf{v}_1^{+} = \mathbf{v}_1^{-} + \frac{j_t \hat{\mathbf{t}}}{m_1} \qquad \mathbf{v}_2^{+} = \mathbf{v}_2^{-} - \frac{j_t \hat{\mathbf{t}}}{m_2} \tag{3.41}$$

$$\omega_1^{+} = \omega_1^{-} + \frac{\mathbf{r}_1^{\perp} \cdot j_t \hat{\mathbf{t}}}{I_1} \qquad \omega_2^{+} = \omega_2^{-} - \frac{\mathbf{r}_2^{\perp} \cdot j_t \hat{\mathbf{t}}}{I_2} \tag{3.42}$$

where I_i is the moment of inertia about the contact point.

(v) If bodies are in contact ($C_n \leq 0$) enforce the non-penetration constraint. If $\dot{C} < 0$ compute an impulse j_n to change the relative velocity $(\dot{\mathbf{p}}_1^{+} - \dot{\mathbf{p}}_2^{+}) \cdot \hat{\mathbf{n}}$.

If $|(\dot{\mathbf{p}}_1^{+} - \dot{\mathbf{p}}_2^{+}) \cdot \hat{\mathbf{n}}| < v_{thr}$:

$$j_n = \frac{-(\dot{\mathbf{p}}_1^{+} - \dot{\mathbf{p}}_2^{+}) \cdot \hat{\mathbf{n}}}{\frac{1}{m_1} + \frac{1}{m_2} + \frac{(\mathbf{r}_1^{\perp} \cdot \hat{\mathbf{n}})^2}{I_1} + \frac{(\mathbf{r}_2^{\perp} \cdot \hat{\mathbf{n}})^2}{I_2}} \tag{3.43}$$

Else if $|(\dot{\mathbf{p}}_1^{+} - \dot{\mathbf{p}}_2^{+}) \cdot \hat{\mathbf{n}}| \geq v_{thr}$:

$$j_n = \frac{-(1+e)(\dot{\mathbf{p}}_1^{+} - \dot{\mathbf{p}}_2^{+}) \cdot \hat{\mathbf{n}}}{\frac{1}{m_1} + \frac{1}{m_2} + \frac{(\mathbf{r}_1^{\perp} \cdot \hat{\mathbf{n}})^2}{I_1} + \frac{(\mathbf{r}_2^{\perp} \cdot \hat{\mathbf{n}})^2}{I_2}} \tag{3.44}$$

(vi) Calculate the post-j_n velocities for each body:

$$\mathbf{v}_1^{++} = \mathbf{v}_1^{+} + \frac{j_n \hat{\mathbf{n}}}{m_1} \qquad \mathbf{v}_2^{++} = \mathbf{v}_2^{+} - \frac{j_n \hat{\mathbf{n}}}{m_2} \tag{3.45}$$

$$\omega_1^{++} = \omega_1^{+} + \frac{\mathbf{r}_1^{\perp} \cdot j_n \hat{\mathbf{n}}}{I_1} \qquad \omega_2^{++} = \omega_2^{+} - \frac{\mathbf{r}_2^{\perp} \cdot j_n \hat{\mathbf{n}}}{I_2} \tag{3.46}$$

(vii) Iterate over (iii)-(vi) until the stop condition is reached. The solver treats constraints sequentially, and in a model with multiple bodies in contact, multiple iterations are required in order to converge to an accurate global solution.

(viii) Calculate the new position variables for each body:

$$\mathbf{x}(t + \Delta t) = \mathbf{x}(t) + \Delta t \mathbf{v}(t + \Delta t) \tag{3.47}$$

$$\Omega(t + \Delta t) = \Omega(t) + \Delta t \omega(t + \Delta t) \tag{3.48}$$

where $\mathbf{v}(t + \Delta t)$ and $\omega(t + \Delta t)$ are the final velocities from the step (vii).

3.1.6. Position error

Body inter-penetrations due to numerical errors cannot be removed by the collision solver because the constraints are formulated at the velocity level. In resting contacts, over several time steps, this would lead to a position drift and the bodies would sink into each other. Box2D uses the following stabilization method to deal with this problem:

(i) For a pair of bodies in contact ($C_n \leq 0$) an additional constraint is formulated:

$$\dot{C}pos = (\dot{\mathbf{p}}_1^{\alpha} - \dot{\mathbf{p}}_2^{\alpha}) \cdot \hat{\mathbf{n}} - \beta_f (\mathbf{p}_1 - \mathbf{p}_2) \cdot \hat{\mathbf{n}} = 0 \tag{3.49}$$

where β_f is a scaling factor, set by default to 0.2, and $\dot{\mathbf{p}}_i^{\alpha}$ is the pseudo velocity, a quantity introduced into the simulation as a mean to remove the position error, of the contact point on the body i. In Box2D, a pseudo velocity is a non-physical quantity which resembles velocity in that it is a rate of change of position but differs from it in that it is not a part of the state of the body and does not persist across the time steps.

(ii) The corrective normal impulse is calculated from:

$$j_{pos} = \frac{-\beta_f (\mathbf{p}_1 - \mathbf{p}_2) \cdot \hat{\mathbf{n}}}{\frac{1}{m_1} + \frac{1}{m_2} + \frac{(\mathbf{r}_1^{\perp} \cdot \hat{\mathbf{n}})^2}{I_1} + \frac{(\mathbf{r}_2^{\perp} \cdot \hat{\mathbf{n}})^2}{I_2}} \tag{3.50}$$

(iii) The pseudo velocities for each body are calculated from:

$$\mathbf{v}_1^\alpha = \frac{j_{pos}\hat{\mathbf{n}}}{m_1} \qquad \mathbf{v}_2^\alpha = -\frac{j_{pos}\hat{\mathbf{n}}}{m_2} \tag{3.51}$$

$$\omega_1^\alpha = \frac{\mathbf{r}_1^\perp \cdot j_{pos}\hat{\mathbf{n}}}{I_1} \qquad \omega_2^\alpha = -\frac{\mathbf{r}_2^\perp \cdot j_{pos}\hat{\mathbf{n}}}{I_2} \tag{3.52}$$

Note that $\mathbf{v}^\alpha$ and ω^α are treated separately from the body velocities $\mathbf{v}(t)$ and $\omega(t)$, exist only for bodies in contact and are always zero at the beginning of a time step.

(iv) The position corrections are calculated from:

$$\mathbf{x}_c = \Delta t \mathbf{v}^\alpha \tag{3.53}$$

$$\Omega_c = \Delta t \omega^\alpha \tag{3.54}$$

3.1.7. Comparison with the distinct element method

The reason for conducting the research on Box2D was its potential ability to model the behaviour of frictional backfill materials in a manner similar to the traditional DEM approach but without its main limitations i.e. very long run-times and the need for tuning of the input parameters. Because of that it is worthy to highlight the differences between the simulation method implemented in Box2D and the most popular DEM approach in the field of geomechanics - the distinct element method (in the literature, also referred to as molecular dynamics). The general concept is similar: the bodies are modelled as rigid and their continuous motion is discretized over the time domain and the simulation progressed using a time-stepping scheme with the dynamics based on the Newton-Euler formulation. The key differences lie in the contact models and are discussed below.

Collision

Consider two colliding discs as shown in Figure 3.2a. Box2D does not care about what is happening during the collision but rather simulates just its outcome; this makes the physics, including friction, relatively simple at low or no cost since the information lost, such as elastic deformations or the time length of the collision, is not required in most applications. In Box2D the collision effectively lasts one time step regardless of the time step size. If the collision is frictionless, the normal and the tangential components of the post-collision relative velocity are known from basic physics; the latter does not change during a frictionless collision and the former is calculated from the coefficient of restitution which takes into account the energy converted to heat and plastic deformation in the real collision. The objective of the contact solver is then to calculate, from the law of conservation of momentum, the normal impulse (the tangential impulse must be equal to zero) that directly change the pre-collision relative velocity to the required post-collision value. The calculated impulse is equal to the integral of the force over time in the real collision event. If the collision does involve friction, the

tangential impulse is additionally calculated, and this is done in two steps; in the first step it is assumed that the friction is large enough to stop the relative movement in the tangential collision direction (i.e. the post-collision relative tangential velocity is zero) and the impulse calculated from the law of conservation of momentum. In the second step the calculated impulse is checked against the Coulomb's friction law and reduced if it falls outside the limit (the bodies will slide in that case).

In case of a frictionless collision, the distinct element method attempts to simulate the physics at a lower level than Box2D i.e. the actual collision event and not just the outcome . At the instant the colliding bodies start touching, as shown in Figure 3.2a, no contact force exists; the incremental force is started to be generated only in the next time step, graphically shown in Figure 3.2b, when the bodies overlap; the force increment in a given time step is calculated from:

$$\Delta F_n = k_n \Delta t (\dot{p}_1 - \dot{p}_2) \cdot \hat{\mathbf{n}} \tag{3.55}$$

where k_n is the normal contact stiffness and Δt is the time step size. If the simulation is to be accurate, the collision event must be several time steps long over which time the force and acceleration first gradually rise, proportional to the overlap, and then decrease once the relative velocity changes its direction and the overlap is gradually reduced. The energy converted to heat and plastic deformation in the real collision is usually simulated by adding normal damping to the contact model. Friction in the distinct element method is simulated by adding incremental force in the tangential collision direction; the force increment in a given step is calculated from:

$$\Delta F_t = k_t \Delta t (\dot{p}_1 - \dot{p}_2) \cdot \hat{\mathbf{t}} \tag{3.56}$$

where k_t is the tangential stiffness, and the total tangential force is limited in magnitude by the Coulomb's friction law. Additionally, stability of the simulation usually requires tangential damping to be added to the contact model. The workings of the friction model in the distinct element method clearly has nothing to do with real physics and the aim is simply to achieve the correct collision outcome i.e. the tangential post-collision velocity and the integral of the frictional force over the collision time.

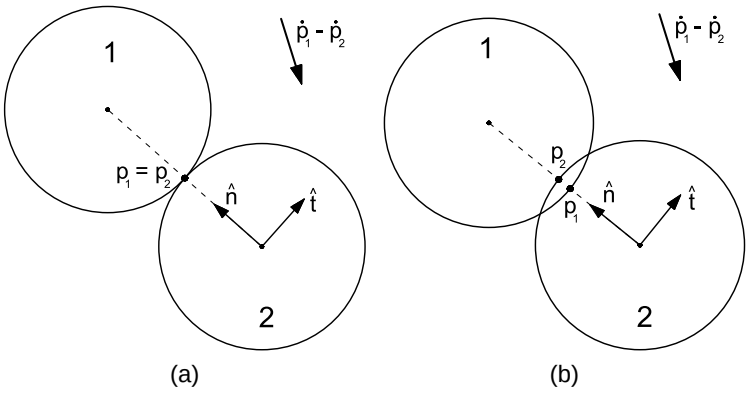

Figure 3.2.: Colliding discs: (a) $t = t_0$; (b) $t = t_0 + \Delta t$

Resting contact

Consider a disc resting on a flat surface as shown in Figure 3.3. The tentative velocity of the body produced by the gravity in a given time step is equal to the gravitational acceleration times the time step size. In resting contacts the objective of the contact solver is essentially the same as in case of a perfectly inelastic collision: generate a force or an impulse that will zero the relative velocity in the normal collision direction. Because of this, in both, Box2D and the distinct element method, resting contacts are treated in the same way as collisions.

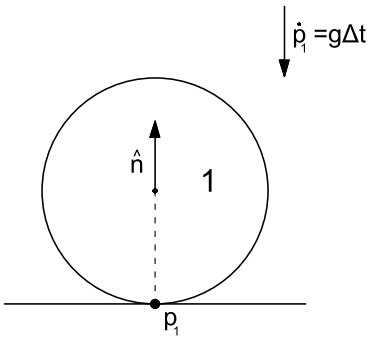

Figure 3.3.: Resting disc

Quasi-static simulations

This study is primarily concerned with statics and therefore all Box2D simulations of masonry arch bridges presented in this document are quasi-static in nature. In quasi-static simulations the correct relative velocity at a contact is zero in the normal direction (assuming no free-fall); same condition as in a perfectly inelastic collision (this means that in quasi-static simulations in Box2D the coefficient of friction has to be set to 0). The models involve multiple bodies and it is worth to discuss how each of the methods deal with the issue of multiple simultaneous contacts.

In Box2D, multiple contacts are solved one at a time in an arbitrary order and the correct global solution is achieved in an iterative process. In general, this approach is much faster than employing a global solver which would have to work on very large matrices (Catto, 2014) but it requires the user to decide on how many iterations are available in a time step to the solver. In general, the more bodies in a problem and the more dynamic the simulation in a given time step, the more iterations are required for good convergence but a proper guidance on this is required before Box2D can be considered to be a practical engineering tool (see Section 5.2.2 for a discussion on this matter).

In the distinct element method, the contacts are also solved one by one but the correct global solution is achieved by limiting the time step size rather than in an iterative process. The time step size depends on the size of bodies in the model, and is set at a level required to transfer the load just between the adjacent bodies and should not be any larger than this in order to prevent the elastic wave propagation further into the model (Thornton and Randall, 1988); in practice this means that the time step size has to be very low if simulation is to be stable.

Practical implications

The distinct element method is easy to implement and theoretically very fast because of the simple contact model. However, in practice, stability of the simulation dictates very small time step size and run-times are very long. Per time step, the contact model implemented in Box2D is computationally more expensive but it is still relatively fast because of its sequential nature. At the same time, the time step size can be much larger than in the distinct element method without the danger of numerical instability or unduly sacrificing accuracy. This means that the overall simulation time in Box2D can be potentially much lower than in the distinct element method .

Another advantage of the contact model implemented in Box2D is that, considering quasi-static simulations of frictional soils, there is only one relevant contact parameter, μ, and this directly represents a physical property of the soil being modelled. In contrast, in the distinct element method, apart from μ, the contact model uses several other parameters, namely the normal stiffness, tangential stiffness, contact damping and global damping, which in practice do not represent real physical properties of the bodies but are instead tuned in order to achieve the desired macro behaviour (O'Sullivan, 2011).

3.1.8. Comparison with Contact Dynamics

The simulation method implemented in Box2D has much more in common with Contact Dynamics (CD), a discrete element method developed by J.J. Moreau and M. Jean in 1980s and 1990s, than with the distinct element method. Contact Dynamics, described for example in Radjai and Richefeu (2009), has been successfully used to model granular media by various researchers (see for example Nouguier-Lehon et al. (2003), Staron and Hinch (2007) and Azéma and Radjaï (2010)) but in the geotechnical community the method is significantly less popular than the distinct element method (Krabbenhoft et al. (2012) speculate that the lack of popularity of CD is the result of the method being perceived as much more difficult to implement). The main modelling principles of CD shared with Box2D are as follows:

(i) bodies are modelled as perfectly rigid; the contacts are hard i.e. the body overlap is not allowed (if present, it is treated as an error)

(ii) dynamics is based on the Newton-Euler formulation with the simulation progressed using a time-stepping scheme (this is also common with the distinct element method)

(iii) contact laws are based on the Signorini conditions in the form shown in Figure 3.4a and on the Coulomb's friction law, graphically shown in Figure 3.4b.

Let f_n be the magnitude of the normal contact force F_n, let f_t be the magnitude of the tangential contact force F_t and let $v_{rel,t}$ be the magnitude of the relative velocity in the tangential collision direction:

$$v_{rel,t} = (\dot{\mathbf{p}}_1 - \dot{\mathbf{p}}_2) \cdot \hat{\mathbf{t}} \tag{3.57}$$

The Signorini conditions state that for a pair of bodies in contact: (a) $v_{rel,n}$ should be zero or separating, (b) F_n should be non-attractive and (c) if $v_{rel,n}$ is separating, the contact force is not generated.

The Coulomb's friction law bears the following meaning: (a) $-\mu f_n \leq f_t \leq \mu f_n$, (b) if $|f_t| < \mu f_n$, the contact is sticking ($v_{rel,t} = 0$), (c) if $|f_t| = \mu f_n$, the contact is sliding ($|v_{rel,t}| > 0$) or sticking and (d) F_t acts in the direction opposite to sliding.

(iv) contact laws are in the form of constraints formed at the velocity level; accelerations are not computed and forces are replaced with impulses in the simulation; the body motion is non-smooth (collisions result in velocity jumps)

(v) multiple simultaneous contacts are resolved iteratively; in a given iteration, contacts are solved sequentially in a random order

The main difference between the methods lies in the integration approach adopted; Box2D uses the semi-implicit Euler integration method whilst CD employs a fully implicit integration scheme. Another major difference is that in CD an additional contact parameter, the tangential coefficient of restitution, e_t, is introduced; $e_t \in [-1, 1]$ and acts as a weight in the formula for the mean-relative-tangential velocity in a given time step:

$$\overline{v}_{rel,t} = \frac{v_{rel,t}(t + \Delta t) + e_t v_{rel,t}(t)}{1 + |e_t|} \tag{3.58}$$

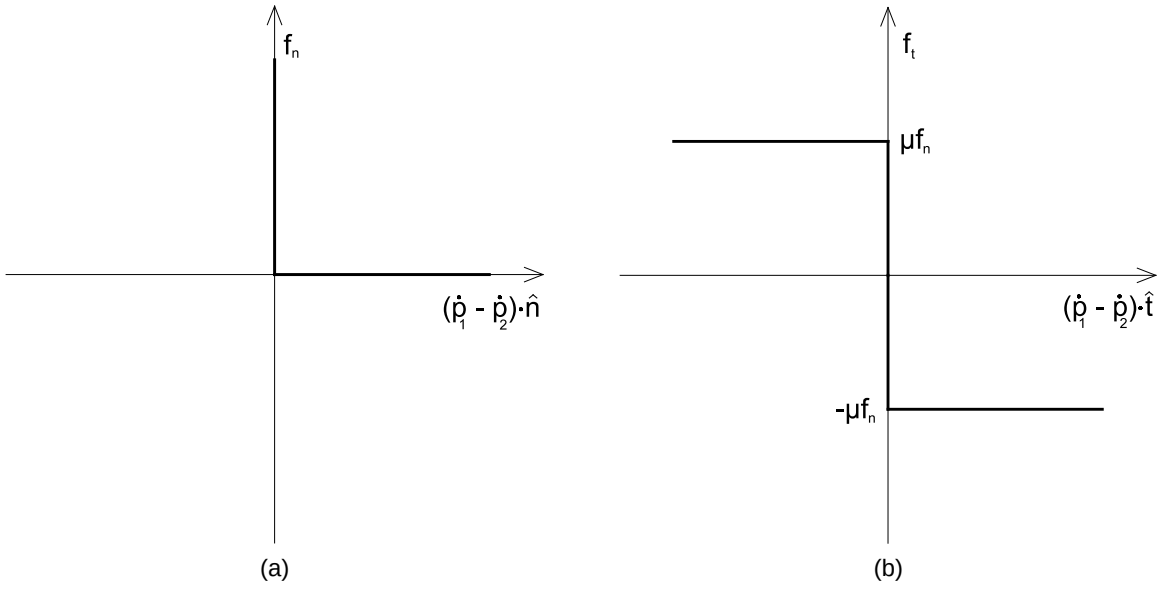

Figure 3.4.: Contact laws in Contact Dynamics and in Box2D: (a) Signorini conditions; (b) Coulomb's friction law

3.2. Modelling with Box2D

3.2.1. Modelling and processing the simulation output

Box2D is a rigid body simulation library written in C++. It is not intended to be a stand-alone software and thus does not contain user interface or any tools to collect or process the simulation output.

In this study, each scenario was simulated using a purpose written computer program (depending on the complexity of the problem, ranging from 200 to over 1300 lines of code) utilizing Box2D to handle the physics of the problem. The output from the simulated scenarios was logged to text files. Typically one file contained a log of quantities analogue to those measured in laboratory experiments such as stress or displacement of the key bodies and the rest of the files contained information for 'drawingWriter', a program written by the author of this study for processing the output data. drawingWriter uses the Asymptote vector graphics language (Hammerlindl et al., 2014) to produce the following drawings:

- Geometry and position of all bodies for a chosen time step
- Map of vector displacements of bodies in the chosen time interval
- Colour map of the accumulated rotations of bodies in the chosen time interval
- Colour map of the accumulated displacements of bodies in the chosen time interval

3.2.2. Simulation accuracy

The following factors affect the simulation accuracy in Box2D:

(i) Convergence

The contact solver treats constraints sequentially and in a model with multiple bodies in contact several iterations are required in order to converge to an accurate global solution. In general, the more velocity iterations allowable to the contact solver the more accurate the solution but also the slower the simulation. The convergence is controlled directly by the maximum number of velocity iterations allowable to the contact solver in a time step, N_i, and indirectly by the time step size Δt. The time step size affects the convergence because of the 'warm starting' technique implemented in Box2D. If a contact is persistent, Box2D uses the values of the corrective impulses from the previous time step as a starting point in the calculation of the new values. This means that the iterations necessary to obtain an accurate answer can effectively be spread over several time steps (providing the problem is not too 'dynamic' in nature).

(ii) Integrator

Box2D uses semi-implicit Euler integration scheme. As with will all numerical integrators, its accuracy improves with decrease in the time step size.

(iii) Body interpenetrations

The position error correction method is not fully based on physics and is a potential source of simulation inaccuracy. It is therefore important to keep the position errors small by reducing the time step size if necessary.

(iv) Floating point arithmetic

Catto (2013) states that: *'Box2D works with floating point numbers and tolerances have to be used to make Box2D perform well. These tolerances have been tuned to*

work well with meters-kilogram-second (MKS) units. In particular, Box2D has been tuned to work well with moving shapes between 0.1 and 10 meters.'

(v) Body skin

Box2D was designed to simulate physics in computer games where problems are often very dynamic in nature. If bodies move by a large amount in one time step, they might pass through each other; this effect is called tunnelling. In Box2D tunnelling can be prevented by continuous collision detection (CCD) scheme. If CCD is used (it is an optional feature), the engine calculates the time of impact (TOI) for colliding bodies; the bodies are then moved to their first TOI and then halted for the remainder of the time step. In order to implement CCD in Box2D, polygons and edges have a skin around them; this is graphically shown in Figure 3.5. The skin does affect rotation of polygons and the thicker it is the bigger the effect (see Section 3.3.3 for more details). Since in quasi-static simulations, which are of interest here, there is no need for CCD, there is also no need for the skin. However, in Box2D the skin is modelled even if CCD is not active; the way around it is to set its thickness to a negligible value (setting it to 0 appears to be a source of inaccuracy) by editing the source code file b2Settings.h. For more information on the use of CCD in Box2D see Catto (2013).

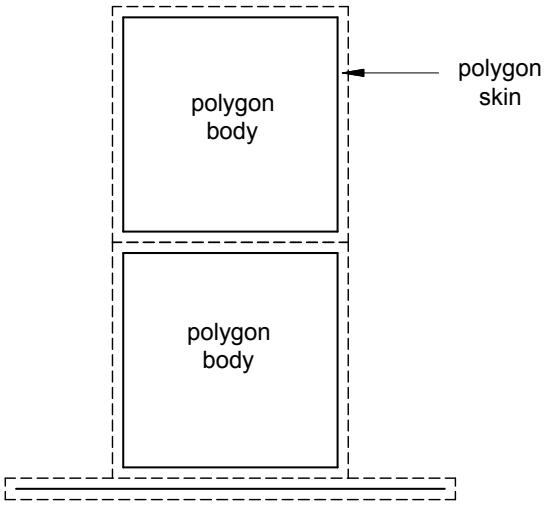

Figure 3.5.: Body skin

3.3. Validation

Box2D was created for computer games where the requirement is to generate simulations which are merely visually believable, rather than physically correct. For this reason its accuracy in modelling a range of problems, for which an analytical or experimental solution exist, was verified before moving on to modelling masonry arch bridges.

In this chapter, there is no discussion on the selection of the simulation input parameters for the presented problems; in most cases the default Box2D values are used (i.e. the time

step size of 1/60s, the number of velocity iterations per time step of 8, the number of position iterations per time step of 3 and the position iteration scaling factor of 0.2); if this is not the case, the parameters were determined with the procedure described in Section 5.2.2. The coefficient of restitution in all simulations was set to 0 as they are either quasi-static in nature or do not involve formation of any new contacts.

3.3.1. Disk on incline

A disk on an incline is a simple dynamic problem featuring both sliding and rotation of one body. The theoretical solution to this problem was derived by Ke and Bray (1995) for the purpose of validation of the Discontinuous Deformation Analysis program DDAD. Consider a disk under the gravity g resting on a plane inclined at the angle β as shown in Figure 3.6. The disc has radius r and the angle of friction between the disc and the plane is ϕ.

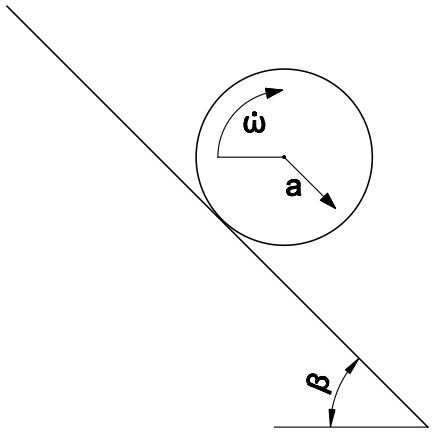

Figure 3.6.: Disc on incline

Depending on the values of β and ϕ the disc will be in one of the three possible modes of behaviour: pure sliding ($\phi = 0$), sliding with rolling ($\phi \leq \phi_L$) or pure rolling ($\phi > \phi_L$) where ϕ_L is the limiting friction angle given by:

$$\phi_L = \tan^{-1}\left(\frac{\tan\beta}{3}\right) \tag{3.59}$$

The magnitude of the linear acceleration $\mathbf{a}$ and the angular acceleration $\dot{\omega}$ are given by:

(i) Sliding with rotation or pure sliding ($\phi \leq \phi_L$):

$$a = g(\sin\beta - \cos\beta\tan\phi) \tag{3.60}$$

$$\dot{\omega} = \frac{2g\cos\beta\tan\phi}{r} \tag{3.61}$$

(ii) Pure rotation ($\phi > \phi_L$):

$$a = \frac{2g \sin \beta}{3} \tag{3.62}$$

$$\dot{\omega} = \frac{2g \sin \beta}{3r} \tag{3.63}$$

The simulation input parameters are given in Table 3.1. Note that because this is a single contact problem, the contact solver computes the final value of the tangential and normal impulses in the first iteration and the value of N_i has no influence on the accuracy of the simulation. On the other hand the value of Δt has to be low because in a dynamic problem the accuracy of the integration is of major importance. The comparison of the average

Table 3.1.: Disc on incline: simulation input parameters

Parameter	**Value**
Time step size Δt	0.0001 s
Number of velocity iterations per time step N_i	8
Number of position iterations per time step	3
Position error correction scaling factor β_f	0.2
Disc and incline coefficient of friction during shearing	variable
Disc radius r	1.0 m
Angle of incline of the plane β	$45°$
Gravity g	1.0 m/s^2
Simulation length	1.0 s

linear acceleration and the average angular accelerations after 1.0 s of the simulation with the theory is shown in Figures 3.7a and 3.7b respectively. Since in Box2D accelerations do not directly appear in the simulation they were back calculated from the velocities. The Box2D accelerations for pure rolling case ($\phi > \phi_L$) are essentially equivalent to the theoretical values. Some deviation for the sliding with rotation case becomes noticeable when ϕ approaches the limiting value ϕ_L; the maximum error is at $\phi = \phi_L$ where the simulated linear and angular accelerations are 96.8% and 101.6% of the theoretical values respectively. The simulation ϕ_L was found to be $19.25°$, slightly higher than the theoretical value of $18.43°$. The comparison of the accumulated rotation of the disc with the theory is shown in Figure 3.7c. The accuracy is essentially the same as for the angular acceleration; this suggests that the influence of the position error correction scheme on the results was negligible. Overall, the accuracy can be considered to be satisfactory.

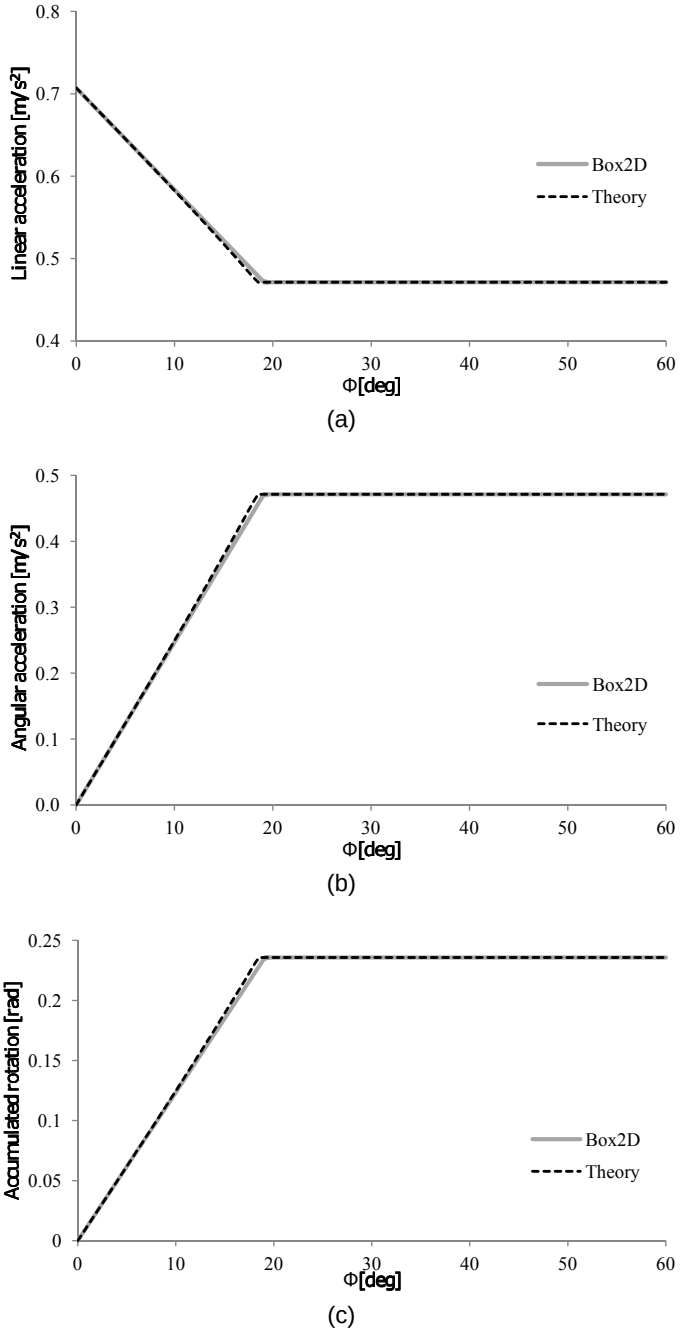

Figure 3.7.: Disc on incline: (a) Linear acceleration; (b) Angular acceleration; (c) Rotation accumulated in 1.0 s

3.3.2. Biaxial compression of hexagonally packed discs

To verify the ability of the physics engine to accurately model an assemblage of bodies, a simulation involving biaxial compression of hexagonally packed discs was run, and then validated against the theoretical solution derived by Rowe (1962). The theoretical stress ratio for this problem is:

$$\sigma_1/\sigma_2 = \tan 60^\circ \tan(\phi_\mu + \beta) \tag{3.64}$$

where σ_1 is the major principal stress, σ_2 is the minor principal stress, ϕ_μ is the angle of particle surface friction, defined as $\phi_\mu = \tan^{-1}(\mu)$ and β is the deviation of the tangent at

the contact point between sliding discs from the direction of the principal stress.

Model

The simulation input parameters are given in Table 3.2. The test sample consisted of 32 discs. Figure 3.8a demonstrates how the confining stress was simulated. The test was strain-controlled with the deviatoric stress applied by the top cap moving vertically at a constant velocity. The top cap and the bottom boundary were rigid and frictionless. The test was conducted under zero gravity.

Table 3.2.: Biaxial compression of hexagonally packed discs: simulation input parameters

Parameter	**Value**
Time step size	1/60 s
Number of velocity iterations per time step	8
Number of position iterations per time step	3
Position error correction scaling factor	0.2
Disc diameter	1.0 m
Disc density	1000 kg/m^2
Disc surface friction ϕ_μ	10°
Force F	100 N
Top cap velocity	0.001 m/s

Results

The results of the test on discs with $\phi_\mu = 10°$, the same friction as in the experimental validation tests conducted by Rowe (1962), are shown in Figure 3.8c. The failure mechanism is shown in Figure 3.8b. The stress ratio closely matches Rowe's solution across the whole strain range. The peak stress ratio is 100.9% of the theoretical value (100.5% in terms of angle of friction). The accuracy achieved is superior to that reported by O'Sullivan and Bray (2003), who modelled the same problem with the distinct element method code PFC2D and a modified version of discontinues deformation analysis code DDAD; their simulations yielded a peak angle of friction of about 92% of the theoretical value.

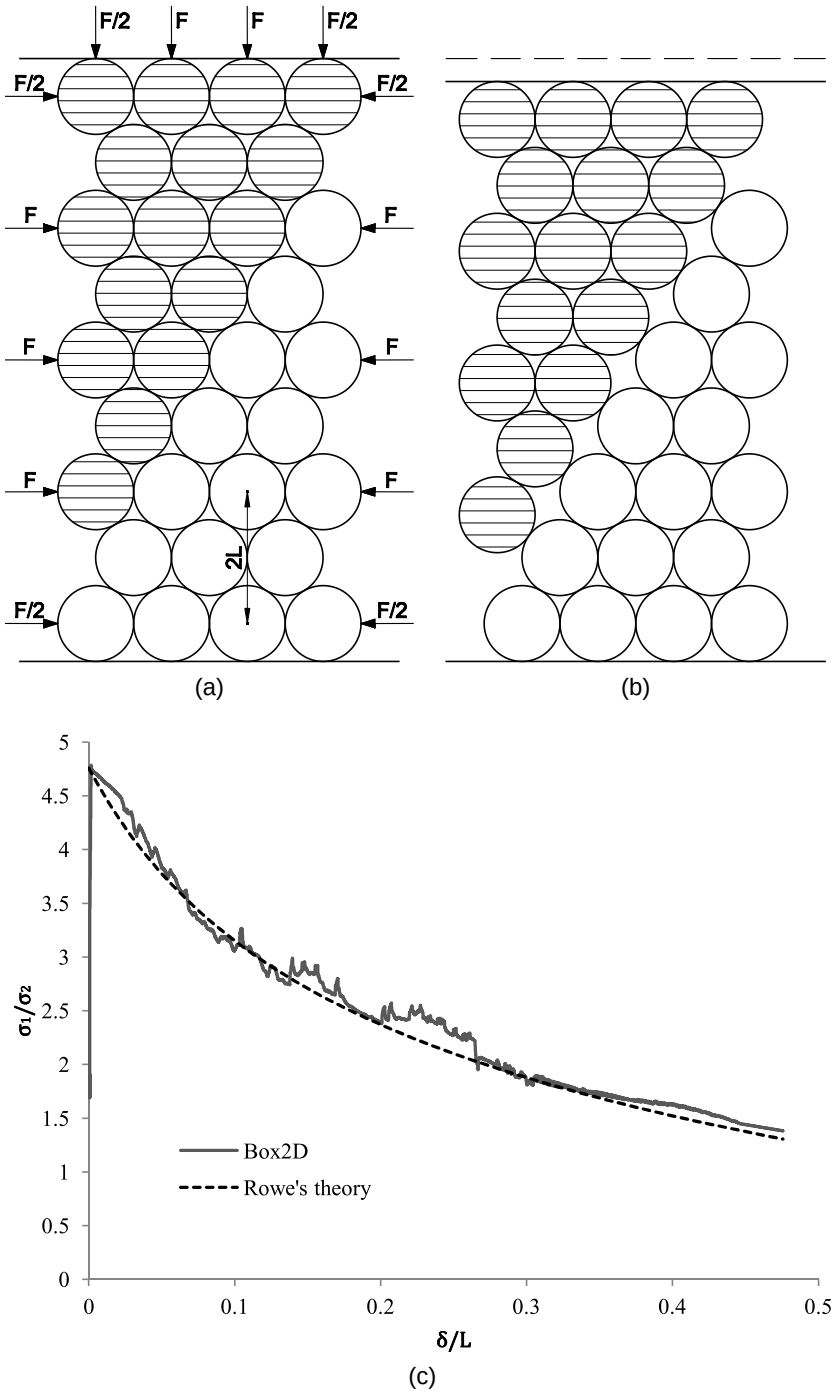

Figure 3.8.: Biaxial compression of hexagonally packed discs: (a) confining stress model; (b) failure mechanism; (c) results, where δ is the vertical displacement and L is the initial length per row in the vertical direction as shown in Figure 3.8a

3.3.3. Block on incline

A simulation of polygons is much more challenging than that of discs because the collision detection phase, including determination of the collision normal unit vector, becomes non trivial. A block on an incline is a simple problem allowing investigation of the accuracy in capturing a sliding and a toppling failure of a polygon; this problem has been considered for example by Hoek and Bray (1981). Consider a block of width b and height h resting on a plane inclined at an angle β as shown in Figure 3.9a. A toppling failure will occur if the weight of the block W falls outside the base of the block i.e. when $b/h < \tan\beta$. A sliding failure will occur if β is greater than the angle of surface friction between the block and the incline ϕ_μ.

In the Box2D simulations, the block was created on a horizontal plane. The plane was then slowly rotated at a constant rotational velocity until the block failed. The simulation input parameters are given in Table 3.3.

Table 3.3.: Block on incline: simulation input parameters

Parameter	**Value**
Time step size	1/60 s
Number of velocity iterations per time step	8
Number of position iterations per time step	3
Position error correction scaling factor	0.2
Block width	1.0 m
Rotational velocity of the plane	0.001 rad/s

In the first set of tests, b/h was set to 2 in order to prevent the toppling failure and ϕ_μ was the variable. The values of β at failure in the tests in this series are shown in Figure 3.9b. The results are essentially identical with the theory.

In the second set of tests, ϕ_μ was set to 60° in order to prevent the sliding failure and b/h was the variable. The values of β at failure in the tests in this series are shown in Figure 3.9c. The results are close to the theoretical values but the accuracy is slightly lower than in the sliding failure case. The discrepancy is caused by the skin around the block and the plane. Figure 3.10a shows the influence of the skin thickness on the accuracy of the simulation for a range of values of the body size. It is evident that the deviation from the theoretical value of β at failure increases with: (i) the increase in the skin thickness and (ii) the decrease in the size of the block. In the explored range of skin thicknesses and block sizes, a very accurate prediction of β at failure in a Box2D simulation can be made using a slightly modified theoretical expression:

$$\beta = \arctan(\frac{b}{h+l}) \tag{3.65}$$

where l, graphically shown in Figure 3.10b, is equal to twice the skin thickness minus the tolerance on the skin overlap. Figure 3.10c shows the comparison of the Box2D results with the prediction made using Equation 3.65 for the block with b=0.1m and the skin thickness of 0.01m (i.e. the smallest block and the thickest skin in the study); the agreement is excellent.

Thus it can be deduced that in Box2D a toppling block does not rotate exactly around the corner of its body but, instead, around a point inside its skin (note that there is no information on this issue in the software documentation).

In practice, as shown in Figure 3.10a, in simulations involving bodies larger than 0.1m, the influence of the skin on the results can be deemed negligible if its thickness is set to a value of 0.001m or lower.

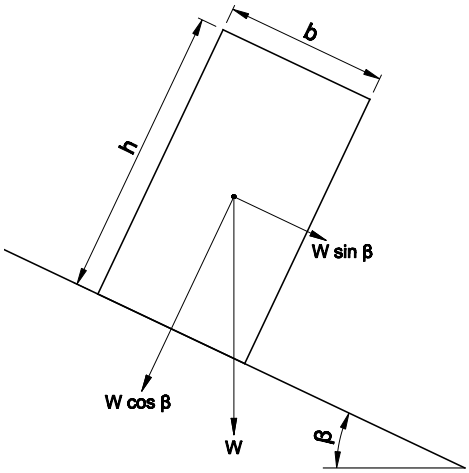

(a)

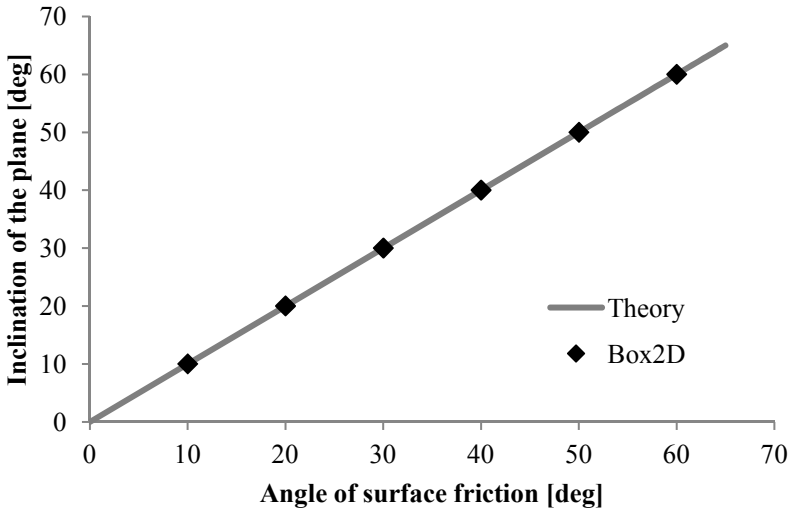

(b)

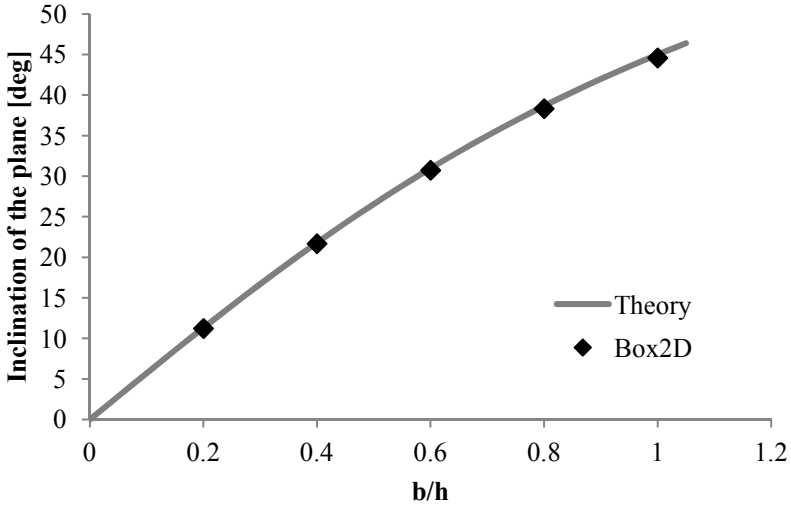

(c)

Figure 3.9.: Block on incline: (a) Model; (b) Results: sliding failure; (c) Results: toppling failure;

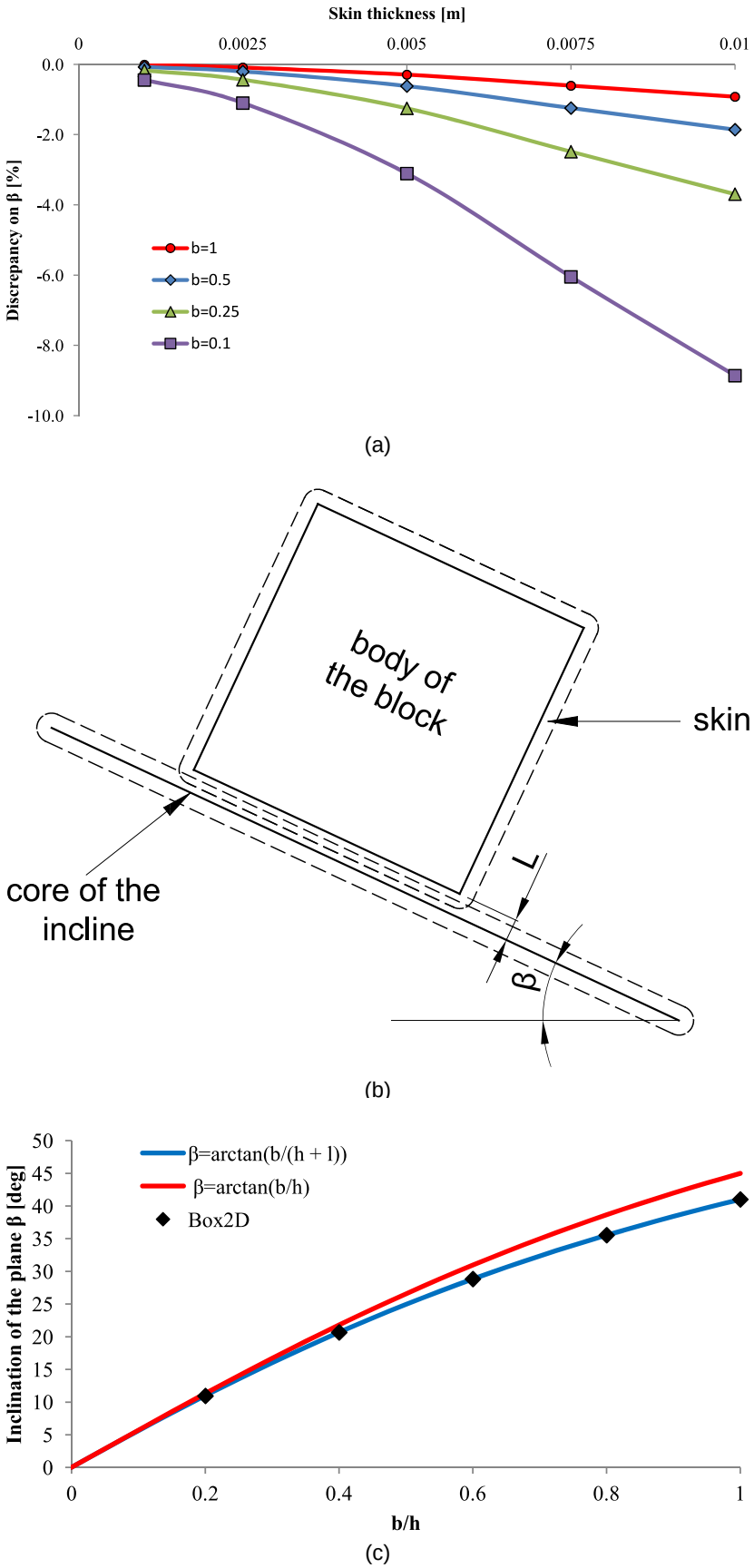

Figure 3.10.: Block on incline; influence of the skin on the simulation of the toppling failure mode (a) parametric study (simulations with b/h=1); (b) model with the skin; (c) theoretical value of β at failure (simulations with b=0.1 and the skin thickness of 0.01m giving l=0.015m)

3.3.4. Multiple blocks on incline

To verify the ability of the physics engine to accurately model an assemblage of polygons, a problem involving multiple blocks on incline, graphically depicted in Figure 3.11a, was modelled. In this problem the base plate is slowly rotated until the blocks start to fall freely. The global failure mode involves simultaneous sliding and toppling of individual or groups of blocks what, particularly with a large number of blocks in the system, makes this problem a good accuracy test. This problem was originally considered by Ashby (1971) who conducted a series of laboratory experiments with assemblages of plaster blocks. Additionally the non-associative limit analysis solutions for this problem are available in Babiker et al. (2014). These use an iterative method to converge at a single plausible non-associative solution. Minimum and maximum non-associative loads can then be determined based on the kinematics of this solution. Other non-associative solutions may be possible.

In order to make the code simpler the rotation of the plane was simulated with a horizontal gravity field. The equivalent inclination of the plane is given by $\beta = \tan^{-1} \lambda$ where λ is the ratio of the horizontal gravitational acceleration to the vertical gravitational acceleration. The simulation input parameters are given in Table 3.4. The block-block and block-plane interface friction angle ϕ_μ was set to the same value as in Ashby (1971) and Babiker et al. (2014).

The comparison of the results with the experimental data and the limit analysis is given in Figure 3.11b. In problems with up to 25 block columns β at failure is above the experimental values but very close to the maximum non-associative solution. In problems with 30 and 35 block columns the Box2D and the experimental results are very similar. The possible reasons for the discrepancies in problems involving lower number of block columns between Box2D simulations and the results reported by Ashby (1971) are: (i) ϕ_μ in the physical model was unlikely to be exactly 36° for all interfaces; in problems involving smaller number of blocks individual deviations would have a bigger impact on the results; (ii) in the physical tests the blocks can be damaged e.g. a block apex can be sheared off which promotes toppling and damage to the block surface may reduce the interface angle of friction; the numerical model does not take into account these effects. There are no theoretical solutions for this problem but the Box2D results are either within the min-max envelope of the non-associative limit analysis solutions of Babiker et al. (2014) or very close to their upper limit.

In summary, Box2D provides a reasonably good prediction of the global model stability in this problem but the potential error might be on the unsafe side. However, due to the non-uniqueness of non-associative solutions, other issues such as block damage and initial variation in geometry could have moderately significant effects which would explain the variations. Modelling such imperfections in Box2D might lead to lower loads.

Table 3.4.: Multiple blocks on incline: simulation input parameters

Parameter	Value
Time step size	1/60 s
Number of velocity iterations per time step	100
Number of position iterations per time step	3
Position error correction scaling factor	0.2
Block width	1.0 m
Equivalent rotational velocity of the plane	0.001 rad/s
ϕ_μ	36°

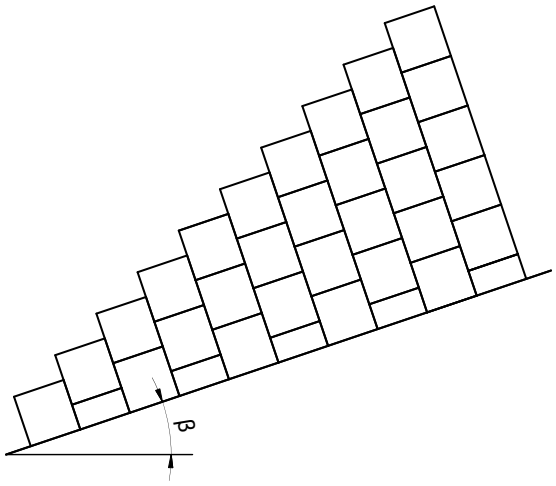

(a)

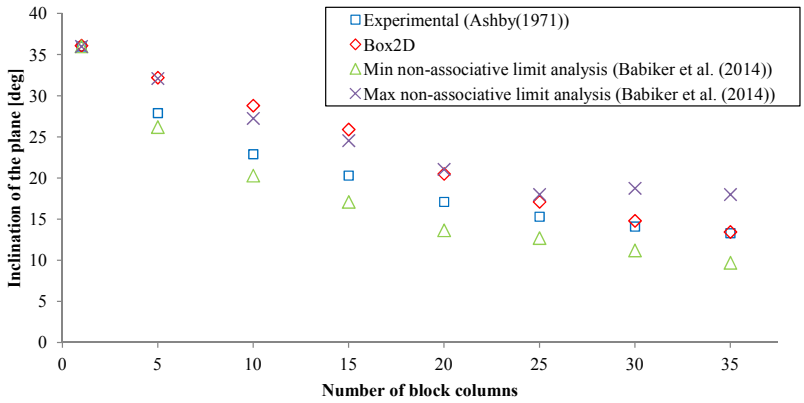

(b)

Figure 3.11.: Multiple blocks on incline: (a) Model with 10 column blocks; (b) Results

3.3.5. Conclusions

Box2D has been found to be capable of accurately simulating disc interaction dynamics. The accuracy achieved in simulation of biaxial compression of hexagonally packed discs was superior to that achieved using the PFC2D and DDAD discrete element method codes quoted in the literature.

Box2D has been shown to be capable of accurately predicting the stability of a single block providing that the body skin thickness is insignificant compared to the body size.

The predictions of global stability of assemblages of blocks have been found to be non-conservative when compared to the experimental results but they follow the experimental trends and the discrepancies become very low for large number of blocks. It is not clear whether the discrepancies are due to the inaccuracies in the numerical simulation or additional phenomena in the physical tests which were not taken into account in the simulations. Compared to the non-associative limit analysis of this problem quoted in the literature, the Box2D results were either within the min-max envelope of the reported possible solutions or very close to their upper limit.

In summary, Box2D is capable of generating physically correct simulations and thus is a viable alternative to the two-dimensional DEM tools currently applied in engineering practice.

4. Modelling soil using Box2D physics engine

This chapter discusses the soil model adopted in this study. A biaxial compression test program allowing determination of the macro-scale properties of virtual soils is also presented and it is shown that this tool can successfully capture the critical state response of granular media.

The biaxial compression test program utilizes the Box2D physics engine described in Chapter 3 to carry out the simulations. The graphical output from the simulations presented in this chapter was produced with the drawingWriter program. In all the presented simulations: (i) the number of position iterations per time step and the position error correction scaling factor were kept at their default Box2D values of 3 and 0.2 respectively and (ii) the coefficient of restitution of 0 was used

4.1. Soil model

Traditionally soil is modelled as a continuum material. However, capturing key aspects of soil behaviour can be difficult when using this approach, and the many highly complex constitutive models developed to date generally fail to fully model certain important aspects of real soil behaviour. The complexity of observed macro level soil behaviour essentially results from its granular nature. When individual particles are considered, their interaction generally follows relatively simple physics; this concept is a foundation of the particulate discrete element method (DEM) which is utilized in this study (i.e. as Box2D fulfills the definition of a DEM program proposed by Cundall and Hart (1992)). This study is limited to frictional soils only; cohesive forces between particles are not modeled.

4.1.1. Micro-scale soil properties

Deformation of a granular soil, at the micro-scale level, is accommodated by interparticle sliding and rolling. Micro-scale soil properties controlling these two interaction mechanisms will therefore also control the macro-scale behaviour; these properties are discussed below.

Particle eccentricity

Particle eccentricity refers to the global form of the particle; in two-dimensions it reflects the difference between particle height and width. Particle eccentricity hinders rotation and ability for particle rearrangement; at the macro-scale this translates into increased dilation,

peak shear strength and, to a lesser degree, critical state shear strength. Eccentricity also enhances an anisotropic behaviour which means the more eccentric the particles the higher the sensitivity of the soil behaviour to the initial soil fabric and the loading direction. For more information on the influence of particle eccentricity on granular soil behaviour see Rothenburg and Bathurst (1992) and Cho et al. (2006).

Particle angularity

Particle angularity describes the shape of the corners on a particle; the sharper the corners the more angular the particle. Angular particles tend to interlock which hampers both inter-particle sliding and rotation. Angularity increases dilation, peak shear strength and critical shear strength; its influence on the critical state friction angle is more significant than that of particle eccentricity (Cho et al., 2006). For more information on the influence of particle angularity on granular soil behaviour see Cho et al. (2006); the paper also features a database of particle shape properties of various sands.

Particle coefficient of friction

The coefficient of friction of a particle, μ_i, describes its surface texture; in real soils it depends not only on the particle roughness but also on its hardness and the magnitude of the normal force the particle is subjected to (Senetakis et al., 2013*a*). High values of contact coefficient of friction, μ (in Box2D calculated from: $\mu = \sqrt{\mu_1 \mu_2}$), force transition in particle behaviour from sliding to rolling. The influence of μ on granular soil behaviour was studied numerically by Huang et al. (2014) and Morgan (1999). The researchers found that shear strength, both peak and critical state, increases with increase in μ but this effect diminishes at values of μ higher than 0.5. Additionally, high values of μ appear to stiffen the response of soil in the initial-section of the stress-strain curve. Note that, although the general trends in the cited papers are likely to be representative of real granular soil behaviour, the quantitative results are correct only for systems comprised solely of disc/spherical particles.

Particle size distribution

The influence of particle size distribution (PSD) on the granular soil behaviour was studied by Morgan (1999) and Morgan and Boettcher (1999); the researchers concluded that PSD has secondary but measurable influence on frictional strength and volume strain. In general, in small quantities finer particles tend to fill the pore spaces, increasing contact area and consequently frictional resistance to shear deformation; in large quantities fine particles define the shearing matrix and act as a 'lubricant' between rotating large particles.

Initial particle arrangement

Initial particle arrangement, especially the bulk density, has significant influence on the macro-scale soil behaviour. In dense systems particle rotation is inhibited by high number of interparticle contacts; in order to accommodate shear deformations the soil system has to

dilate which requires extra energy; this translates into a peak strength behaviour where the peak angle of friction corresponds to the maximum rate of dilation; the peak is followed by strain softening which gradually brings the angle of friction to the critical state value which is independent of the initial particle arrangement. Loose systems, initially can accommodate part of the load induced deformations by contraction, a mechanism energetically cheaper than constant volume shearing; this translates into gradual increase in the mobilized angle of friction up to the critical state value. The influence of bulk density on the behaviour of frictional soils is described in several textbooks on soil mechanics; for more information on this topic see e.g. Wood (1990).

Particle crushing strength

The relevance of particle crushing strength to the macro-scale soil behaviour depends on the stress magnitudes in the problem. In low stress problems this property can be effectively ignored but at hight stresses particle crushing might be energetically cheaper than inter-particle sliding or rolling and therefore the global shear strength will be lower. Particle crushing also leads to change in PSD and particle shape (the newly created particles are likely to be more angular). For more information on the influence of particle crushing on granular soil behaviour see e.g. Morrow and Byerlee (1989).

Particle elastic modulus

The effect of elastic deformations of individual particles on large strain soil behaviour is usually negligible (the macro-scale deformations being a result of particle rearrangements instead) and is therefore ignored in this study.

4.1.2. Adopted soil model

The properties of the soil model adopted in this study do not represent those of any real soil but they do provide relatively realistic behaviour whilst keeping the model very simple. The particles were modelled as randomly shaped convex dodecagons. The height to width ratio of particles (where for a given particle with vertices numbered consecutively 0 to 11, height is the distance between the vertices 0 and 6 and width it the distance between the vertices 3 and 9) was set to 1.0 in order to limit the effect of the initial fabric on the results. Figure 4.1 shows an example of the particles used in the simulations. The eccentricity of this particle model is effectively zero, the angularity is relatively high but the convex limitation, although simplifying the simulations, means that the tendency of particles to interlock will be much lower than in the real soils. The coefficient of friction, μ, was set to 0.6 which provides a stiff load response of dense samples which, as it will be shown later, was desired in this study. Particles were of uniform size d_b, where d_b is defined as a diameter of a circle bounding the full extent of a given particle. The particles are modelled as rigid bodies and therefore are not allowed to crush or deform.

In practice, the Box2D soil model would have to replicate the macro-scale behaviour of the prototype backfill material; it can be hypothesized that, providing the problem is plane

strain, this can be achieved by replicating the micro-scale properties of the prototype backfill material.

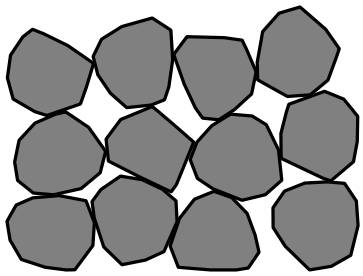

Figure 4.1.: Polygon shaped particles

4.2. Biaxial compression test

The biaxial test program allows the determination of the macro-scale behaviour of the soil model with given micro-scale properties. The series of tests described here was performed on the soil model described in Section 4.1.2. Apart from determining the macro-scale properties of the soil model used later in the backfilled masonry arch tests, this series of tests is also a verification of the ability of Box2D to successfully capture the critical state type response of granular media as defined by O'Sullivan (2015).

4.2.1. Simulation accuracy

As discussed in Sections 3.2.2 and 5.2.2, the main tools to control the accuracy of the simulation are the time step size, Δt, and the maximum number of velocity iterations per time step available to the constraint solver N_i. Additionally for given values of Δt and N_i, accuracy is affected by the ratio of the force experienced by a given particle to its mass. A high ratio will lead to a high tentative velocity, and consequently to large velocity errors that then have to be corrected by the constraint solver (as target velocities will be close to zero in a quasi-static analysis). Therefore in the biaxial compression test described here the values of confining pressure and density could be selected with a view to maximising accuracy for a given runtime, rather than to replicate laboratory test settings. (i.e. as this test simply involves an assemblage of rigid particles under zero gravity, these parameters will not affect the physics of this quasi-static simulation). The adjustments of the confining pressure and the density of soil particles are similar in nature to the technique described in Section 5.2.3, with the difference being that this test is under zero gravity and the load is applied in a displacement control mode.

4.2.2. Sample preparation

The simulation input parameters are given in Table 4.1. Particles were created simultaneously at a random position and at a random orientation within a two dimensional zone of approximately 50 $\times$ 166 d_b and were not allowed to overlap; the width of the zone was equal

Table 4.1.: Biaxial compression of polygon particle specimens: simulation input parameters

Parameter	Value
Soil particles	
Coefficient of friction	μ_g or μ_s
Coefficient of restitution	0
Density	5000 kg/m^2
Size d_b	1.0 m
Test setup: general properties	
Time step size	1/60 s
Number of velocity iterations per time step	100
Approximate number of particles	5000
Test setup: sample generation stage	
μ_g for loose sample	0.6
μ_g for dense sample	0.2
Gravity	0.1 m/s^2
Test setup: shearing stage	
μ_s	0.6
Coefficient of friction of the top cap and the bottom boundary	1.0
Confining pressure	1 kN/m
Top cap velocity	0.005 m/s

to the final width of the sample and the height of the zone was determined automatically, in an iterative process, as the minimum required to create the specified number of non-overlapping particles. The sides of the zone were bounded by temporary rigid frictionless walls. Once created, the particles were allowed to fall under gravity. After all the particles had come to rest, the top of the sample was levelled, gravity was gradually reduced to zero and the temporary side walls were removed. The final sample size was 50 $\times$ 100 d_b. The initial sample density was controlled by the particle friction coefficient (μ_g) used at the sample generation stage (the lower the μ_g, the more easily the particles can slide over each other and, as a result, the higher the initial packing density).

The exact shape and drop position for each particle was determined by the random number generator; in order to check repeatability both test setups were run three times with different seeds. The initial void ratios for all specimens are listed in Table 4.2.

4.2.3. Confining stress

The confining pressure in the horizontal direction was simulated by applying forces to the centre of mass of the particles at the perimeter of the specimen. Boundary particles were determined automatically in each time step by casting multiple horizontal rays along the height of the specimen. The force applied to a boundary particle was proportional to the number of rays hitting the particle in a given time step. The confining pressure in the vertical direction was applied by a 'servo-controlled' rigid top cap. The confining pressure was applied incrementally until the sample was in equilibrium at 1 kN/m. The particle coefficient of

Table 4.2.: Biaxial compression of polygon particle specimens: void ratios

Seed	Loose sample e_l	Dense sample e_d	$\frac{e_l - e_d}{e_l}$
Initial global average			
1	0.311	0.258	0.17
2	0.308	0.259	0.16
3	0.307	0.260	0.15
RVE at 15% axial strain			
1	0.296	0.296	0.00
2	0.295	0.290	0.02
3	0.296	0.293	0.01

friction was then gradually changed to the value used for shearing (μ_s).

It has to be noted that when using the biaxial compression test program, unlike in a real laboratory test, there is no need to conduct tests at various levels of confining stress; this is because the results, by definition, have to be the same since the particles are modelled as rigid bodies and therefore are not allowed to crush or deform.

4.2.4. Biaxial compression

The compression was strain-controlled with deviatoric stress applied by the top cap moving vertically at a constant velocity. Figure 4.2a shows the mobilization of the angle of friction with the axial strain for both the loose and dense states (3 simulations per state). The corresponding evolution of volumetric strain and global void ratio are shown in Figures 4.2b and 4.2c respectively. Figures 4.3a and 4.3b show particle arrangement and accumulated rotation at 15% axial strain of the seed 1 dense and the seed 1 loose samples respectively.

Overall the results show reasonably good repeatability between simulations. Qualitatively all the dense and the loose samples display behaviour typical of that obtained in laboratory experiments. The loose samples contract and the dense samples dilate upon shearing, consistent with critical state behaviour. However the global average void ratios plotted in Figure 4.2c do not converge as expected. Figures 4.3a and 4.3b show that in the loose system, shear deformations are spread across most of the sample whilst in the dense system shearing is localized in distinctive bands, with large parts of the sample undisturbed by shearing, and having local void ratios largely unchanged from the initial values. In Figures 4.3a and 4.3b a volume element (RVE) considered to be representative of the part of the sample that underwent shearing is indicated by a red circle. Each RVE contained approximately 10% of the sample volume and was positioned in the zone with the highest density of particles having high accumulated rotation. The void ratios in the RVEs of all samples at 15% axial strain are given in Table 4.2. The results show that parts of the samples that underwent shearing converged or are very close to convergence to a consistent critical state void ratio.

The mobilized angle of friction also converges to the critical state value ϕ_{crit}, of about $21.5°$, for both the loose and the dense states. The dense samples exhibit peak strength behaviour, with a peak angle of friction of about $29°$; the peak strength corresponds to the

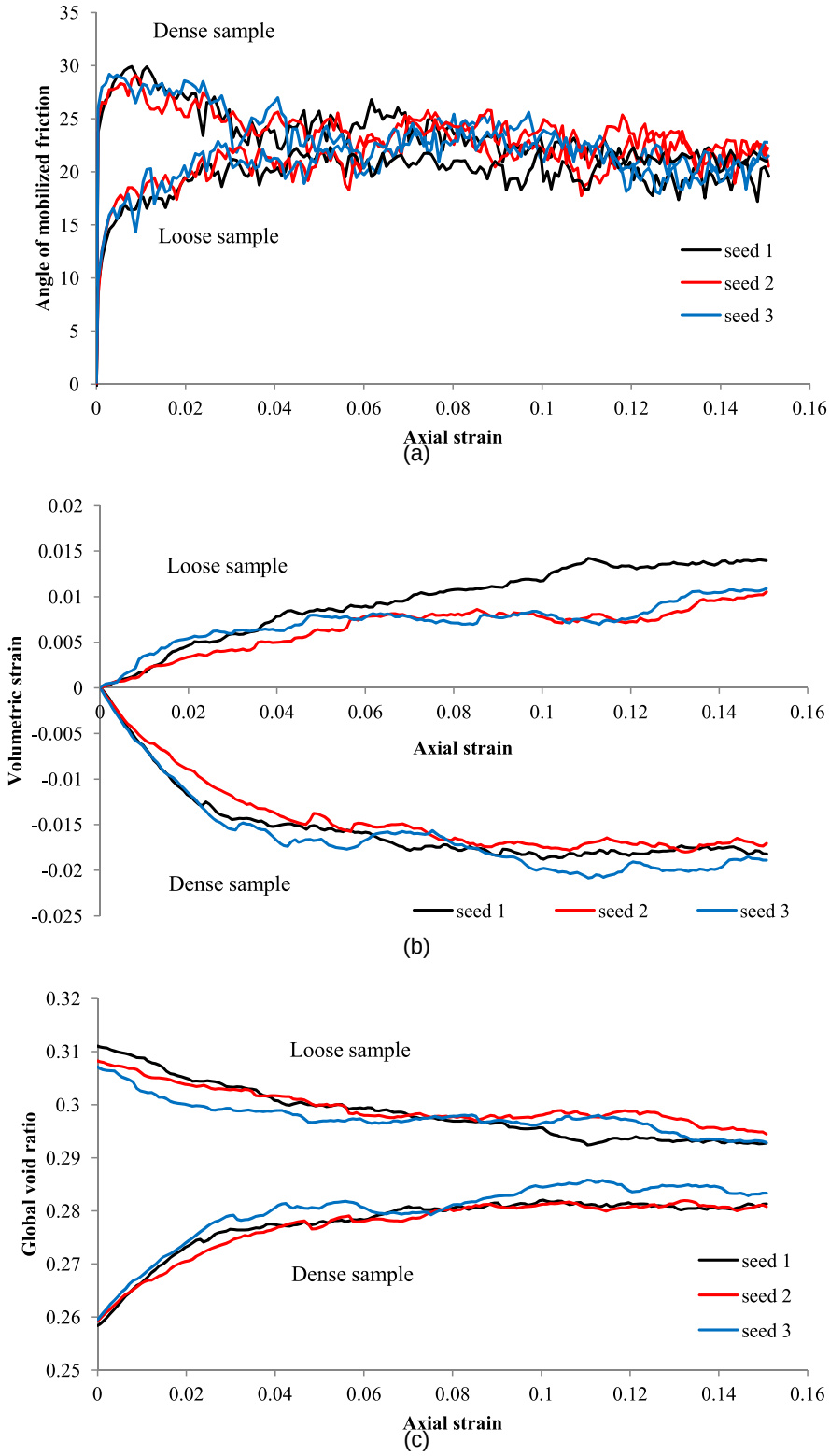

Figure 4.2.: Macromechanical response of polygon particle specimens: (a) angle of mobilized friction; (b) volumetric strain; (c) global void ratio

maximum rate of dilation.

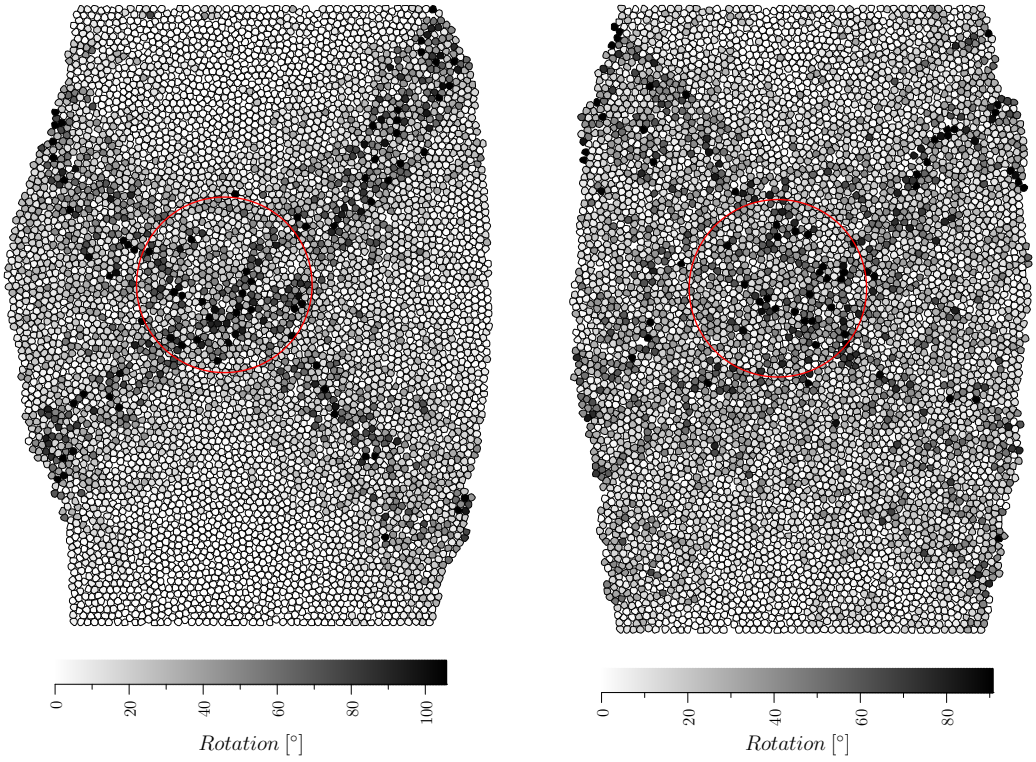

Figure 4.3.: Particle arrangement and accumulated rotation at 15% axial strain: (a) dense sample; (b) loose sample.

4.2.5. Discussion

The biaxial compression test demonstrated that the proposed approach to modelling soil allows the capture of some of the fundamental characteristics of a granular media and therefore has the potential to be used in simulation of frictional backfill materials if further developed. The tested soil model has low shear strength and, when initially dense, very high stiffness but this can be attributed to its micro-scale properties which were chosen for simplicity rather than to be representative of those of a real soil. Clearly, an extensive study is required to develop appropriate soil models but due to time limit the author could not embark on this task.

5. Modelling masonry arch bridges using Box2D physics engine

The purpose of this chapter is to describe and validate three computer programs developed by the author of this study which together with the biaxial compression test program described in the previous chapter create a virtual laboratory for testing of masonry arch bridges with frictional backfill.

The programs utilize the Box2D physics engine described in Chapter 3 to carry out the simulations. The graphical output from the simulations presented in this chapter was produced with the drawingWriter program. In all the presented simulations: (i) the number of position iterations per time step and the position error correction scaling factor were kept at their default Box2Dvalues of 3 and 0.2 respectively and (ii) the coefficient of restitution of 0 was used.

5.1. Masonry model

In this study masonry structures were idealised as assemblages of rigid bodies. Each masonry block, a brick or a stone unit, was modelled as a separate body. Masonry joints in the numerical model had zero thickness and did not carry tension. Thickness of mortar joints in the physical structure under consideration was taken into account by increasing the size of the masonry blocks in the numerical model accordingly. In the context of masonry arch bridges, the idealised model used here allows the capture of the most common failure modes including the formation of plastic hinges and sliding; this was judged to be sufficient at this stage of the research.

5.2. Bare arch test

The bare arch test program allows the simulation of a load test to failure on voussoir type masonry arches. The purpose of this program is provide a tool for quick verification of the arch models before they are used in the, more challenging, tests with backfill.

In this section results of tests on several arches of various properties, modelled in order to verify the overall accuracy of the simulations, are presented. The choice of the simulation input parameters is discussed and a method to decrease the simulation time is proposed.

5.2.1. Test setup

Masonry was modelled with the approach described in Section 5.1. An example model is shown in Figure 5.1a.

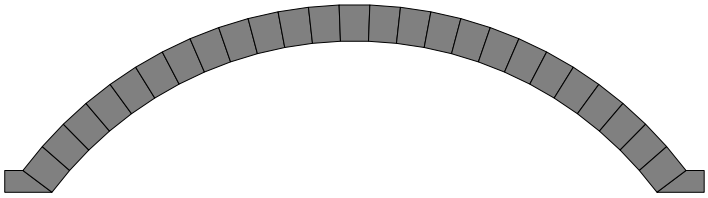

(a)

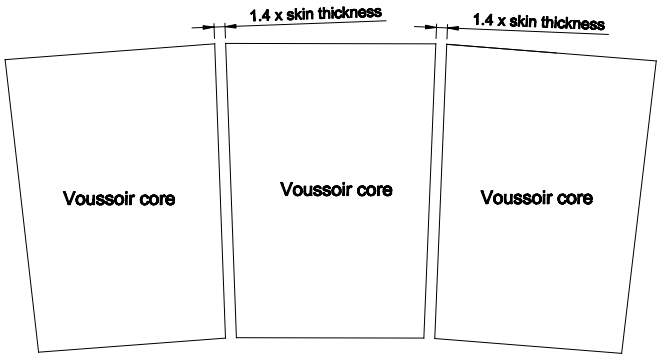

(b)

Figure 5.1.: Bare arch test: (a) arch model; (b) space for body skin.

The width of the voussoirs was decreased in order provide the space for the body skin; this is illustrated in Figure 5.1b. A pilot study revealed that this adjustment is required if the results are to be accurate; the optimum distance between the cores of adjacent blocks was found to be $1.4\times$skin thickness. This adjustment reduces the effective unit weight of the masonry so either the skin volume has to be negligible compared to the volume of the voussoirs or the masonry density has to be increased in order to take this into account. In this study the skin thickness was reduced to $0.001m$ which kept the skin to voussoir volume ratio below 0.00015 in all simulations.

The gravity was applied incrementally, the target value was reached in 100 seconds; this approach is required in order to avoid any dynamic effects which might lead to deformation of the arch prior to the load application.

The load was applied as a force acting directly on the loading voussoir. The loading voussoir and the exact point of load application were determined prior to loading. The position of the loading point was constant throughout the simulation in the local coordinate system of the voussoir but could move together with the voussoir in the global coordinate system. The load was always applied in the vertical direction.

In order to avoid dynamic effects a limiting condition was set on the velocity of the loading voussoir. If the velocity was below $\Delta t \times \frac{g_{test}}{10}$, where g_{test} is the gravitational acceleration in the test, the load was applied at a constant specified rate; if the velocity was above the limiting value, the loading rate was temporarily set to 0. This condition also ensured that no additional load was applied once the arch was transformed into a mechanism. The test was

stopped when the total displacement of the loading voussoir exceeded the ring thickness.

5.2.2. Accuracy settings

Simulation accuracy can be controlled by adjusting the time step size, Δt, and the maximum number of velocity iterations per time step available to the constraint solver, N_i. The values of these parameters, required for a given level of accuracy, depend on the simulated scenario and currently, as there is no guidance, have to be determined for each modelled problem separately.

Proposed procedure

In this study, Δt and N_i were determined in the following two steps:

(i) Arbitrarily select a value of N_i

(ii) Find the optimal value of Δt by running a series of simulations with Δt halved in each subsequent run. If the difference in the collapse load between a two consecutive simulations, termed the consecutive run discrepancy and calculated from:

$$\frac{P_1 - P_2}{P_1} \times 100\% \tag{5.1}$$

where P_1 is the collapse load in the first simulation of the pair and P_2 is the collapse load in the subsequent run with the Δt halved and all the other input parameters kept the same, is less than the specified error limit, the higher value of Δt from this pair of simulations is taken as the optimum.

The parametric study is being run on Δt and not on N_i because this order guarantees that the results in the consecutive runs are converging to the correct collapse load; this is because N_i controls only the convergence of the velocities in a given time step whilst Δt, apart from the convergence, controls also the accuracy of the integrator and, in problems with bodies moving at high velocities, the magnitude of the position errors. In general, the same level of accuracy can be achieved with several combinations of N_i and Δt but each will have a different runtime; from a practical perspective there is a need for guidance on the selection of N_i leading to the shortest runtime for a given scenario but this is out of scope of this document (based on the experience of the author, the higher the number of bodies in a problem, the higher the optimum N_i; see the worked example in this section for a sensible value on N_i in a bare arch test).

Note that, the choice of the loading rate is of small importance in quasi-static simulations because it is the load (or displacement) increment per time step that matters; and this depends on the time step size which is subject to a parametric study. The value of loading rate in this test was selected with a view to ensure the load increment per time step for the initial time step size was below 0.025% of the expected collapse load. Note that in this test the influence of the selected value of the loading rate on the results is inherently low because of the limiting condition on the velocity of the loading voussoir explained in Section 5.2.1.

Worked example

The procedure of determining the values of Δt and N_i is shown for a 51 voussoir arch loaded at quarter span (arch properties are given in Table 5.1). The limit on the consecutive run discrepancy was taken as 0.1%. The loading rate was set to 10 kN/s and the initial value of Δt was taken as $0.01s$ (a round number, slightly lower that the default value of $1/60\ s$). The consecutive run discrepancies and the runtimes for each simulation are shown in Figure 5.2a. The results show that in the simulated scenario the lower N_i, the lower the runtime for the set of N_i and Δt satisfying the accuracy requirements; for example for N_i of 500 the maximum Δt that satisfies the discrepancy conditions is $0.0025s$ and the runtime for this set of parameters is $281s$ whilst for N_i of 25 the maximum allowable Δt is $0.0005s$ and the runtime is only $105s$. Figure 5.2b compares the consecutive run discrepancies with the discrepancies between a given Box2D simulation and the true collapse load determined with LimitState:RING (a limit analysis software which provides the exact failure load for arches modelled as an assembly of rigid blocks). The results show that the proposed method of relying on the consecutive run discrepancies provides a good prediction on the actual error on the collapse load.

Table 5.1.: Bare arch test - worked example: arch properties

Parameter	**Value**
Span	20 m
Span to rise ratio	4
Number of voussoirs	51
Ring thickness	1.2 m
Shape	segmental
Coefficient of friction	0.6
Coefficient of restitution	0
Unit weight of masonry	20 $kN/m2$

Conclusions

The proposed procedure appears to be reliable in determining the set of values of N_i and Δt providing an accurate prediction of the collapse load. The procedure can be automated but in order to produce accurate simulations at a minimum computational cost a guidance on the selection of N_i for various type of scenarios is required.

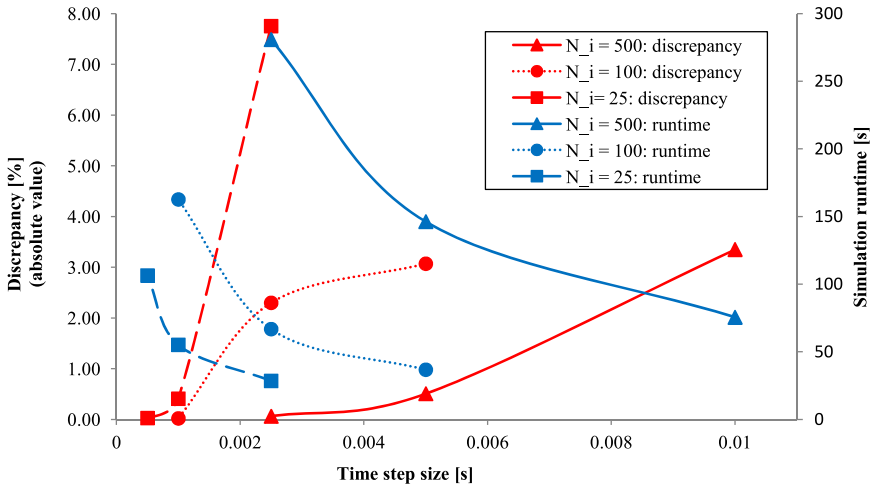

(a)

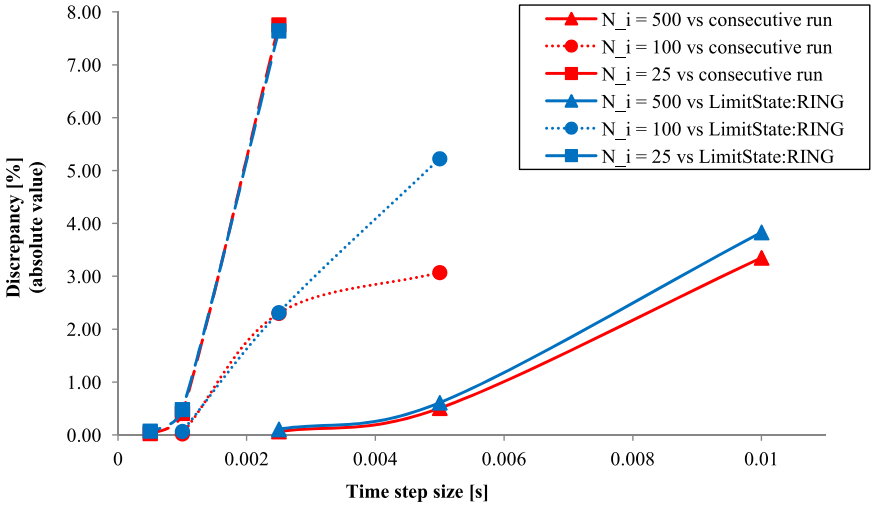

(b)

Figure 5.2.: Bare arch test parametric study: (a) consecutive run discrepancy and runtime (simulations were run on Intel Core i5-2500 processor); (b) consecutive run discrepancy and true discrepancy

5.2.3. A technique to decrease simulation runtime

In quasi-static simulations, the convergence in Box2D, can additionally be improved by making the problem more 'static'; this can be done by increasing the body density so, in a given time step, the tentative velocities are lower for a given force magnitude. Since the correct velocities in quasi-static simulations are close to zero, the lower the tentative velocities, the lower the initial velocity errors that then have to corrected by the constraint solver. In order to preserve physical correctness when using this technique, the gravitational acceleration in the problem has to be decreased proportionally to the increase in the body densities so the bodies keep their correct unit weights. The optimum density of bodies will depend on the simulated scenario. In a test on a very stiff model loaded in a load control mode where the only objective is to find the ultimate load capacity, the density of bodies can be set to a very high level and the proposed technique would provide very significant simulation speed benefits, perhaps of several orders of magnitude; on the other hand in load tests where

the target is to reach a specified deformation of the model, having close to zero velocities in the simulation would mean that it will take more virtual time to complete the simulation and specifying very high density of bodies might be counterproductive. As an example, this technique was used in a simulation of the arch from the worked example from the previous section; the results for $N_i = 25$ are shown in Figure 5.3. By increasing the density by a factor of 100, the maximum Δt that provides the required accuracy increased by a factor of 10 which led to approximately 9 times faster simulation ($12s$ vs $105s$ at the normal density).

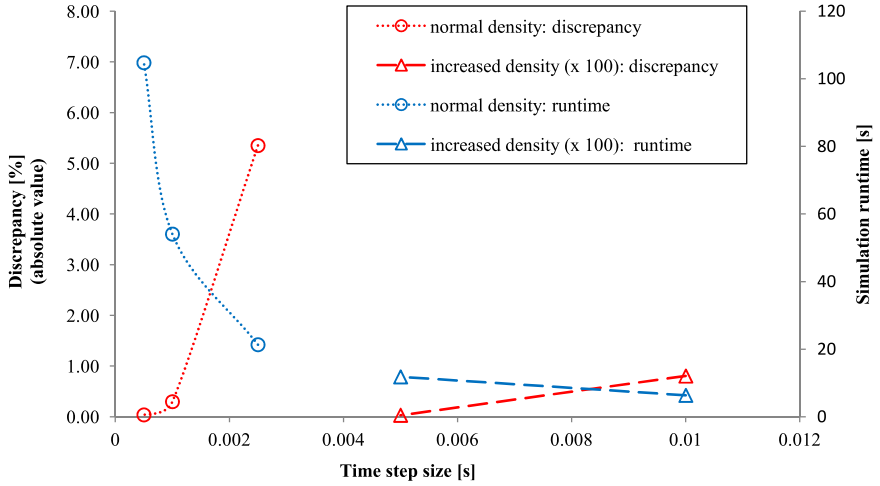

Figure 5.3.: Bare arch test: parametric study on body density; simulations were run on Intel Core i5-2500 processor.

5.2.4. Validation

In order to verify the overall accuracy of the bare arch test program, various bare arch ribs were set up and solved. The models comprised an arch rib with span 20m, ring thickness 1.2m, and comprising voussoirs of unit weight $20kN/m^2$; the following parameters were varied: number of voussoirs in the arch (test series NOV), coefficient of friction of the masonry (COF), span to rise ratio (STRR) and load position (LP). The properties of the default model and the general simulation settings are given in Table 5.2. The values of Δt and N_i were determined using the procedure described in Section 5.2.2 for the test NOV_100 (when referring to a specific test, the name of the test series is followed by an underscore and the value of the parameter varied) which was assumed to be the most computationally challenging simulation as the model comprised the largest number of bodies.

The comparison of the collapse loads from the four test series with those obtained using the LimitState:RING software is given in Figure 5.4 (for clarity, the test LP_0.5 was omitted in Figure 5.4d); for selected tests, the collapse load is also given in Table 5.3 and the corresponding failure mode shown in Figure 5.5.

The accuracy of the Box2D simulations proved to be excellent; in all of the tests the discrepancy on the collapse load between Box2D and LimitState:RING was below 1% and the failure modes identified by the two software were nearly identical. The results of the parametric studies show also that for the adopted arch model:

(i) in general, the higher the number of voussoirs in an arch the lower its load capacity (the more voussoirs, the more potential locations for the hinges)

(ii) above a certain value the coefficient of friction has no influence on the behaviour the arch (approximately 0.4 in the study)

(iii) the flatter the arch, the higher its load capacity (note that sliding of the abutments and crushing of the masonry were not allowed and thus failure modes more likely to occur in shallow arches could not be captured)

(iv) the critical load position for a segmental arch with span to rise of 4 is approximately at its quarter span

Table 5.2.: Bare arch test - validation: simulation input parameters

Parameter	Value
Arch properties - default model	
Span	20 m
Span to rise ratio	4
Number of voussoirs	25
Ring thickness	1.2 m
Shape	segmental
Coefficient of friction	0.6
Coefficient of restitution	0
Unit weight of masonry	20 $kN/m2$
Density of masonry	200,000 $kg/m2$
Load position	0.25 $span$
Test setup: general properties	
Time step size Δt	0.00025 s
Number of velocity iterations per time step N_i	25
Gravity	0.1 m/s^2
Loading rate	0.1 † / 10 ‡ kN/s

† tests COF_0.1 and LP_0.5; ‡ all the other test

Table 5.3.: Bare arch test - validation: parameters varied and failure loads for selected tests

Test	Parameter varied	Value	Failure load		
			Box2D $[kN]$	LimitState:RING $[kN]$	Discrepancy $[\%]$
default	-	-	433.9	432	+0.4
NOV_11	Number of voussoirs	11	519.9	517	+0.5
NOV_100	Number of voussoirs	100	384.9	387	-0.5
COF_0.2	Coefficient of friction	0.2	189.5	190	-0.3
COF_0.3	Coefficient of friction	0.3	352.5	352	+0.1
STRR_2.01	Span to rise ratio	2.01	37.8	37.5	+0.8
STRR_6	Span to rise ratio	6	786.7	784	+0.3
LP_0.1	Load position	0.1 $span$	570.4	569	+0.2
LP_0.5	Load position	0.5 $span$	2288.7	2280	+0.4

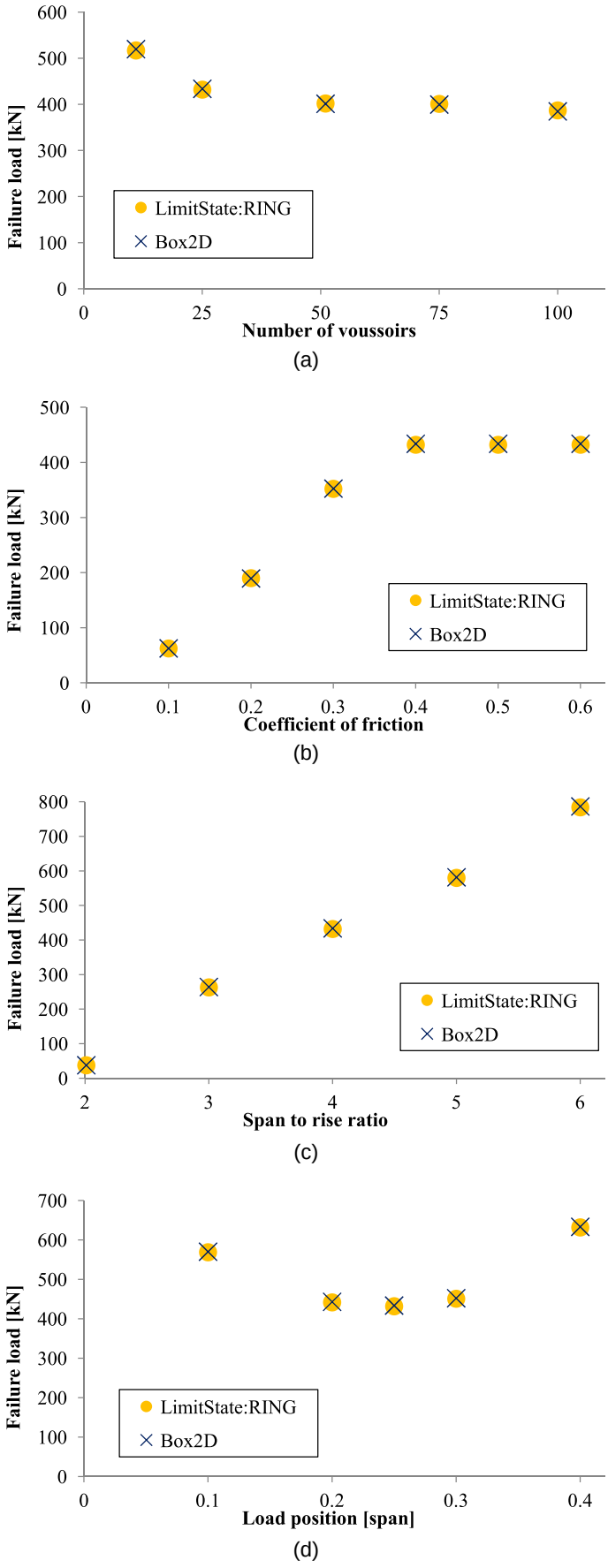

Figure 5.4.: Bare arch test - validation; results for test series: (a) NOV; (b) COF; (c) STRR; (d) LP

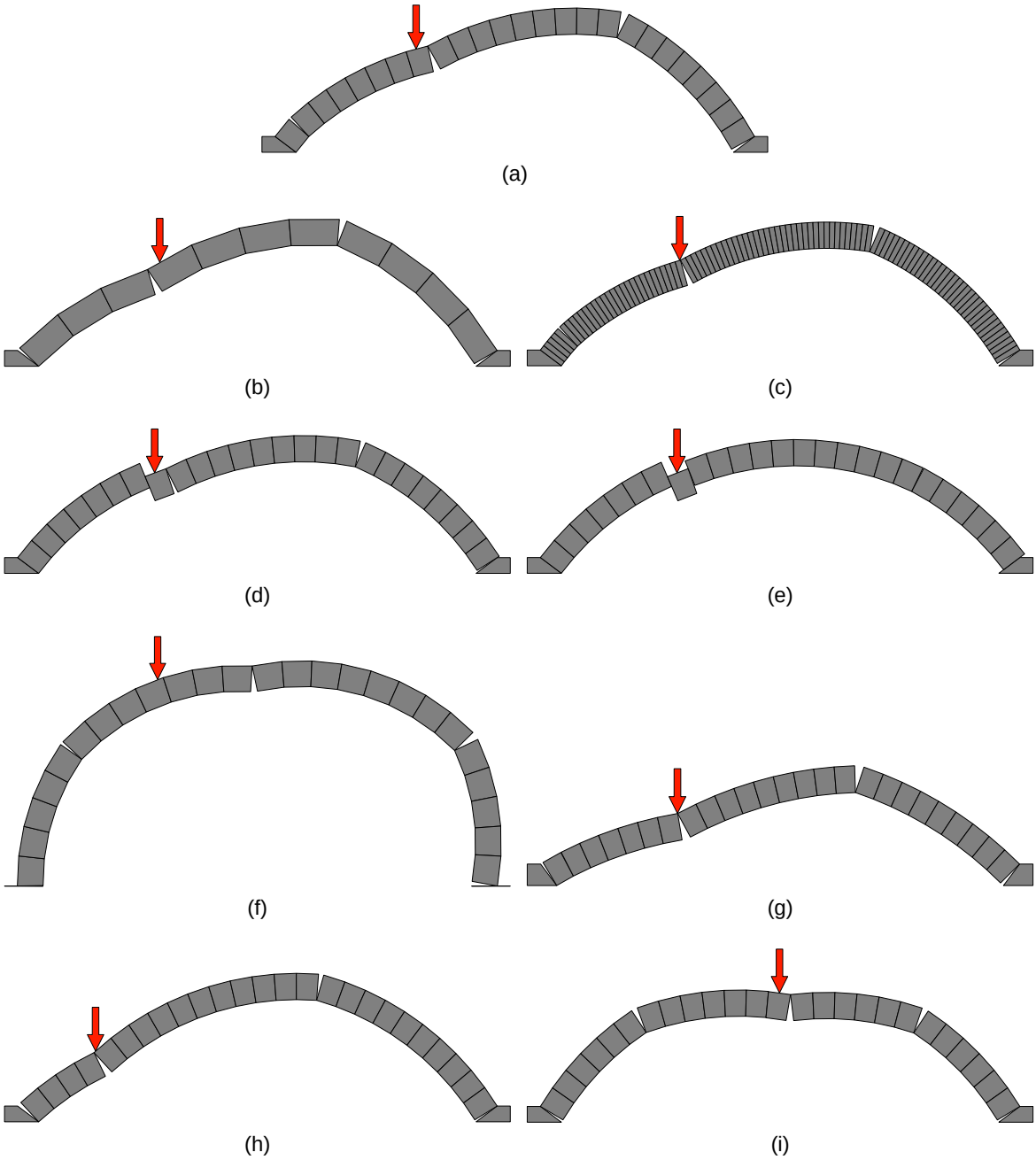

Figure 5.5.: Bare arch test - validation; failure modes for tests: (a) default; (b) NOV_11; (c) NOV_100; (d) COF_0.3; (e) COF_0.2; (f) STRR_2.01; (g) STRR_6; (h) LP_0.1; (i) LP_0.5

5.2.5. Summary

The presented bare arch test has been shown to be capable of accurately simulating load test to failure on voussoir type masonry arches. A method, applicable to any quasi-static Box2D simulation, of determining a set of Δt and N_i which provides an accurate solution was proposed and validated; the method can be automated therefore making Box2D based programs more suitable for engineers. A technique to decrease simulation runtime was proposed; an example showed that the potential reductions in runtime can be very significant.

5.3. Simplified backfilled masonry arch test

The simplified backfilled masonry arch test program allows the simulation of load tests to failure on voussoir type masonry arches backfilled with frictional soils, with the load applied directly to the arch. The program simulates the mobilization of passive and active soil pressures directly, without the need for mobilization factors (which, as explained in Section 2.2, are required when using the limit analysis modelling approach). The live load distribution is not modelled in the presented tests, instead the load is applied at a point on the arch extrados, in the same manner as in the bare arch tests; this approach allows the isolation of the effect of soil pressure mobilization for the purpose of validation. It is envisaged that, if the program is to be used for the assessment of real bridges, the dispersion of live loads can be modelled indirectly using, for example, the Boussinesq model with the calculated distributed load applied directly to the arch extrados (see LimitState (2014*b*) for more details on this approach); the advantage of such approach over the full backfilled arch test, described later in this chapter, would be a significant reduction in the computational cost (the phenomenon of soil pressure mobilization can be simulated accurately with far fewer particles in the model than the load dispersion - see Section 5.4.1 for a short discussion on this). In this section, the test setup is described and the results of example tests are validated.

5.3.1. Test setup

The test is conducted in the following stages:

(i) Create the arch

The arch is modelled with the approach described in Section 5.2.

(ii) Deposition of the backfill

Based on the specified particle size, backfill height, and the position of the side boundaries, the number of particles in the test is calculated automatically; these are then created simultaneously at a random position and at a random orientation within a two dimensional zone; the bottom side of the zone follows the extrados and the floor but is shifted up by 5 d_b; the height of the zone is initially equal to the backfill height but is automatically increased if the program cannot find a non-overlapping position for a particle within the specified number of trials. Once created, the particles are allowed to fall under a reduced gravity. The initial density of the backfill is controlled in the same

manner as in the biaxial compression test i.e. by the particle friction (μ_g) used at the sample generation stage.

(iii) Level the top surface of the backfill

The redundant soil particles are removed from the model.

(iv) Change gravity to the value used during loading (if different from the value used during the deposition stage)

(v) Change particle coefficient of friction to the value used during loading (μ_s)

(vi) Start loading

In the current version of the program, the load is applied at a point in the same manner as in the bare arch test.

(vii) End the test when displacement of the loading voussoir exceeds the specified level.

5.3.2. Backfill model

The soil model adopted in this study was discussed in Sections 4.1 and 4.2; an aspect not discussed before but equally important is the particle size or the number of particles in the backfill model. Frictional backfill in a masonry arch bridge is likely to consist of millions of particles. Including all of them in a model is neither necessary nor computationally feasible. Instead, in order to accurately replicate the desired backfill behaviour, the number of particles in a model must only be sufficient to allow for the correct global failure mechanism to develop, including localizations. In this study, the optimum number of particles in a model is determined by running a series of simulations with the same arch and backfill properties but with the number of particles, controlled by the particle size, doubled in each subsequent run. If the difference in the collapse load between the two consecutive simulations is less than the specified limit, the lower number of particles from this pair of simulations is taken as the optimum.

5.3.3. Example test with dense backfill

Simulation parameters

A 24 voussoir arch, backfilled with dense soil, is loaded at the quarter span. The properties of the arch and the backfill are given in Table 5.4. The bearing capacity of a bare arch of the same properties was determined with the bare arch test and is equal to 412.8 kN. The macro-scale properties of the soil model were determined with the biaxial compression test (see Section 4.2); the mobilization of shear strength with strain is shown in Figure 5.6a; the initial global void ratio in the biaxial compression test was 0.26 which, at the particle unit weight of 26.5 kN/m^2, translates to the bulk unit weight of 21.0 kN/m^2; a similar bulk unit weight of backfill is expected in the backfilled arch tests. The optimum particle size d_b was determined in a parametric study, with the first guess value of 0.48 m which translates to an approximately 1000 soil particles in the model.

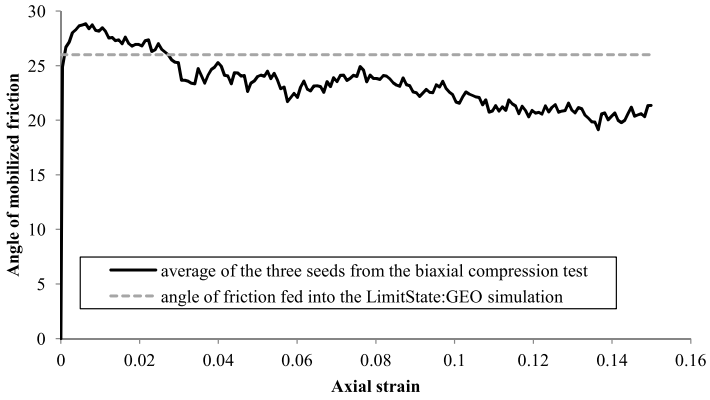

(a)

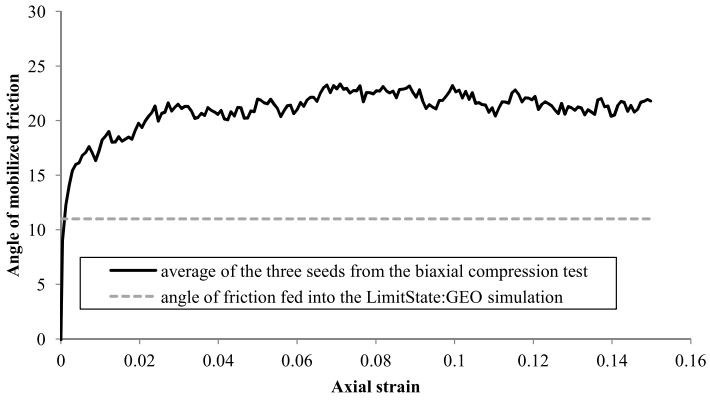

(b)

Figure 5.6.: Angle of friction mobilized in the biaxial compression test: (a) dense backfill material; (b) loose backfill material

The accuracy settings were determined with the procedure described in Section 5.2.2. Note that, as the models contain a large number of bodies, the optimum N_i is also expected to be large, thus a value of 500 is used in all the tests. Following the technique described in Section 5.2.3, in order to reduce the run times, the density of bodies in the tests was increased by a factor of 100 (and, to keep the unit weights constant, the gravitational acceleration was decreased accordingly).

Model with 1000 soil particles ($d_b = 0.48$)

The initial setup of the arch-backfill system is shown in Figure 5.7. Following the procedure to determine the optimum Δt from Section 5.2.2, the collapse load and the consecutive run discrepancy are given in Table 5.5. The discrepancy does not decrease with the decrease in Δt, like in the bare arch test, but instead it fluctuates with the amplitude of up to 7.7%. This means that the accuracy settings are already sufficient for the largest Δt of 0.01s and the discrepancy is caused by the difference in the initial particle arrangement which is expected, because the backfill deposition stage of the test is dynamic in nature and would require a much higher accuracy settings than the quasi-static loading stage if it is to be accurate and repeatable; since, as long as the desired bulk density and fabric of backfill is achieved, there is no need for high accuracy in the backfill deposition stage, Δt of 0.01s is judged to provide

a sufficient accuracy in this test. The load-displacement curve from the test at Δt of 0.01s is shown in Figure 5.8; the full strength of the arch-backfill system is mobilized at a very low displacement of the arch; note that since the load is applied in a load control mode, once the load matches the capacity of the bridge, a catastrophic failure occurs. Figure 5.9a shows the arch-backfill system and the total displacements of particles at 0.6 m displacement of the loading voussoir and Figure 5.10a shows the corresponding accumulated particle rotations. The bridge failed in a four hinge failure mechanism. The mean collapse load at Δt of 0.01s across five simulations with different seeds for the random number generator is 1895 kN with the coefficient of variation of 4.0%; the mean bulk unit weight of the backfill in this set of simulations is 20.7 kN/m^2, slightly lower than the expected value of 21.0 kN/m^2; the difference is likely to be the result of the large particle size used.

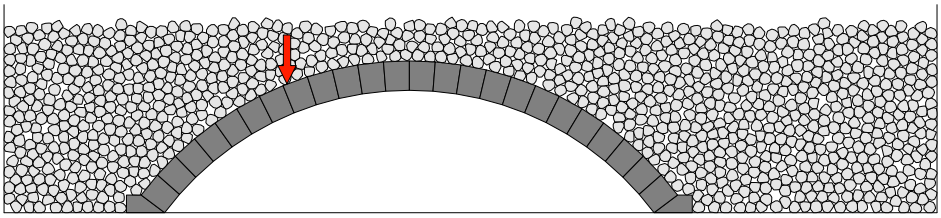

Figure 5.7.: Backfilled arch test with dense backfill: initial setup of the system

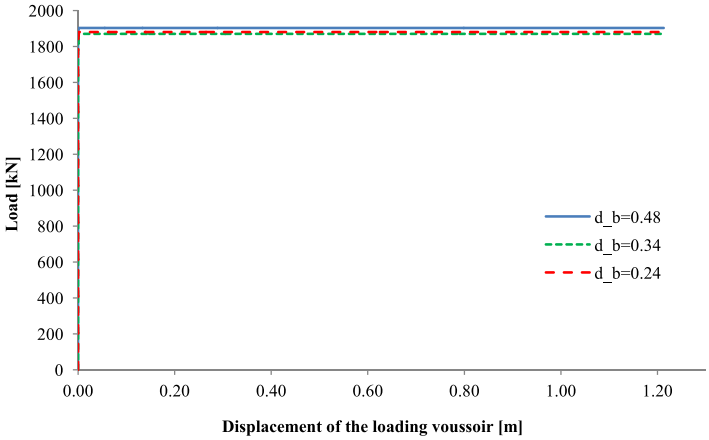

Figure 5.8.: Backfilled arch test with dense backfill: load-displacement curve

Table 5.4.: Backfilled arch test with dense backfill: simulation input parameters

Parameter	Value
Arch properties	
Span	20 m
Span to rise ratio	4
Shape	segmental
Ring thickness	1.2 m
No. of voussoirs	24
μ	0.6
Unit weight	20 kN/m^2
Voussoir density	200,000 kg/m^2
Backfill properties	
Backfill height	8.0 m
Particle unit weight	26.5 kN/m^2
Particle density	265,000 kg/m^2
μ_g	0.2
μ_s	0.6
Size d_b	0.48 / 0.34 / 0.24 m
Approximate number of particles (depends on d_b)	1000 / 2000 / 4000
Loading	
Loading position	1/4 span
Loading rate	100 kN/s
Simulation settings	
Time step size	0.01 / 0.005 / 0.0025 / 0.0001 s
Number of velocity iterations per time step	500
Gravity during backfill deposition stage	0.1 m/s^2
Gravity during loading stage	0.1 m/s^2

Table 5.5.: Backfilled arch test with dense backfill: parametric study on Δt

Particle size d_b $[m]$	Δt $[s]$	**Collapse load** $[kN]$	**Consecutive run discrepancy** ‡ $[\%]$	**CPU runtime** † $[min]$
0.48	0.01	1903	-3.3	35
	0.005	1967	+7.7	81
	0.0025	1816	-3.6	143
	0.001	1881	—	428
0.34	0.01	1871	-2.4	79
	0.005	1917	+3.4	226
	0.0025	1852	-6.2	451
	0.001	1968	—	1278
0.24	0.01	1881	-3.2	447
	0.005	1942	+3.5	792
	0.0025	1874	—	1194

† Simulations were run on either Intel X5650 or Intel E5 2650V2 processor; Box2D is a single threaded physics engine.
‡ Calculated from Equation 5.1.

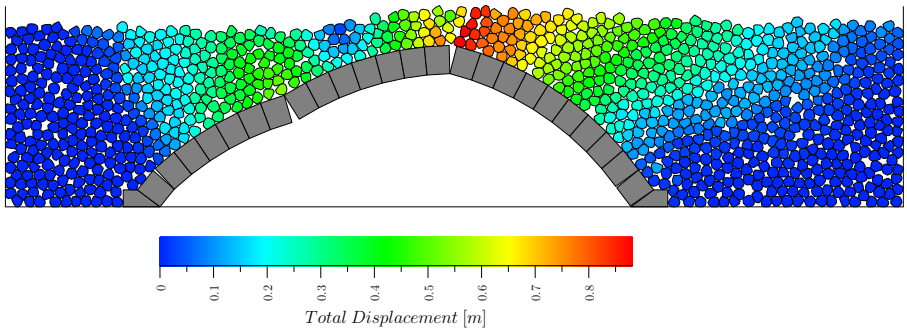

(a)

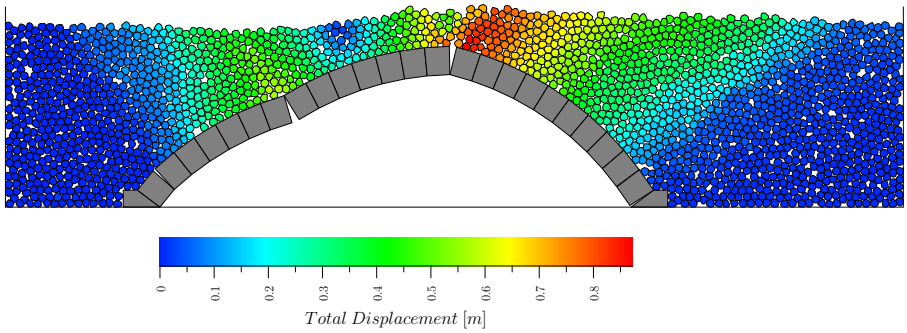

(b)

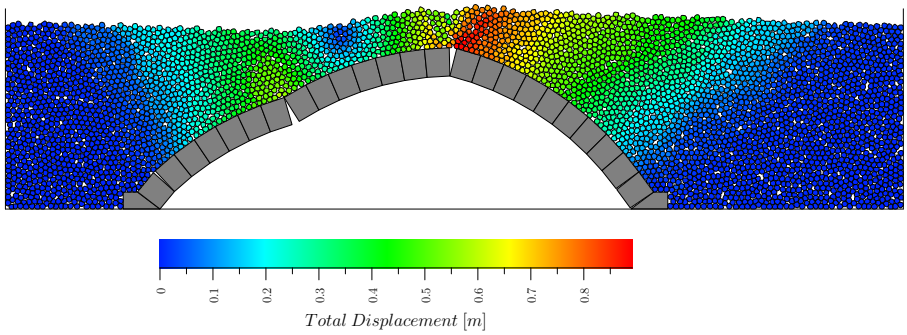

(c)

Figure 5.9.: Backfilled arch test with dense backfill; deformed shape and displacements of soil particles at 0.6m displacement of the loading voussoir: (a) $d_b = 0.48$; (b) $d_b = 0.34$; (c) $d_b = 0.24$

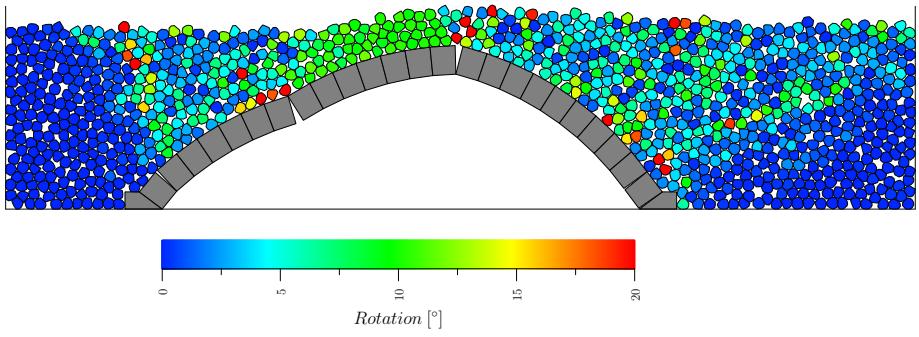

(a)

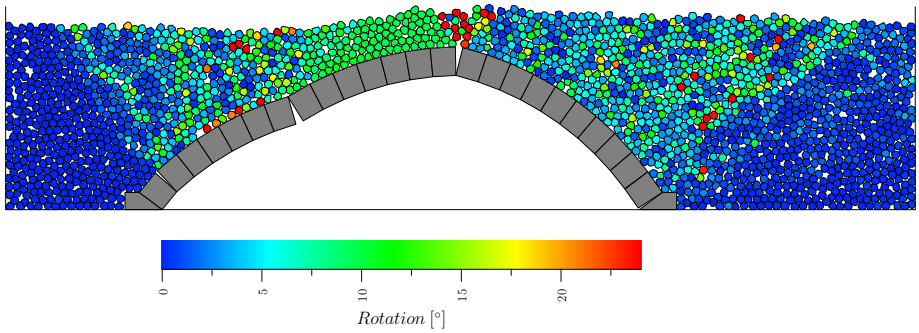

(b)

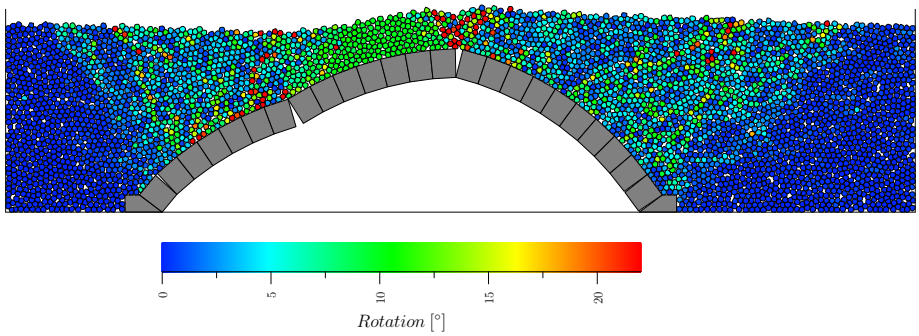

(c)

Figure 5.10.: Backfilled arch test with dense backfill; deformed shape and accumulated particle rotations at 0.6 m displacement of the loading voussoir: (a) $d_b = 0.48$; (b) $d_b = 0.34$; (c) $d_b = 0.24$

Models with 2000 ($d_b = 0.34$) and 4000 ($d_b = 0.24$) soil particles

The collapse load and the consecutive run discrepancy for both models are given in Table 5.5; similar fluctuations as for the model with $d_b = 0.48$ can be observed in both cases; for both models Δt of 0.01s provides a sufficient accuracy of the loading stage of the test. The load displacement curves from the tests with Δt of 0.01s are shown in Figure 5.8; again in both cases the behaviour is almost identical to the model with $d_b = 0.48$ with the full strength of the system mobilized at a very low deformation of the arch. Figures 5.9b and 5.9c show the arch-backfill system and the total displacements of particles at 0.6 m displacement of the loading voussoir for d_b of 0.34 and 0.24 respectively whilst Figures 5.10b and 5.10c show the corresponding accumulated particle rotations respectively for the two values of d_b. The failure mechanisms in both models are almost identical; compared to the model with $d_b = 0.48$, the volume of soil involved in shearing on the passive side appears to be slightly lower in both cases.

For each of the two values of d_b, the test at $\Delta t = 0.01s$ was run four additional times with different seeds; the collapse load and the initial bulk unit weight of backfill for all the simulations are given in Table 5.6. Across the three values of d_b, the mean collapse load varies by about 5%; the coefficient of variation is lower for models with larger number of particles and therefore the corresponding results can be considered to be more accurate. The bulk unit weight in the test with d_b of 0.34 is exactly the same as in the biaxial compression test and in the tests with d_b of 0.24 and 0.48 it is very close to this value (+1.0% and - 1.4% respectively).

Overall, the difference in the behaviour of the system between models with d_b of 0.24, 0.34 and 0.48 is very small.

Table 5.6.: Backfilled arch test with dense backfill: initial bulk unit weight of backfill and collapse load (given in units of kN/m^2 and kN respectively)

d_b $[m]$	Seed 1	Seed 2	Seed 3	Seed 4	Seed 5	Mean	Coefficient of variation $[\%]$
Bulk unit weight of backfill							
0.48	20.6	20.6	20.6	20.9	20.6	20.7	0.6
0.34	21.0	21.1	21.0	21.1	21.0	21.0	0.2
0.24	21.2	21.2	21.2	21.2	21.2	21.2	0.1
Collapse load							
0.48	1903	1748	1939	1926	1958	1895	4.0
0.34	1932	2019	2009	1979	1954	1979	1.7
0.24	1881	1940	1968	1936	1881	1921	1.8

Validation against LimitState:GEO

The very stiff behaviour of the arch-backfill system modelled in Box2D (see Figure 5.8) allows the shear strength of the backfill mobilized at the point of failure of the bridge, ϕ_{mob}, to be accurately estimated using the results from the biaxial compression test i.e. assuming that the macro-scale behaviour of the virtual soil is the same in the biaxial compression test

and in the simplified backfilled arch test, ϕ_{mob} is approximately equal to the very-small-strain strength from the biaxial compression test (indicated in Figure 5.6a with the dashed line).

LimitState:GEO (LimitState, 2015*a*) is a commercial limit analysis software which has been rigorously validated for a range of geotechnical problems (see LimitState (2015*b*) for more details) and is capable of modelling both the backfill and the arch directly . It has been used for the analysis of masonry arch bridges (Gilbert et al., 2010) albeit it is more of an academic purpose tool in this regard. The main disadvantage of LimitState:GEO when used in the analysis of masonry bridges is that to model the passive soil pressures correctly, it requires the use of empirical mobilization factors; their use could be avoided only if ϕ_{mob} was known which is very unlikely for a real structure. As explained above, this condition is however satisfied in the presented Box2D simulations which makes LimitState:GEO a suitable candidate for a validation tool in this study.

The geometry of the arch and the backfill in the LimitState:GEO model were as in the Box2D simulations. The masonry blocks were modelled with a rigid material type with the unit weight set to 20 kN/m^2, same as in the Box2D models. The masonry joints were modelled with a mixed material consisting of cutoff material type with tensile and compressive limiting stresses set to 0 and 25,000 kN/m^2 respectively and Mohr-Coulomb material type with angle of friction (ϕ') set to 31° (which is equivalent to the μ of 0.6 used in the Box2D model). The backfill was modelled with a Mohr-Coulomb material type with the unit weight of 21.0 kN/m^2, as the initial value in the biaxial compression test and very close to or the same as the initial value in the Box2D backfilled arch simulations, ϕ' set to 26° and zero cohesion; the specified angle of friction, as shown in Figure 5.6a, is equal to the shear strength mobilized at a very low strain in the biaxial compression test (i.e. the assumed ϕ_{mob}). The soil-arch interface was modelled with the Derived Mohr-Coloumb material (i.e. the properties of the interface were derived from those of the adjacent soil) with the multiplier on $\tan\phi'$ set to 0.33, the same value as used in the models reported in Gilbert et al. (2010). The load was applied at the quarter span directly to the brick. The model was solved with the target number of nodes set to 4000 and the baseline nodal spacing on the arch joints set to 0.1. These accuracy settings were judged to be sufficient as the difference in the collapse load between simulations with 4000 and 2000 nodes was only 1%.

The collapse load in the LimitState:GEO simulation was 1941 kN; this is within the range of Box2D results reported in Table 5.6 and only 1.0% higher than the mean for $d_b = 0.24$ which has the lowest coefficient of variation of the three models. The failure mechanism, shown in Figure 5.11, is also very similar to mechanisms obtained in the Box2D simulations.

Figure 5.11.: Backfilled arch test with dense backfill: failure mode in LimitState:GEO

5.3.4. Example test with loose backfill

Simulations

A 24 voussoir arch, backfilled with loose soil, is loaded at the quarter span. The properties of the arch and the backfill are the same as in the test with dense backfill apart from μ_g which was set to 0.6. The macro-scale properties of the backfill were determined with the biaxial compression test; the mobilization of shear strength with strain is shown in Figure 5.6b; the initial global void ratio in the biaxial compression test was 0.31, which at the particle unit weight of 26.5 kN/m^2, translates to the bulk unit weight of 20.2 kN/m^2. The same procedures for determining the optimum particle size and the accuracy settings as in the test with dense backfill were employed. The initial setup of the arch-backfill system with d_b of 0.48 is shown in Figure 5.12. Following the procedure to determine the optimum Δt, the collapse load and the consecutive run discrepancy for the models with the three values of d_b are given in Table 5.7. Similar fluctuations in discrepancy as in the tests with dense backfill can be observed but for d_b of 0.48 and 0.34 the amplitudes are larger, reaching up to 10%; Δt of 0.01s provides a sufficient accuracy for all the three models. The load-displacement curve from the tests at Δt of 0.01s is shown in Figure 5.13; the full strength of the the arch-backfill system is mobilized at a very low displacement of the arch, the same behaviour as in the tests with dense backfill.

Figures 5.14a, 5.14b and 5.14c show the arch-backfill system and the total displacements of particles at 0.6 m displacement of the loading voussoir for d_b of 0.48, 0.34 and 0.24 respectively whilst Figures 5.15a, 5.15b and 5.15c show the corresponding accumulated particle rotations respectively for the three values of d_b. The arch failed by transformation to a four hinge mechanism. Compared to each other, the failure mechanisms are very similar. Compared to the models with dense backfill, the failing block of soil is larger on the active side and smaller on the passive side which is expected for a backfill with lower shear strength.

For each of the three values of d_b, the test at $\Delta t = 0.01s$ was run four additional times with different seeds; the collapse load and the initial bulk unit weight of backfill for all the simulations are given in Table 5.8. Across the three models, the mean collapse load varies only by about 0.8 % which gives confidence in the accuracy of the simulations. The mean bulk unit weight of backfill in the tests with d_b of 0.24 and 0.34 is very close to the value obtained in the biaxial compression test of 20.2 kN/m^2 (+0.3% and -0.5% respectively); the

difference is slightly larger for $d_b = 0.48$ but this can be attributed to the large particle size used.

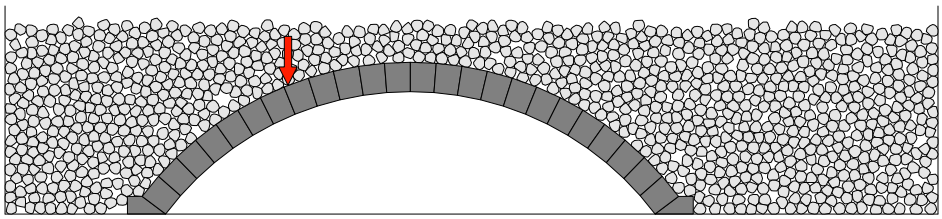

Figure 5.12.: Backfilled arch test with loose backfill: initial setup of the system

Table 5.7.: Backfilled arch test with loose backfill: parametric study on Δt

Particle size d_b $[m]$	Δt $[s]$	**Collapse load** $[kN]$	**Consecutive run discrepancy**‡ $[\%]$	**CPU runtime** † $[min]$
0.48	0.01	1357	-7.4	38
	0.005	1458	+2.7	84
	0.0025	1418	-7.2	159
	0.001	1520	—	383
0.34	0.01	1456	+6.5	153
	0.005	1361	-10.2	231
	0.0025	1500	+6.9	317
	0.001	1396	—	1168
0.24	0.01	1425	+1.6	340
	0.005	1403	-1.5	456
	0.0025	1424	—	1455

† Simulations were run on either Intel X5650 or Intel E5 2650V2 processor; Box2D is a single threaded physics engine.
‡ Calculated from Equation 5.1

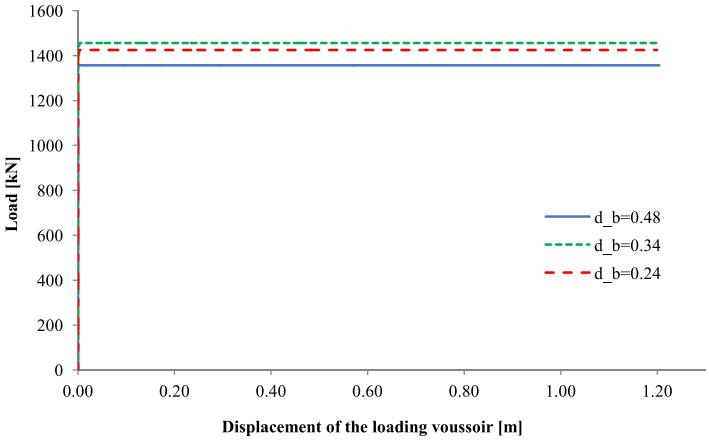

Figure 5.13.: Backfilled arch test with loose backfill: load-displacement curve

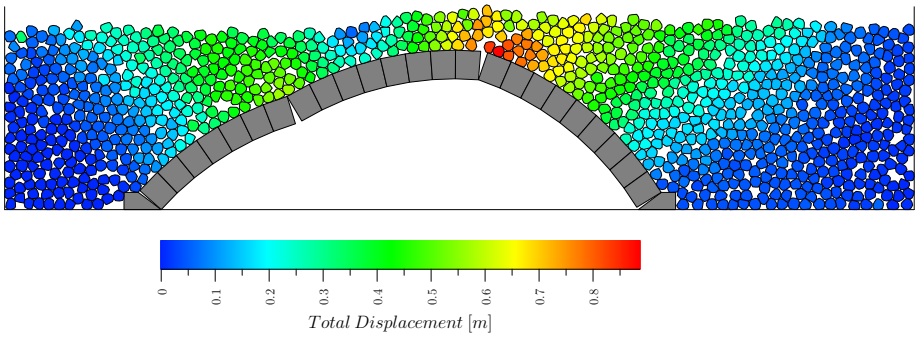

(a)

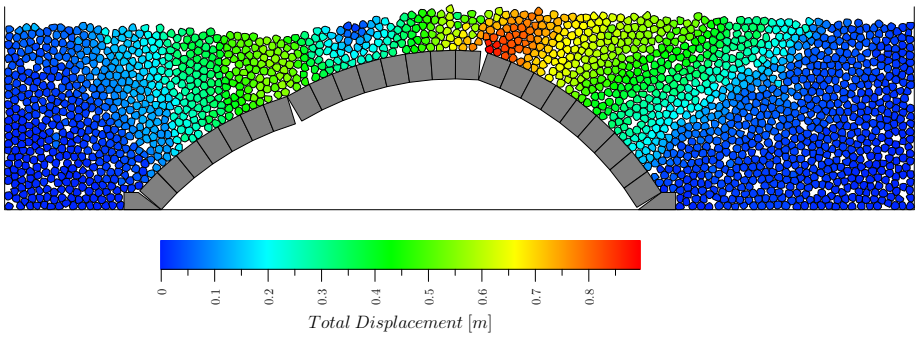

(b)

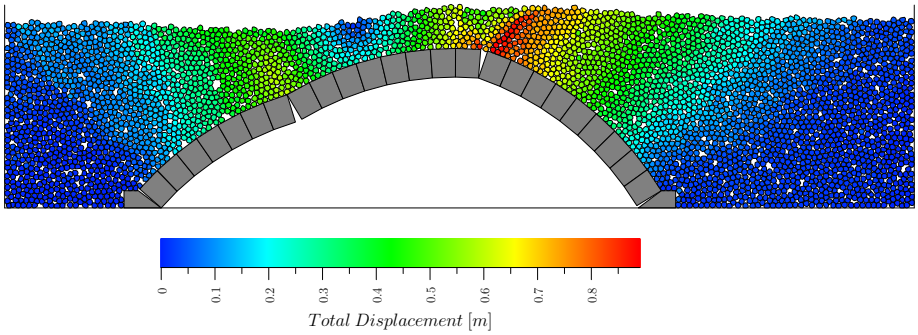

(c)

Figure 5.14.: Backfilled arch test with loose backfill; deformed shape and displacements of soil particles at 0.6m displacement of the loading voussoir: (a) $d_b = 0.48$; (b) $d_b = 0.34$; (c) $d_b = 0.24$

Table 5.8.: Backfilled arch test with loose backfill: initial bulk unit weight of backfill and collapse load (given in units of kN/m^2 and kN respectively)

d_b $[m]$	Seed 1	Seed 2	Seed 3	Seed 4	Seed 5	Mean	Coefficient of variation $[\%]$
Bulk unit weight of backfill							
0.48	19.8	19.7	20.0	19.8	19.7	19.8	0.6
0.34	20.0	20.1	20.1	20.1	20.1	20.1	0.2
0.24	20.2	20.3	20.2	20.3	20.2	20.3	0.2
Collapse load							
0.48	1357	1449	1507	1447	1498	1452	3.7
0.34	1456	1416	1471	1462	1410	1443	1.7
0.24	1425	1414	1482	1435	1451	1441	1.6

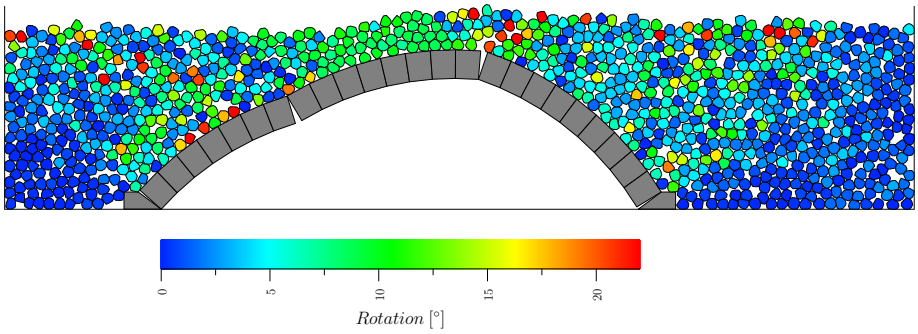

(a)

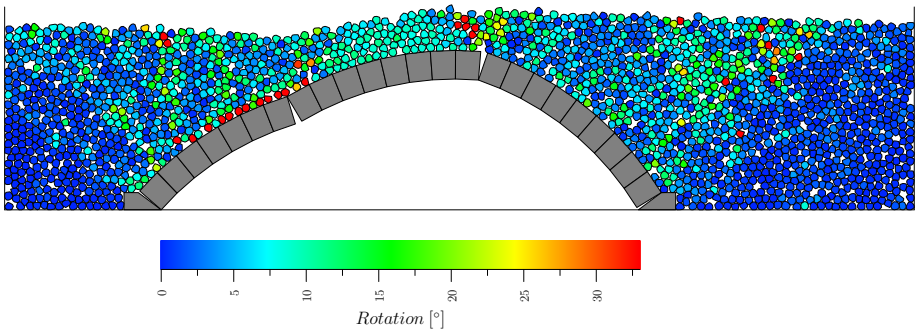

(b)

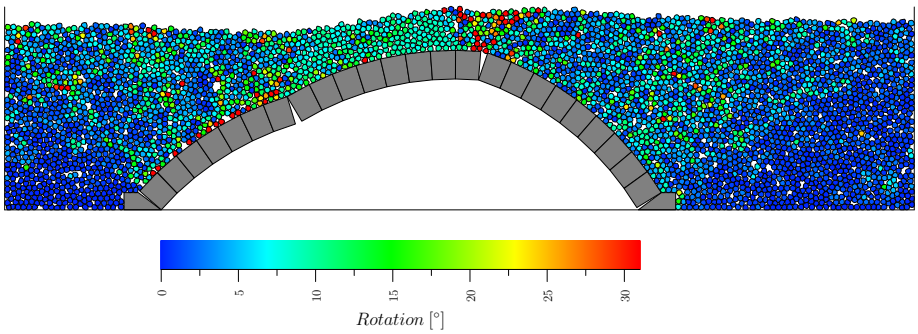

(c)

Figure 5.15.: Backfilled arch test with loose backfill; deformed shape and accumulated particle rotations at 0.6 m displacement of the loading voussoir: (a) $d_b = 0.48$; (b) $d_b = 0.34$; (c) $d_b = 0.24$

Validation against LimitState:GEO

The LimitState:GEO model had the same properties as in the example with dense backfill with the exception of unit weight and angle of friction of the backfill which were set to 20.2 kN/m^2 and 11° respectively; the unit weight is the same as the initial value in the biaxial compression test and the angle of friction, as shown in Figure 5.6b, is equal to the shear strength mobilized at a very low strain in the biaxial compression test.

The collapse load in the LimitState:GEO simulation was 1456 kN which is extremely close the values obtained in the Box2D simulations (+0.2 %, +0.9% and 1.0% for d_b of 0.48, 0.34 and 0.24 respectively). The failure mechanism is shown in Figure 5.16. The plastic hinges within the arch are located at the same places as in the Box2D simulations and the volume of failing blocks of soils is approximately similar. The differences between the amount of soil involved in the failure mechanism between the LimitState:GEO simulations of models with loose and dense backfill are similar to those observed when comparing the results of the respective Box2D simulations i.e. a bigger block of soil on the active side and a smaller block of soil on the passive side are failing in the system with the loose backfill.

Figure 5.16.: Backfilled arch test with loose backfill: failure mode in LimitState:GEO

5.3.5. Summary

The simplified backfilled masonry arch test has been described. The program allows the modelling of load tests to failure on voussoir type masonry arches backfilled with frictional soil; in order to significantly reduce the runtime, the live load distribution in the backfill is not modelled directly, instead the load is applied directly to the arch.

The initial bulk unit weight of the backfill in the example tests was essentially the same as in the biaxial compression tests, for both the loose and dense backfill, which means that (i) the utilized deposition method is reliable across different simulated scenarios and (ii) the backfill in the arch tests had the same micro-scale properties as in the respective biaxial compression tests.

The results of the example tests, with both the loose and dense backfill, are in an excellent agreement with the LimitState:GEO validation tests which were conducted without the use of empirical mobilization factors but, instead, with the backfill strength input taken directly from the virtual biaxial compression test (possible because of the initial very high stiffness of the soil model); this indicates that:

(i) The macro-scale behaviour of the Box2D soil model, with given micro-scale properties specified in the simulation, is independent of the simulated scenario.

(ii) The biaxial compression test program provides a good prediction of the behaviour of the backfill in the backfilled masonry arch tests.

(iii) Providing the macro-scale properties of the soil model obtained in the virtual biaxial compression test match the properties of a real backfill, the simplified backfilled masonry arch test program can be a reliable tool for the analysis of masonry arch bridges with frictional backfill at a reasonable runtime of less than 40 min.

(iv) The method of determining a set of Δt and N_i which provides an accurate solution described in Section 5.2.2 is applicable to the masonry arch tests with backfill but the parametric study must include at least three simulations in order to determine whether the observed discrepancies are due to an inaccuracy or fluctuations caused by the difference in the initial arrangement of soil particles.

(v) The technique to decrease simulation runtime described in Section 5.2.3 can be successfully used in the masonry arch tests with backfill.

Currently the program allows application of load only at a point but the uniform and the Boussinesq load dispersion models can be implemented relatively easily in the same manner as described in LimitState (2014*b*).

5.4. Full backfilled masonry arch test

The full backfilled arch test program simulates load test to failure on voussoir type masonry arches backfilled with frictional soil, with load applied via a loading beam in a displacement control mode; a test setup typical for laboratory tests on masonry arch bridges. The program simulates all aspects of soil and arch behaviour directly including live load distribution in the backfill.

In this section, the test setup is described and the results of an example test are discussed.

5.4.1. Test description

The test setup is the same as in the simplified backfilled arch test except for the loading conditions. The load is applied via a weightless loading beam in a displacement control mode. The beam is created once the backfill deposition stage is finished and initially is set out-of contact with the soil; in the test, it travels vertically at a constant specified velocity and is not allowed to rotate. The test is ended when displacement of the loading beam exceeds the specified level.

Direct modelling of live load distribution in the backfill necessitates the use of much finer soil particles in the model compared to the simplified backfilled arch test. The required size of particles will depend on the width of the loading beam; following recommendation

by Garnier et al. (2007) for studies on bearing capacity of strip footings (the loading beam essentially acts as a strip footing in this test) maximum allowable d_b should be calculated from $d_b = B/35$ where B is the width of the loading beam.

In a simulation of a real structure, B should be equal to the width of the surface of the backfill subjected to the assumed live load; for example, assuming a highway bridge and a load applied to the road surface by a single axle over a width of $0.3m$ and dispersed through a $0.5m$ thick structure of the road at a slope of 2 vertical to 1 horizontal, $B = 0.8m$ should be used in the simulation (see Highways Agency (2001*b*) for a guidance on the loading assumptions in the assessment of highway masonry arch bridges). However, for the geometry of the model from Section 5.3.3 and $d_b = B/35$ this would result in approximately 88,000 particles in a model and a runtime of many days. The computational cost of the full backfilled arch test can significantly be reduced by using the very fine particles only in the vicinity of the loading beam but implementing this technique is out of scope of this study. Here, instead, a much wider loading beam will be used, with B perhaps not realistic for a typical bridge but still suitable for the purpose of validation and demonstration of the program, and the recommendation by Garnier et al. (2007) will not strictly be adhered to.

5.4.2. Example test

Simulation input parameters

The simulation input parameters of the example test are given in Table 5.9; the geometry of the model, the properties of the arch and the properties of the backfill are the same as in the simplified backfilled arch test with dense backfill described in Section 5.3.3. The particle size d_b was set to 0.24 m which, as proved in the section on the simplified backfilled arch test, is sufficient to model correctly the passive and active pressures in the backfill. The loading beam had a width of 4.0 m (which gives B/d_b of 16.7, slightly less than half of the value recommended by Garnier et al. (2007)) and its centreline was positioned at the quarter span. The initial setup of the arch-backfill system is shown in Figure 5.17.

Note that, since the time step size is subject to a parametric study, the choice of the movement rate is of small importance; this is because, in a quasi-static simulation, it is the displacement increment per time step that matters and not the physical magnitude of the movement rate in m/s. The value of the movement rate of the loading beam in this test was selected with a view to ensure the displacement increment per time step for the initial time step size was very small compared to the size of the soil particles (approximately 0.0001 d_b).

The consecutive run discrepancy on the collapse load of the system for Δt of 0.01s was only +1.7$\%$, and it was judged that this time step size provides a sufficient accuracy.

Results

Figure 5.18a shows the strength of the system mobilized with displacement of the loading beam; the corresponding displacement of the arch and the strength of the system mobilized with displacement of the arch are shown in Figures 5.18b and 5.18c respectively. Let x

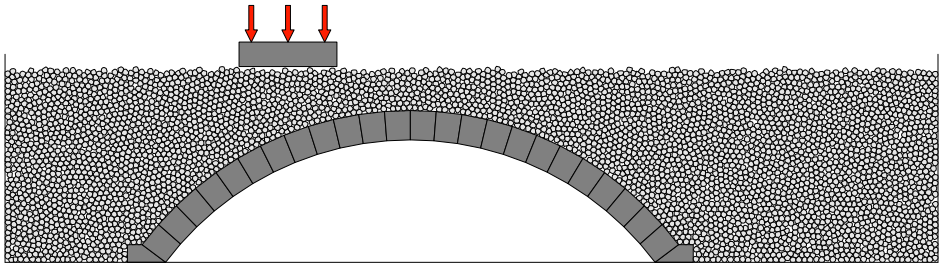

Figure 5.17.: Full backfilled arch test: initial setup of the system

be the displacement of the loading beam. The contact between the loading beam and the backfill was established approximately at $x = 0.035m$; initially, there was one-point contact, building to multiple contacts and the build up of load which lead to a distinctive local peak of 1502kN at $x = 0.095m$. Initially, there is zero deformation of the arch; it starts to deform only at $x = 0.12m$ with the load reaching its global peak almost immediately. After the load peak, the deformation of the arch is roughly proportional to x and the load capacity of the system gradually deteriorates.

Figure 5.19a shows the system and the particle displacements at $x = 0.1m$ and Figure 5.20a shows the corresponding particle rotations; the soil was displaced only in the vicinity of the loading beam and the deformation patterns closely resembled those typical for a bearing capacity failure. The system and the particle rotations at $x = 0.6m$ are shown in Figure 5.20b; the corresponding displacements of the soil particles are shown in Figure 5.19b. The global failure of the system involved formation of four hinges in the arch and similar soil deformation patterns as in the simplified backfilled arch tests; compared to the simplified backfilled arch tests with dense soil, the volume of soil displaced on the passive side is similar but on the active side it is larger and the top part of it has a distinctive shape typical for a bearing capacity failure; the locations of the plastic hinges in the arch are also slightly different.

The presented test results suggest that prior to the global failure of the system, a local bearing capacity failure under the loading beam occurred and that the local peak in the load registered at $x = 0.095m$ is the bearing capacity of the loading beam; however, Figure 5.19b suggests that this local failure did not lead to significant soil deformations; it most likely ceased to occur once the arch started to deform and the global failure mode of the system was initiated.

In order to check repeatability, four more simulations with the same model properties but with different seeds for the random number generator were run. As shown in Figure 5.21, in each of the simulations, a local bearing failure of the loading beam was observed in the early stage of the test. The mean load capacity of the system, the bearing capacity of the loading beam and the initial bulk unit weight of the backfill are given in Table 5.10. Compared to the the simplified backfilled arch test, the bulk unit weight is almost exactly the same; the collapse load is significantly higher (2650 kN vs 1921 kN) which is the expected result of the load being applied at a section of the arch through the backfill, as opposed to at a point.

The coefficient of variation on the load capacity of the system is larger than in the simplified backfilled arch tests with $d_b = 0.24$ but comparable to those with d_b of 0.48. There is

however, much more variability with respect to the local bearing failure of the loading beam, both in terms of the collapse load and the mechanisms; this is most likely caused by a relatively low number of particles facilitating the bearing capacity failure of the beam (i.e. as the failure mode involves only a small part of the global assembly of soil particles).

Table 5.9.: Full backfilled arch test: simulation input parameters

Parameter	Value
Simulation settings	
Time step size	0.01 / 0.005 s
Number of velocity iterations per time step	500
Gravity during backfill deposition stage	0.1 m/s^2
Gravity during loading stage	0.1 m/s^2
Arch properties	
Span	20 m
Span to rise ratio	4
Shape	segmental
Ring thickness	1.2 m
No. of voussoirs	24
μ	0.6
Voussoir density	200,000 kg/m^2
Unit weight	20 kN/m^2
Backfill properties	
Backfill height	8.0 m
Particle unit weight	26.5 kN/m^2
Particle density	265,000 kg/m^2
μ_g	0.2
μ_s	0.6
Size d_b	0.24 m
Approximate number of particles (depends on d_b)	4000
Loading beam	
Position	1/4 span
Width	4.0 m
Movement rate	0.0025 m/s
Unit weight	0 kN/m^2
μ	0.6

Table 5.10.: Full backfilled arch test: results

Quantity	**Mean**	**Coefficient of variation**
Load capacity of the system	2650 kN	5.7 $\%$
Bearing capacity of the loading beam	1555 kN	14.5 $\%$
Bulk unit weight of backfill	21.17 kN/m^2	0.1 $\%$
CPU runtime †	871 min	22.0 $\%$

† Simulations were run on either Intel X5650 or Intel E5 2650V2 processor; Box2D is a single threaded physics engine.

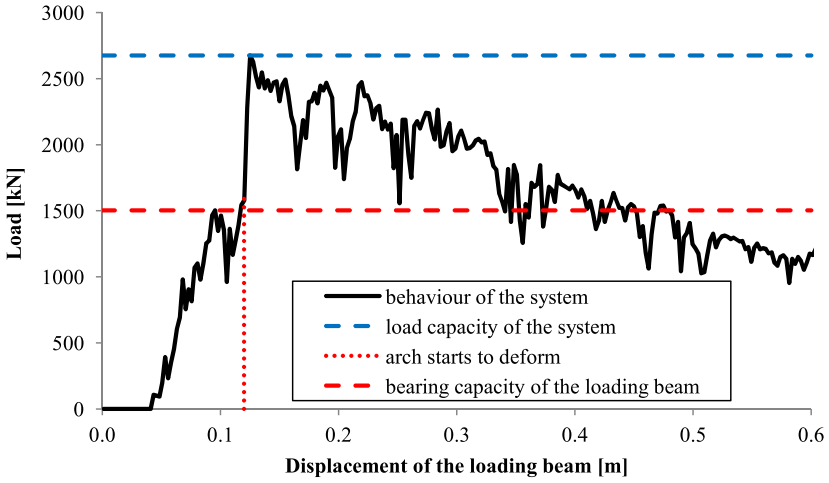

(a)

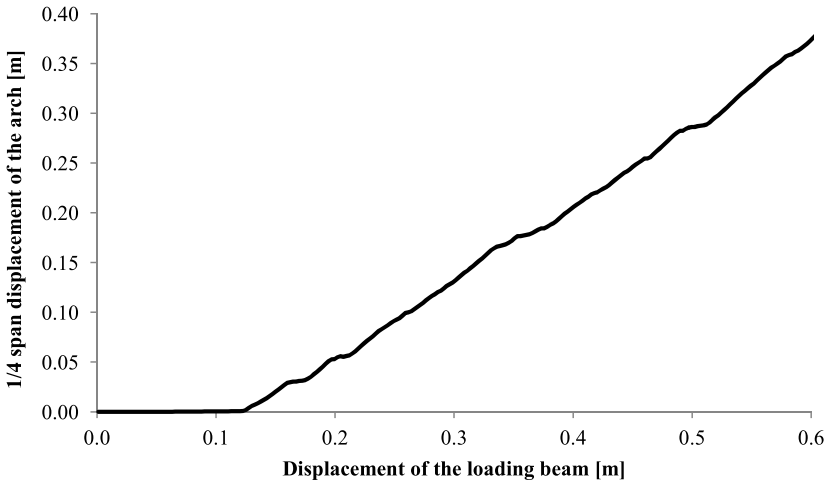

(b)

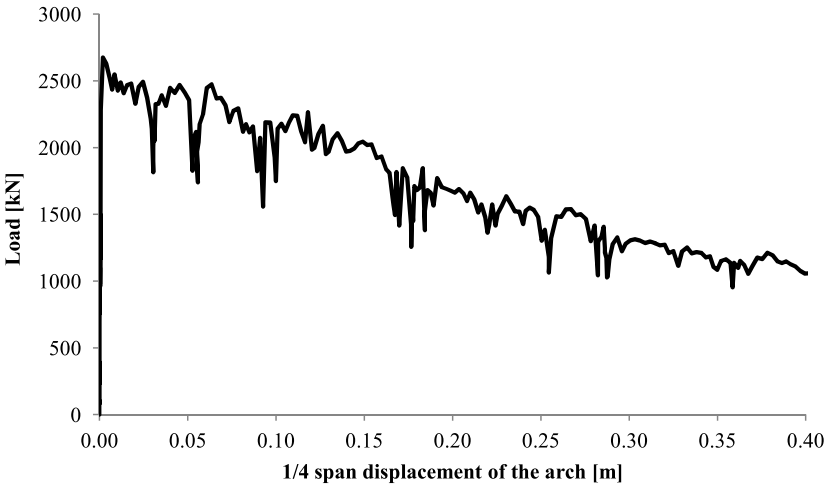

(c)

Figure 5.18.: Full backfilled arch test; system response (each point shown is an average over 1s of the simulation): (a) load v. displacement of the loading beam; (b) displacement of the arch v. displacement of the loading beam; (c) load v. displacement of the arch

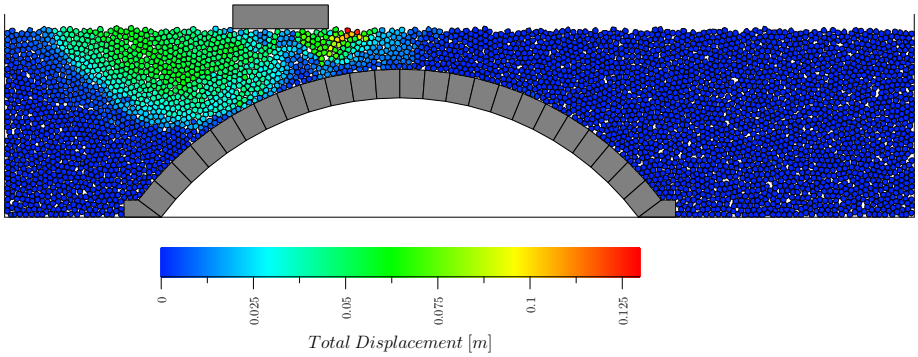

(a)

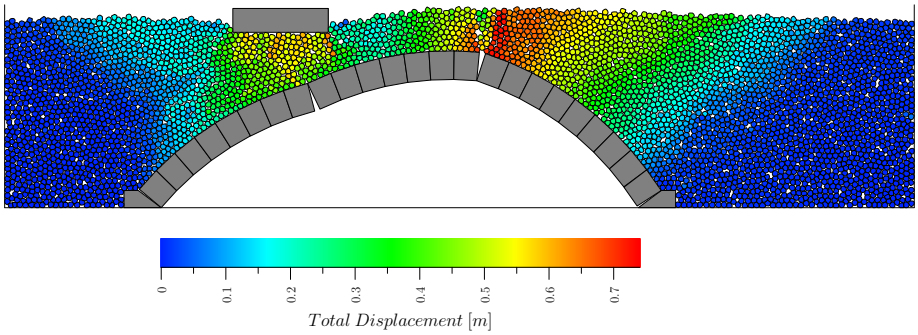

(b)

Figure 5.19.: Full backfilled arch test; deformed shape and particle displacements at: (a) $x = 0.1m$; (b) $x = 0.6m$

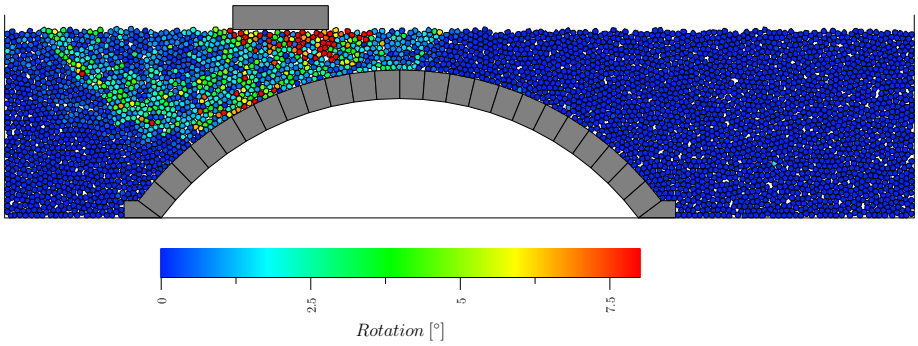

(a)

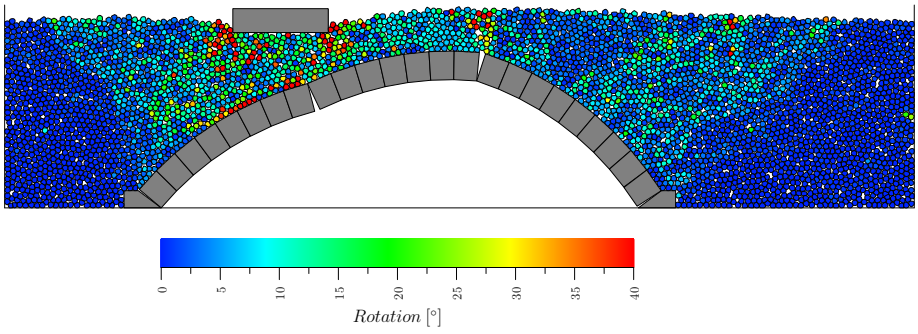

(b)

Figure 5.20.: Full backfilled arch test; deformed shape and accumulated particle rotations at: (a) $x = 0.1m$; (b) $x = 0.6m$

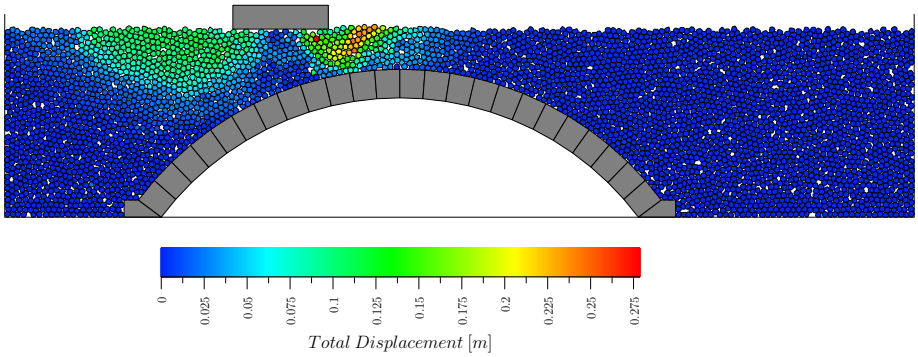

(a)

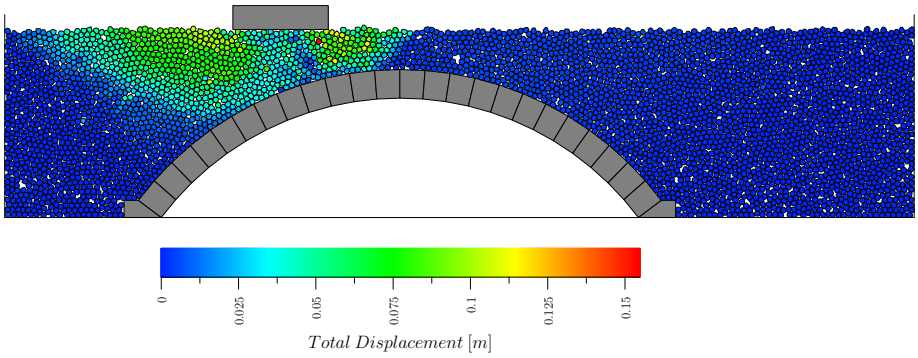

(b)

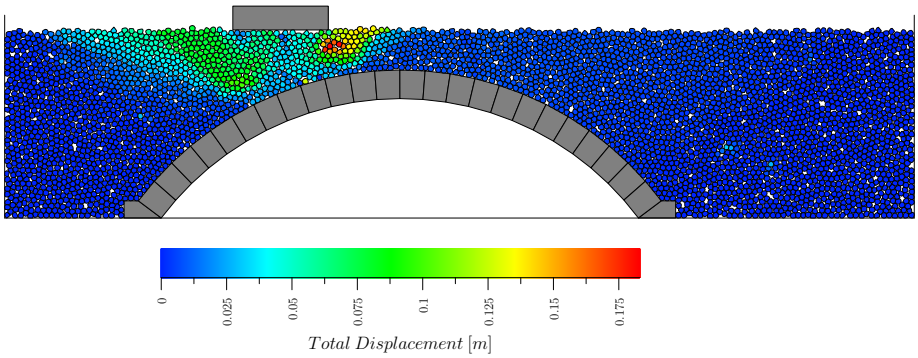

(c)

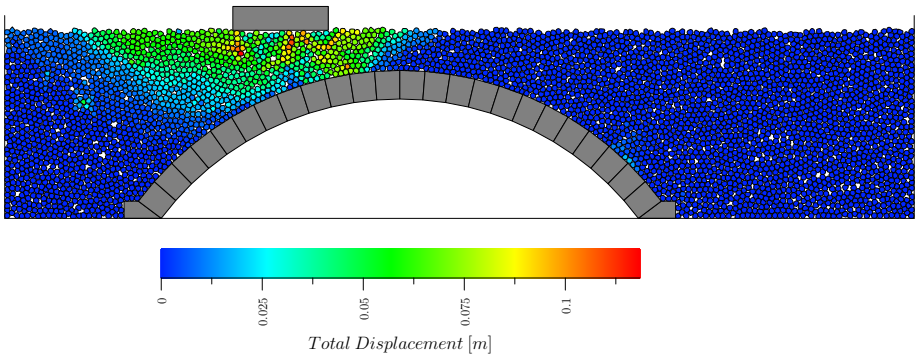

(d)

Figure 5.21.: Full backfilled arch test; local bearing failure in simulations run with different seeds (captured at $x = 0.11$): (a) seed 2; (b) seed 3; (c) seed 4; (d) seed 5

Validation against LimitState:GEO

Similarly to the simplified backfilled arch tests, the example simulation was validated against LimitState:GEO.

The properties of the arch and backfill in the LimitState:GEO model were the same as those in the validation test for the simplified backfilled arch test with dense backfill with the exception of the angle of friction of the backfill which was set to $29°$, the peak shear strength in the biaxial compression test (see Figure 5.6a); the peak strength is used because in a bearing capacity failure, which is expected in this scenario, the full strength of soil will be mobilized. The loading beam had the same geometry as in the Box2D simulation and was modelled with a weightless rigid material type. The soil-beam interface was modelled with the same material as the soil-arch interface i.e. Derived Mohr-Coulomb type with the multiplier on $\tan\phi'$ set to 0.33. The model was solved with the target number of nodes set to 8000 and the baseline nodal spacing on the arch joints and the beam-soil interface set to 0.1. The accuracy settings were judged to be sufficient as the difference in the collapse load between simulations with 8000 and 4000 nodes was below 3%.

The identified failure mechanism, shown in Figure 5.22, is a bearing capacity failure of the loading beam; this agrees with the finding from the Box2D simulations: a local bearing capacity failure of the loading beam precedes the global failure mechanism of the arch-backfill system. The collapse load was 1428 kN which is 8.9% lower than the mean of the Box2D simulations, relatively close considering high sensitivity of bearing capacity problems to the strength of soil and large discrepancy between Box2D simulations caused by the relatively large particle size used.

Unfortunately, LimitState:GEO is a limit analysis software and cannot progress the simulation past the bearing capacity failure thus the load capacity of the arch-backfill system obtained in the Box2D simulation could not be validated with this tool.

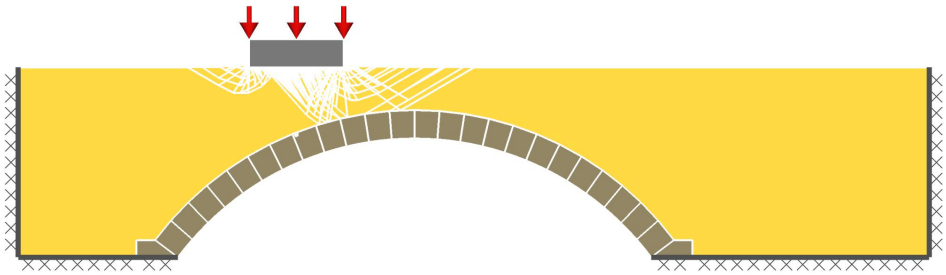

Figure 5.22.: Full backfilled arch test: failure mode in LimitState:GEO

5.4.3. Summary

The full backfilled arch test has been described; the program is an upgrade of the simplified backfilled arch test; it adds direct modelling of live load distribution in the backfill and therefore replicates a typical laboratory test on masonry arch bridges.

Results of an example test with the same system properties as in the simplified backfilled arch tests with dense backfill but with load applied via a loading beam were presented; the

load capacity of the arch-backfill system, as expected, was significantly higher than in the model with the load applied at a point directly to the arch. The failure of the system was preceded by a bearing capacity failure of the loading beam, a finding confirmed by the validation test modelled using the LimitState:GEO software. The bearing capacity of the loading beam in the Box2D simulations was relatively close to the LimitState:GEO validation test which indicates that the ratio of B/d_b of 16.7 might be sufficient for this type of problems (as the mechanics of a bearing capacity problem and a load distribution under a beam problem are essentially the same).

5.5. Discussion

5.5.1. Overview

The biaxial compression test program together with the three programs discussed in this chapter constitute a powerful virtual laboratory for testing of masonry arch bridges with frictional soil.

The biaxial compression test program is a virtual equivalent of the triaxial test, a standard laboratory test used in geotechnics in order to determine the properties of a given soil. It is envisaged that this tool will be used to determine the micro-scale properties of the soil model that will provide the macro-scale behaviour matching this of a backfill of the real bridge under consideration; a database of virtual soil models replicating behaviour of the most common soil types and a guidance on how the behaviour can be fine-tuned would be required if this tool is to be used in an engineering practice.

The bare arch test program was developed primarily to help at the model development stage so new models of arches can be tested and validated before they are used in the tests with backfill; it has runtime of seconds and allows for quick and easy testing of bare masonry arches.

The simplified backfilled arch test program was designed for relatively quick analysis of masonry arches backfilled with frictional soil; the presented simulations, at a reasonable accuracy provided by just 1000 particles in the model, had a runtime of less than one hour on a single CPU core and have a potential to be much faster simply by using the optimal N_i input. The disadvantage of the test is a lack of direct modelling of live load distribution but with the addition of the industry standard uniform and Bousinesq distribution models the program would certainly provide an appealing alternative to the full backfilled arch test.

The full backfilled arch test program is a powerful tool for analysis of masonry arch bridges with frictional backfill which models both the masonry and the backfill directly and replicates a typical laboratory test settings. The program has essentially similar capabilities to a finite element or a conventional DEM simulation but does not require tuning of the input parameters which are instead taken from the biaxial compression test; this gives confidence that the program is able not only to replicate results of a laboratory test but also to reliably predict the behaviour of a bridge which is under assessment. The simulation runtime of several hours in the presented example is likely to be significantly longer if the width of the loading beam is to be more realistic (as finer particles would have to be used) but there is

a large scope to make, both, this test and the Box2D engine much faster; e.g. the former by using the very fine soil particles only in the vicinity of the loading beam and the latter by making the engine multi-threaded.

5.5.2. Accuracy

The accuracy of the bare arch test program was found to be excellent but it was the only test that could be validated so easily. For the other programs, the results were validated by assuming that the macro-scale properties of the backfill determined in the biaxial compression test were the same as in the backfilled arch tests; this hypothesis holds true for all the three independent scenarios tested, i.e. the simplified backfilled arch test with dense soil, the simplified backfilled arch test with loose soil and the full backfilled arch test with dense soil, and therefore it can be concluded that these programs also provide accurate simulation results. It has to be noted, that in the tests presented there was no tuning of the simulation input parameters; the micro-scale properties of the backfill in the biaxial compression test and in the backfilled arch tests were the same and the accuracy settings were determined using a standardized procedure proposed by the author of this study.

5.5.3. Future

The presented results are very promising but clearly more work is required if the developed programs are to be used in an engineering practice. Firstly, realistic soil models have to be developed and ideally a database of those created. Next step would be to validate the developed programs against laboratory test data and finally to improve the simulation speed as the potential gains in this area can be of several orders of magnitude. These issues and other recommendations for further work on Box2D based modelling tools are discussed in more detail in Section 8.1.

6. New facility for testing of soil-filled masonry arch bridges

This chapter describes the development process and features of an innovative masonry arch bridge test facility recently commissioned at the University of Sheffield. The contents of this chapter should prove useful for researchers wishing to develop a similar test facility, i.e. for testing of reasonably large models involving frictional soils, and those who will be using the test rig described in the future.

The test facility described in this chapter was designed to overcome inherent limitations in comparable facilities described in the literature, and came into existence thanks to the hard work of technical staff at the University of Sheffield, supervised by the author, who was in charge of the development process, including the design, procurement, fabrication of parts in the departmental workshop, assembly and testing and fine-tuning of the equipment.

6.1. Design specification

The test facility was developed primarily for conducting static load tests to failure on models of soil-filled masonry arch bridges. The final technical specification was based on the considerations described in this section.

6.1.1. General

The present study is concerned with soil-structure interaction and recording soil kinematics throughout the tests was essential; for this reason, it was decided that the model would not feature spandrel walls and that the backfill would be contained between the transparent walls of the test chamber. The test chamber was to be very stiff in order to provide plane strain conditions. Initially, in order to simplify the development, the backfill material was to be limited to sand only and the models were not to feature sub-base material or surfacing.

6.1.2. Instrumentation

As discussed in Chapter 1, there is a lack of high quality laboratory test data that would allow for thorough validation of more advanced methods of analysis for masonry arch bridges. The finite element method or discrete element method models, including the numerical tools described in Chapter 5, can, and should be validated on the basis of not only the capacity of the arch-backfill system and the displacement of the arch but also the stress-strain behaviour of the backfill. For this reason, it was decided that, apart from the data on load-displacement

behaviour of the arch, the test facility should allow for collection of data on soil kinematics and soil pressures. The requirements with regards to the instrumentation were therefore as follows:

- transducer measuring load applied on the loading beam
- transducer measuring displacement of the loading beam
- three transducers measuring radial deformation of the arch
- two transducers measuring displacement of the abutments
- transducer(s) measuring pressure exerted by the soil on the arch barrel
- high resolution camera to capture soil kinematics

6.1.3. Model size

On one hand, in order to keep the development and running costs low, as well as to assure rapid test turnaround, the bridge model should be small. On the other hand, its size should be large enough to allow for good test-quality control and for reliable measurement of all the quantities listed in Section 6.1.2 during the tests. The test facility described in Callaway (2007), for testing of 0.38m span bridges made of acrylic, which was previously used at the University of Sheffield was considered to be too small; at the time, there were no reasonably priced transducers available on the market that would allow reliable measurement of soil pressures in the model of that size; also fabrication of masonry voussoirs, so the friction at the soil-arch interface could be more realistic than in the acrylic model, was expected to be very problematic. It was therefore decided to build the facility for testing of models of approximately twice the size of those previously tested at the University of Sheffield. Note that, since no attempt of modelling mortar and masonry crushing strength was to be made, and that the backfill was to be purely frictional, the scaling of stresses inside the model was not of primary concern here (see Section 2.3.2 for a short discussion on this).

6.1.4. Automation

The pre-critical state stress-strain behaviour of a frictional soil is determined, to a large extent, by its initial density. In laboratory tests involving sand, it is therefore very important to have a good control over the sample deposition stage, so the density achieved is both uniform across the model and repeatable. This is potentially difficult to achieve with manual sand placement, especially in relatively large models where the procedure might take several hours and involve more than one operator. For this reason it was decided to automate the backfill deposition stage.

6.2. Details

6.2.1. Arch model

Geometry

The work presented here forms a part of the EPSRC research project 'Ultimate and permissible limit state behavior of soil-filled masonry arch bridges'. With regard to the experimental work, the project involved also full-scale tests conducted at the University of Salford using an enhanced version of the test facility described in Smith et al. (2006). It was therefore decided that, in order to make the test results comparable, the arch model in the test facility being developed at Sheffield should be capable of testing scaled down versions of the bridges tested at the University of Salford; considering the desired size of the model discussed in Section 6.1.3, the scale factor was to be 1:4. The geometry of the default test structure was therefore determined to be as follows: segmental arch barrel with 750mm span, 4:1 span to rise ratio and 54mm thick arch barrel. The default width of the arch was set to 198mm, with 1mm clearance between the arch and each of the test chamber walls. Note that, in plane strain tests involving soil, the width of the model must be sufficient to make the influence of the friction at the soil-test chamber interface on the test results negligible. It was therefore envisaged that wider arch models of 398mm and/or 798mm widths would be tested in the future to verify whether the default width was sufficient.

Voussoirs

The default arch barrel consisted of one ring of 24 voussoirs fabricated from solid engineering bricks (Ketley Staffordshire Red Engineering Brick Class A Solid). The number of voussoirs was judged to be sufficient so as to not unduly restrict the failure mechanism (for more information on this issue, see the parametric study NOV presented in Section 5.2.4) and kept the voussoir size large enough to house a pressure sensor.

The cross-section of the voussoirs is shown in Figure 6.1b. The geometry has been chosen in order to maintain a uniform arch joint thickness of 2.0mm across the thickness of the arch barrel. Each voussoir was, first, cut from a brick to a size slightly larger than the design and was then ground to the dimensions required; this technique removed jagged edges on the final product. In order to provide realistic friction at the soil-arch interface, the top face of the voussoirs, forming the extrados in the tests, was formed by the 215x65mm fair face of the brick and was not processed. The tolerance on the width of the voussoirs achieved in the best 24 units out of 42 produced in the workshop was +/- 0.5mm with the average deviation at the bottom and at the top of the voussoir of +0.15mm and -0.04mm respectively. In the voussoirs that were to be used in the tests, a pocket for a pressure sensor was then drilled as shown in Figure 6.1. The typical mass of a voussoir with a sensor pocket was 841g.

The fabrication process for a single voussoir took approximately 1.5 hours; it was therefore important to take good care of the voussoirs so they could be re-used in as many tests as possible.

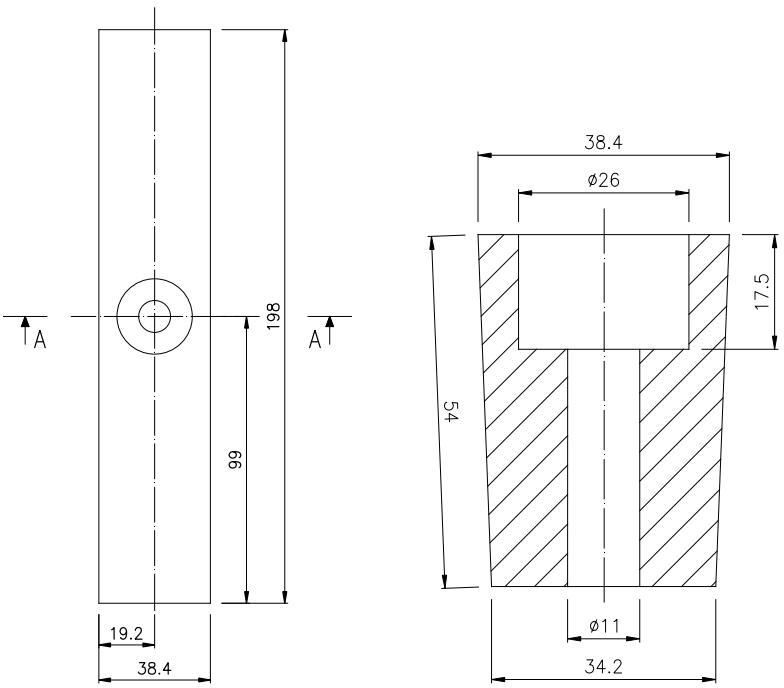

Figure 6.1.: Voussoir: (a) top view; (b) cross-section on A-A

Joints

The joints in all the conducted backfilled tests were made of mixture of Leighton Buzzard sand fraction D and Kaolin clay in 19:1 ratio (by weight). The idea of using sand for joints was inspired by the full-scale tests described by Melbourne and Gilbert (1995) where damp sand was used between the concentric rings of brickwork to simulate their separation. The addition of clay ensures that joints, constructed with a damp material, stay intact after drying out, yet the cementation is weak enough as to have negligible effect on global behaviour. The friction provided by the mix was found to be sufficient to prevent shear and snap-through failure mechanisms of the arch.

The construction of the arch with the clayey sand joints was done in the following steps (see the method statement in Appendix A for a more detailed description):

(i) Build the arch with voussoirs separated by steel shims

(ii) Feed 15g of the clayey sand material into each joint (this filled approximately 40% of the volume of the joints after densification)

(iii) Feed water into each joint

(iv) Densify the material in each joint by tamping

(v) Repeat steps (ii) to (iv) twice in order to finish the joints

(vi) Remove the steel shims

The arch model under construction prior to step (vi) of the procedure is shown in Figure 6.2 (the photograph was taken during the setup for a trial test featuring only one soil pressure

sensor). The shims used in this procedure had nominal thickness of 1.8mm with several of them wrapped with tape in order to achieve the required average thickness of the joints. The shims were laser cut to the specified width of 3.0mm and height of 75mm. The final width of the joints was 192mm (the width of the arch barrel minus the width of the two shims)

Figure 6.2.: Arch construction: arch model prior to step (vi) of the construction procedure

The clayey sand joints have very low compressive strength compared to mortar which, additionally, depends on their density, a property that, to some degree, varied between the joints and between the tests despite significant efforts to keep it uniform. Very low compressive strength of the joints is problematic because it allows the arch to deform more easily and can result in a significant reduction of its load capacity. Unfortunately, the problems with the clayey sand joints were noticed very late in the research programme, after this type of joint had been used in all the initial backfilled arch tests. A series of bare arch tests designed to explore the issue of joints in the model is described in Section 6.3.1.

Abutments

The design of the abutments, shown in Figure 6.3, allows for investigation of the influence of abutment fixity on the behaviour of the model. Each abutment consists of two parts. During a test, the lower part is fixed in place by two steel angles positioned on each side of the part and bolted to the structural elements of the test chamber; the top part of the abutment is either free to slide or fixed to the lower part via two aluminium rods, as shown in Figure 6.3c. The 9.95mm rods are inserted into 10mm aluminium tubes built into each part of the abutment. In order to ensure perfect alignment of the tubes, the top and the bottom part of each abutment were cast together, with the rods inserted.

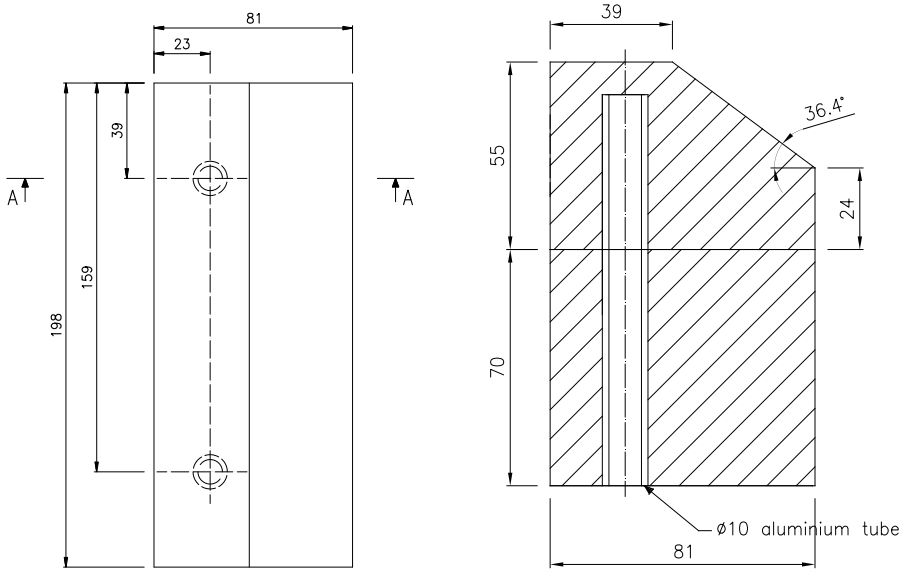

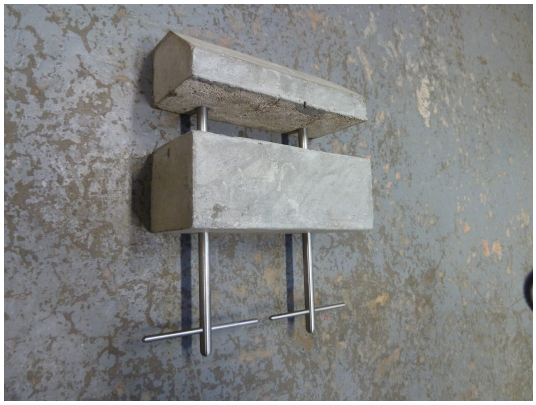

(c)

Figure 6.3.: Abutments: (a) top view; (b) cross-section on A-A; (c) exploded view with rods inserted

Centring

During construction the arch is supported by a centring. The centring, shown in Figure 6.4 in its dropped position, consists of two segmental arches cut from plywood to the required geometry and attached to the plywood base; the arches support 1mm curved aluminium plate with 27 openings for the instrumentation. The centring sits on two M20 threaded rods which are attached to the structural elements of the test chamber; prior to the test, the centring is dropped by means of a screw mechanism.

Figure 6.4.: Centring

6.2.2. Backfill material

As identified in Section 2.4, there is a need for laboratory test data featuring a variety of backfill materials. However, due to constraints in the present study, it was decided that initially the test rig would be developed for tests with sand backfill only. Sand was selected because: (i) it can be deposited by pluviation, a technique that can be automatized relatively easily, and (ii) according to Callaway (2007) it is one of the more popular backfill material types used in real structures.

6.2.3. Test chamber

The test rig is shown in Figure 6.5. In the design, the main concern was the stiffness of the chamber so that approximately plane strain conditions could be maintained throughout the tests; usually satisfying this requirement ensured the design easily passed all the structural strength checks.

The test chamber was designed to contain the full failure mechanism when the arch was positioned as shown in Figure 6.6 and backfilled to a typical height above the crown, and allowing for tests involving 200mm, 400mm and 800mm bridge widths; the default position of the arch, shown in the figure, was chosen with a view to decrease the necessary size of the test chamber (unless the arch is loaded at the center, the volume of deforming soil is larger on the passive side of the arch).

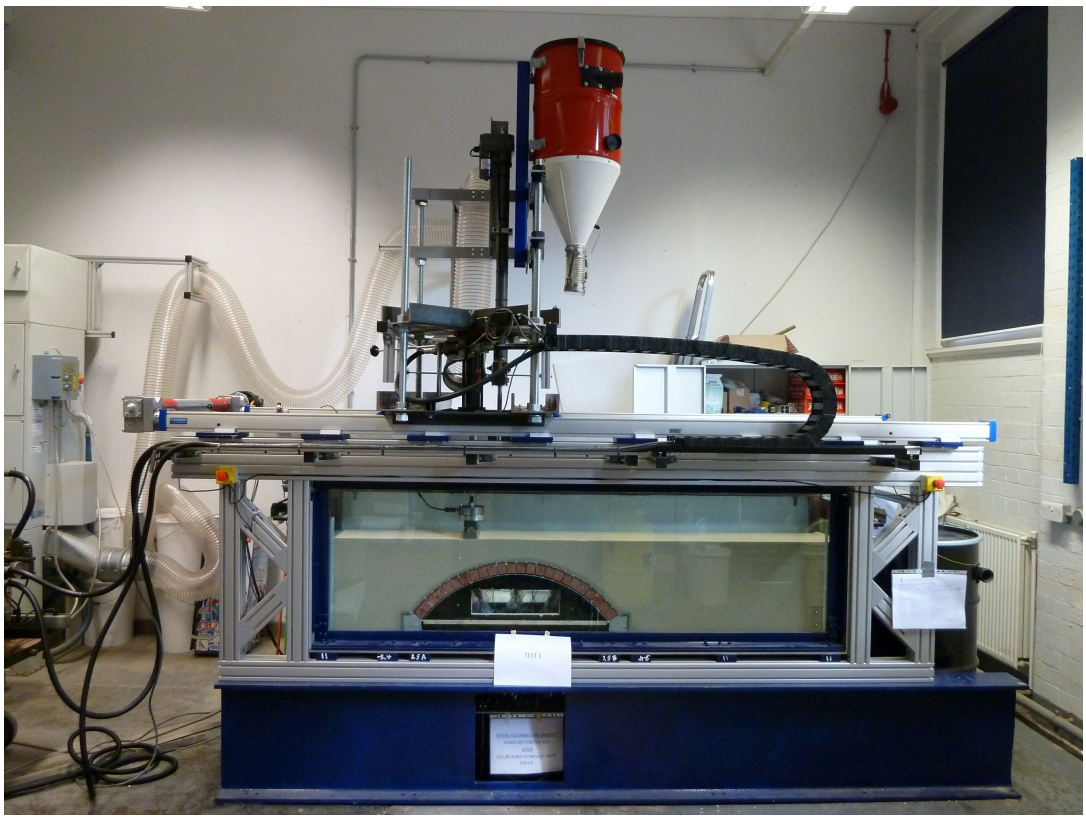

(a)

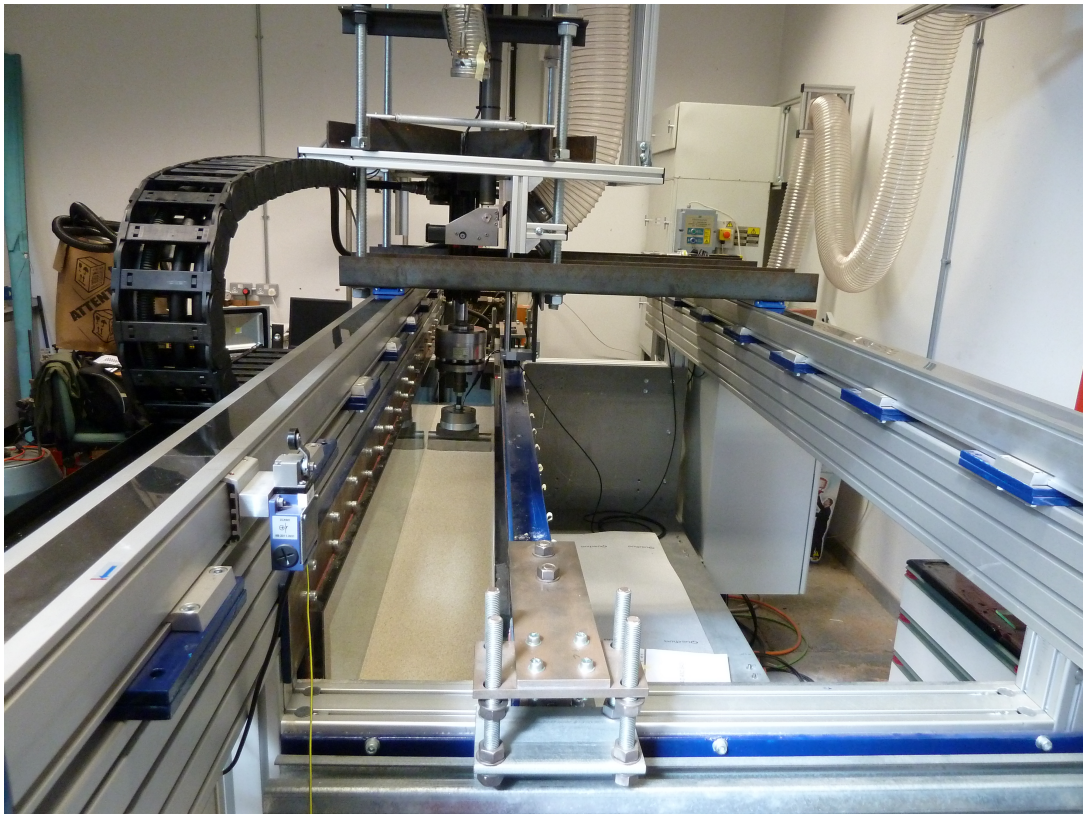

(b)

Figure 6.5.: Test rig: (a) front view; (b) side view

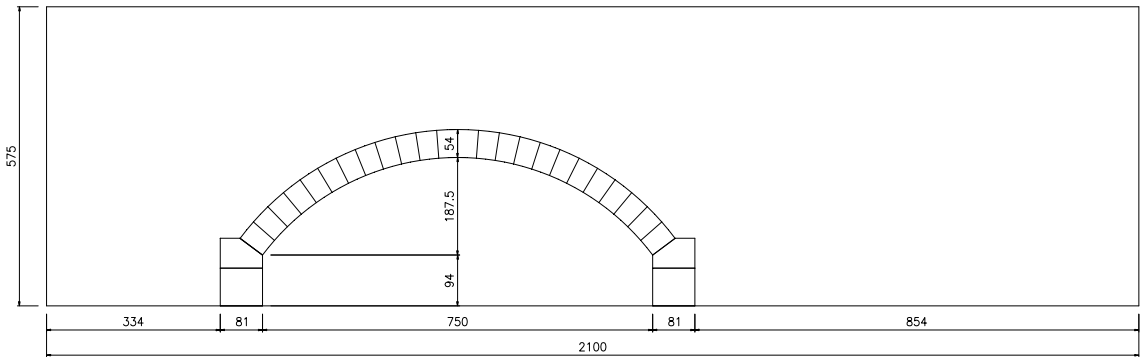

Figure 6.6.: Dimensions of the test chamber

Frame

The main frame is formed using modular heavy section aluminium extrusions. The design drawings of the aluminium frame are given in Appendix B. The parts of the aluminium frame were ordered from AlProfil limited; they were cut and drilled by the manufacturer according to the design specification which allowed assembly time to be reduced to just a few days. The supplier was selected in a tender process involving three bidders. The tender process proved to be very useful as the chosen supplier offered the frame system at approx. two thirds of the cost of the competitors, with a much shorter delivery time and with a wider range of heavy duty connectors. Compared to a traditional steel frame, the cost of the material was higher but the assembly process was much less labour intensive; another advantage of the chosen framing system is that with the T-slots on each side of every aluminium profile, new elements can be attached to the frame very easily, something that saved many days of work in the rig development process.

The side walls and the floor of the test chamber are made of 10mm aluminium plates and the front and the back walls of 19mm annealed glass. The aluminium base plate is supported by five T-sections (custom made with 80x30mm flange and 70x15mm web) and two flat bars (80x30mm) spanning across the width of the frame. The frame sits on top of two steel I-sections UB 457x152 which provides sufficient space for a person to climb under the rig if necessary. A large opening was also cut in the front I-section in order to give easy access to the sensor wiring and the abutment rods during the test preparation process.

Glass walls

The front and the back walls of the test chamber are made of 2096x655mm panes of 19mm annealed glass. Annealed glass was chosen because the alternative, tempered glass, has often slightly curved surface due to asymmetric cooling and contact with flattening rollers during the tempering process (Nielsen, 2009). A curved surface would increase the friction at the glass-soil interface and make it non-uniform across the model, and could cause distortion of images used for the analysis of soil kinematics. Note that, although tempered glass has a much higher structural strength than its annealed counterpart, the stiffness, which was of primary concern here, is typically very similar for both materials.

Both glass panes are supported on all four edges and on the bottom side by a steel

frame. The frames consist of several steel sections bolted together and are not perfectly flat; this means that the glass cannot be supported by the frame directly as it would get damaged during the tests due to stress concentrations. It was therefore decided to bond the glass panes to their supporting frames permanently with an epoxy resin. Note that a soft sealant could not be used as plane strain conditions have to be maintained in the tests. Because of the size and the weight of the elements the bonding procedure took several minutes and it was imperative that the resin had a sufficiently long workable time and could be applied quickly and efficiently; these requirements were satisfied by Thor Helical Remedial Epoxy Resin which, at room temperature, has a workable time of 40min and can be applied with a resin injection gun.

The front glass wall could be fixed in place but the back one had to be movable in order to create working space for construction of the arch and to feature tests involving arch models of differing widths. Since the glass pane together with the frame weighs about 120kg, it cannot be slid back and forth easily. For this reason a special mechanism, visible at the bottom of Figure 6.5b, utilizing sliding gate hardware was constructed. On each side, the top of the frame of the back glass wall is connected to a roller. The rollers sit inside tracks connected to the main frame. During a test the glass wall is fixed to the structural elements of the test chamber; when it has to be moved, it is unbolted and then raised by several millimetres using a screw mechanism so its full weight is supported by the rollers; at this point the wall can be moved back and forth easily and dropped down at the position of choice.

6.2.4. Loading system

The loading system consists of Kelsey 50/36 TestLab servo-hydraulic actuator, LOS series 60 hydraulic power pack and Kelsey K7500 digital servo-controller. The system was readily available in the laboratory and was previously used in the rapid load testing of piles described in Brown (2004). In order to adapt the system for the masonry arch tests, the accumulators were removed and the original 41.4kN load cell was replaced with a more sensitive transducer and a new frame was constructed.

The actuator has a 150mm stroke and is capable of applying load of 41.4kN statically; it has a built-in 150mm linear variable differential transformer (LVDT) and is used with a load cell. The actuator can be operated in displacement or load control mode. The servo-controller allows for a closed-loop control over the actuator and provides excitation and signal conditioning for the LVDT and load cell.

The frame, shown in Figure 6.5, consists of two steel channels bolted to the saddles of the linear motion system (LMS, see Section 6.2.5 for a description of this system), four vertical M30 threaded rods and an X-shaped frame to which the actuator is attached; in order to additionally stiffen the frame and to protect the LMS, the threaded rods are connected at the bottom in the longitudinal direction by steel angles. The X-shaped frame, made of parallel flange channels, was designed to provide good stiffness to weight ratio as the lighter the whole frame the higher the allowable velocity of the LMS. The long threaded rods allow the actuator to be adjusted vertically and are used to attach components of the automatic

sand pourer to the frame.

Note that the longitudinal position of the actuator can be adjusted easily using the LMS. Potentially, this setup allows cyclic tests to be performed where a roller is moved back and forth on the top surface of the backfill, as shown in Figure 6.7. In order to support and guide the hydraulic pipes and electrical cables of the actuator during motion of the LMS, a cable carrier system (IGUS Energy Chain E4.32 series) was added to the test rig; this is a black plastic chain visible in the centre of Figure 6.5a and in the left top part of Figure 6.5b.

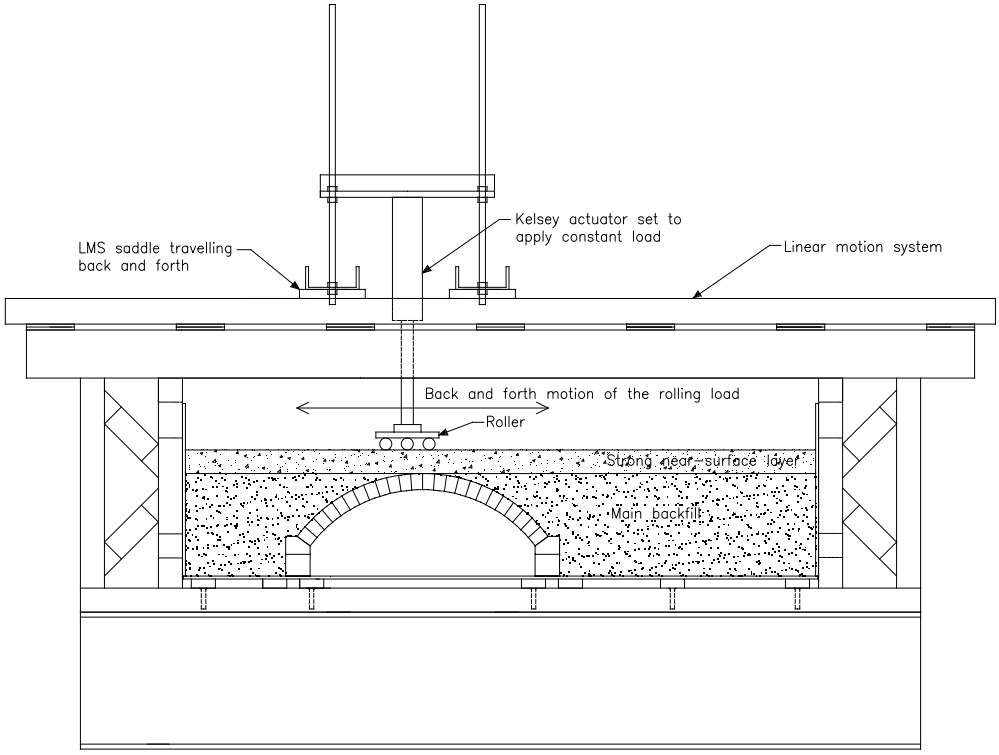

Figure 6.7.: Potential cyclic loading setup

6.2.5. Sand conveyance and pouring system

Overview

The motivation for developing the system described in this section was twofold; first, to ensure that the density of backfill in the tests was always uniform across the model, repeatable and could be controlled and second, to speed up the backfilling process. The technical specifications of the system were therefore as follows:

(i) The sand is to be deposited with an apparatus similar in concept to the multiple sieving pluviation apparatus described in Miura and Toki (1982) but with a rectangular nozzle of a width equal to the width to the model. The position of the apparatus in the vertical and in the longitudinal direction is to be computer controlled and programmable. Following the findings of Miura and Toki (1982), control of the flow rate is to be the primary way to control the density of the backfill

(ii) The sand is to be transported to the pluviaton apparatus by vacuum

(iii) After the tests, the sand is to be removed from the test chamber by vacuum

(iv) At the end of the backfill deposition stage, the top surface of the backfill is to be levelled by vacuum

The budget limits, the large size of the model and its plane strain nature, and the additional requirements compared to the automatic sand pourers developed at other research centres (e.g. see Zhao et al. (2006)) meant that the system had to be designed from scratch to a large extent.

The system in the setup used for backfill deposition is shown in Figure 6.8; the main components as referred to in the figure are as follows:

(1) **Linear motion system (LMS)**

The system provides capability of longitudinal motion of the sand pourer apparatus and the Kelsey actuator. The system was designed for high thrust, payload, precision and stiffness; high speed and acceleration were not of primary concern. In order to ensure a cost effective solution, the system was selected in a tender with three bidders. The chosen system consists of two ball screw driven linear sliders (Thomson Movopart M75) driven by a servo motor connected via two worm gearboxes connected by an intermediate shaft with control provided by a Baldor MotiFlex e100 servo drive.

The linear sliders have physical length of 3200mm and can provide a stroke of 2200mm at a resolution of 0.1mm and a repeatability of 0.05mm; each unit features two saddles and a magnetic strip preventing ingress of debris into the internal mechanism. The linear sliders are supported along the whole length by the main frame of the test rig with each unit clamped to the frame at eight points. The Baldor MotiFlex e100 servo drive has a built in motion controller and features the Mint ActiveX application which allows the system to be computer controlled using a program written in the LabView software.

The system is controlled via a purpose written LabView program; the user can specify the velocity, acceleration and deceleration of the system; the target position can either be specified directly in the LabView program or a sequence of target positions can be read in from a text file.

For safety reasons, the system features two physical limit switches on each side of the test rig and four emergency stop push buttons positioned on each top corner on the test rig.

(2) **Electric actuator**

The actuator allows vertical motion of the pluvation box and the T-shaped suction device (used for levelling of the top surface of the backfill). The Kelsey actuator could not be used for this purpose because its 150mm stroke was not sufficient. An ideal solution would be to replace the Kelsey actuator with an electrical one catering for the needs of both, the loading system and the sand conveyance and pouring system, However, unfortunately the budgetary limitations did not allow for this. Instead, a low

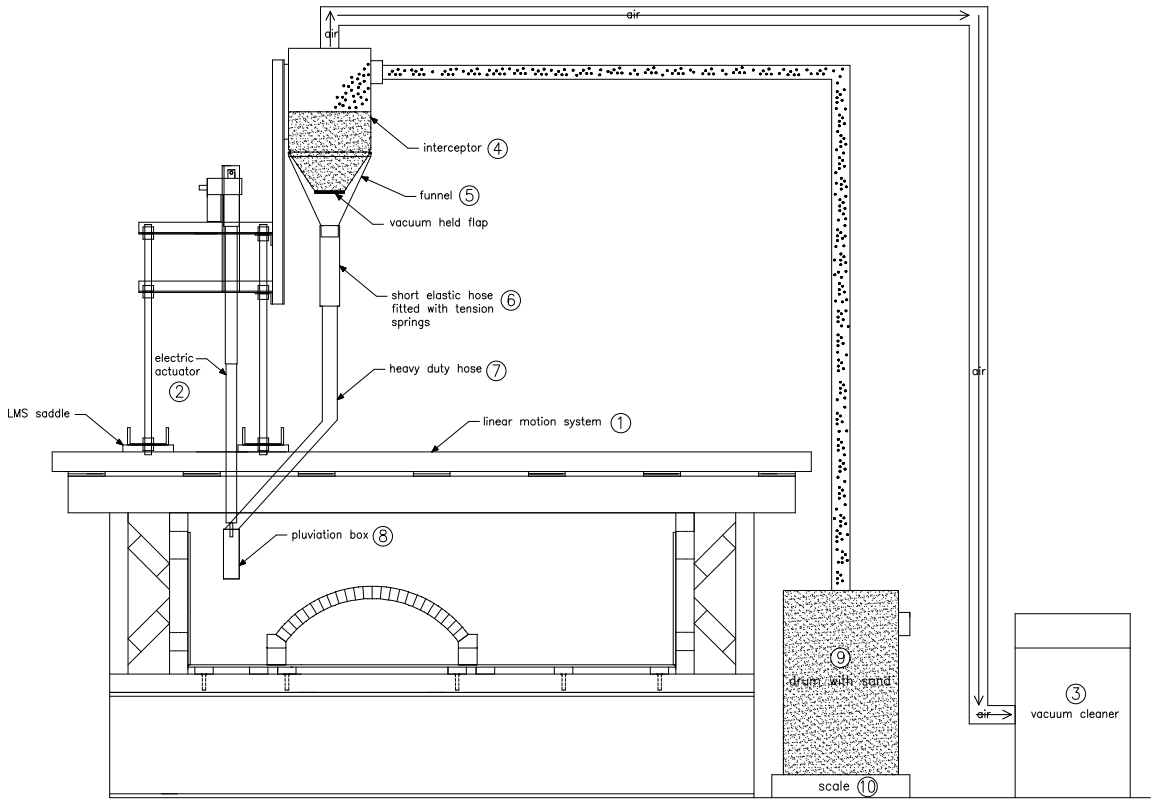

(a)

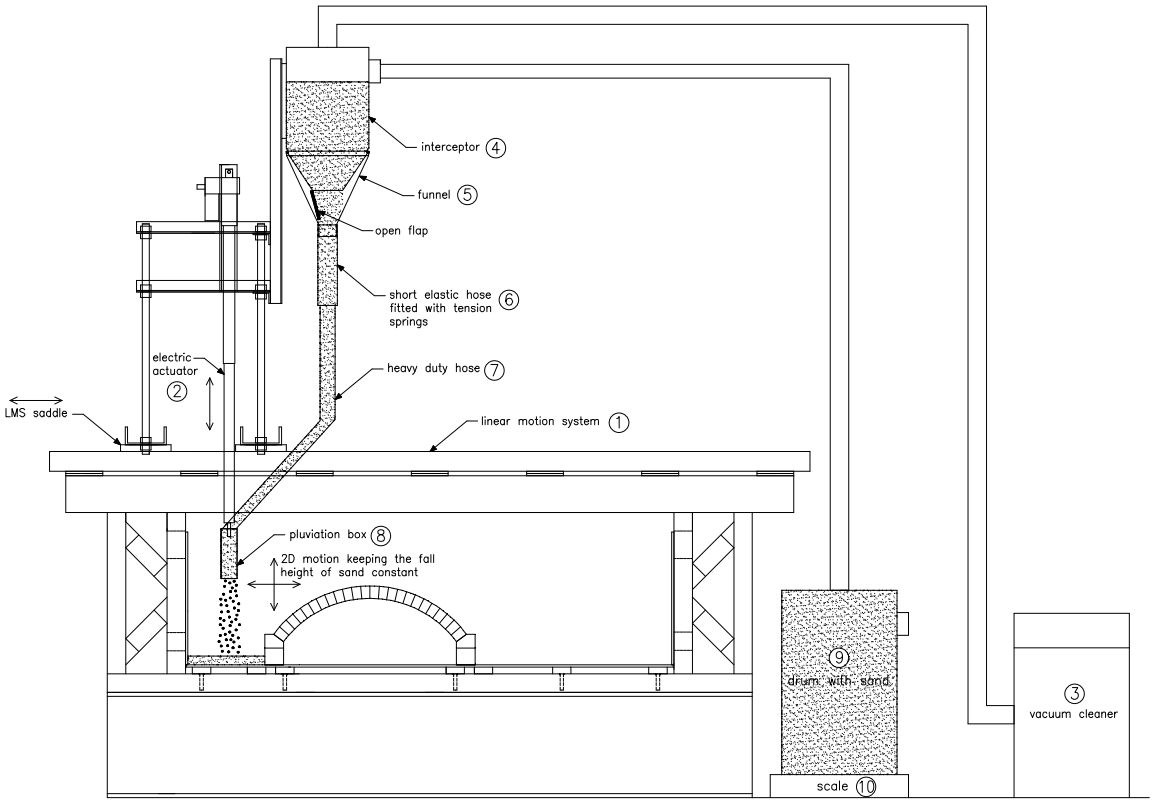

(b)

Figure 6.8.: Sand conveyance and pouring system in the setup used during backfill deposition: (a) first stage; (b) second stage

cost Firgelli Automations 24” Industrial Heavy Duty Linear Actuator was used. The actuator has a stroke of 610mm and a built-in potentiometer for position control; the velocity, acceleration and deceleration of the actuator cannot be controlled but this is not required for the present application.

The control of the actuator was designed so together with the LMS it forms a two-dimensional motion system; it is computer controlled via the same LabView program as used for the control of the LMS; similarly to the LMS, the position of the actuator can either be specified directly in the LabView program or a sequence of target positions can be read from a text file (the same file as used to control the LMS).

The actuator is connected directly to the pluviation box; the end point of the actuator rotates slowly as it extends and this was not acceptable as it would drive the pluvation box into the glass walls and potentially damage them. In order to rectify this, the end point of the actuator is attached to a linear bearing block travelling along a circular linear shaft attached to the frame of the Kelsey actuator.

(3) **Vacuum cleaner**

The vacuum cleaner was required to: (i) be powerful enough to transport sand from a container standing on the ground to an interceptor located over 2m above the container and up to 3m away in the horizontal direction and (ii) to safely remove silica dust, a health hazard, from the sand during the transportation process. These requirements were satisfied by the chosen vacuum cleaner, a Numatic HZDQ750s, which has been specifically designed to remove dust that could constitute a health hazard and features a 2400 watt motor.

(4) **Interceptor**

The WMD interceptor module was supplied by Numatic; it features an outlet in the top lid, an inlet on the side and a thick rubber flap at the bottom. In the setup used during the sand deposition process, the outlet is connected, via a pipe, to the vacuum cleaner and the inlet has the sand feed hose attached. When the vacuum is on, the flap is vacuum held and the interceptor can hold approximately 25kg of sand inside; once the vacuum is switched off, the flap opens and the sand is released to the pluvation box via the pipes.

(5) **Funnel**

The funnel connects the interceptor with the short elastic hose. It was custom made from a 3mm thick polypropylene sheet.

(6) **Short elastic hose**

The hose connecting the interceptor with the pluviation box has to accommodate over 400mm vertical displacement of the pluvation box without restricting the flow of sand; this was not possible with a regular vacuum hose. Instead the hose connecting the interceptor with the pluviation box consist of two parts; a short part made of an elastic

clear PVC hose fitted with three tension springs which provides most of the displacement capability required and a longer part made of a heavy duty vacuum hose. The tension springs keep the elastic hose fully retracted without sideways bending when the pluvation box is in its high position.

(7) **Heavy duty hose**

A 76mm vacuum hose is attached permanently to the pluviation box. In order to guide the hose during extension/contraction of the electric actuator a roller attached to the frame of the Kelsey actuator was added to the system.

(8) **Pluviation box**

A cross section of the pluviation box in the longitudinal direction of the test rig is shown in Figure 6.9. The sand is fed to the box by the heavy duty hose; the particles then fall through the openings in the replaceable aluminium plate and through the two sheets of woven wire mesh before they land in the test chamber. The flow rate of sand, and therefore its deposition density, can be controlled by using replaceable aluminium plates with different opening spacings and diameters. The two sheets of woven wire mesh spread the sand particles evenly across the plan of the box and the plastic curtains prevent the sand particles from landing outside the test chamber when the box is in its highest position.

The sand type used in the masonry arch tests with backfill was Leighton Buzzard sand Fraction B with particles of size of 0.6-1.18mm. The minimum diameter of the openings in the replaceable aluminium plate providing steady flow rate without blockage of this material is 6mm (5mm also provides a steady flow rate but might get block very occasionally) and the minimum spacing of the openings allowing for even distribution of sand particles across the plan of the box after they fall through the sieves is 28mm.

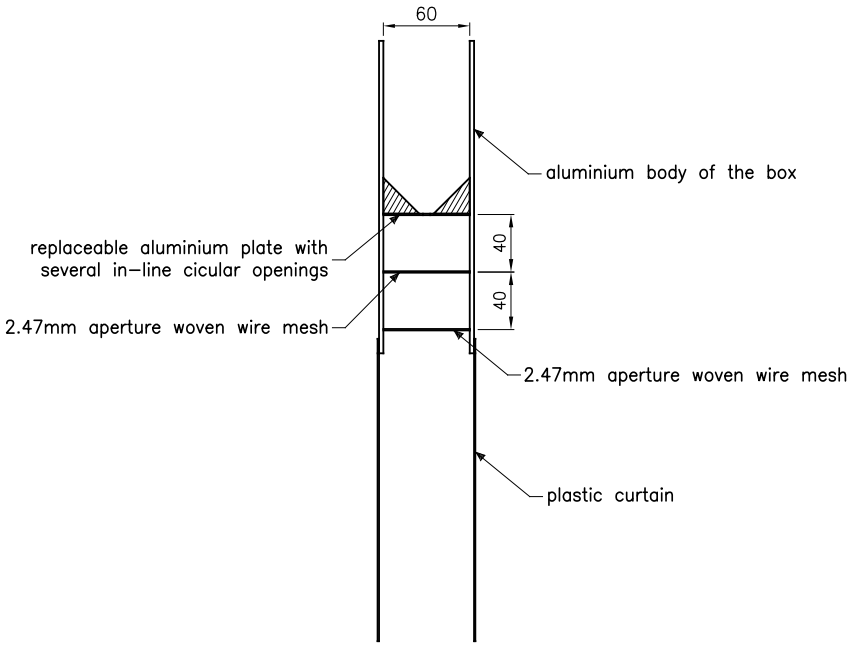

Figure 6.9.: Cross section of the pluviation box

(9) **Drum**

A 205 litre airtight steel drum with removable lid. In order to transport sand directly from the test chamber to the drum after the tests, the lid was fitted with an outlet and the side of the drum with an inlet; during the sand removal procedure, the outlet is connected to the vacuum and the inlet has the sand feed hose attached.

(10) **Scale**

A 300kg electronic floor scale (Adam Equipment GFK 300) with accuracy of 40g. The scale, measuring the weight of the drum with the sand backfill inside, is used to control the amount of sand transported to the interceptor and to calculate the mass of sand inside the test chamber.

(11) **Dust extraction system (not shown in Figure 6.8)**

The sand type used in the tests contains silica dust, a respiratory health hazard, which is released to air when the sand is being pluviated. Part of the dust is removed from the material by the Numatic HZDQ750s vacuum cleaner but an additional safety measure was required. For this reason an industrial dust extractor system was installed in the laboratory. The dust extractor unit was fitted with a 160mm flexible PVC hose; the end point of the hose was attached to the frame of the Kelsey actuator so it travels together with the LMS and is always in the vicinity of the pluviation box.

(12) **T-shaped suction device (not shown in Figure 6.8)**

The suction device, shown in Figure 6.10, is used to level the top surface of the backfill at the end of the backfill deposition procedure. The device is attached to the electric actuator in place of the pluviation box so its height and longitudinal position can be computer controlled. The top of the device is connected to the inlet of the drum via a hose. At the bottom of the device, along its whole width of 196mm, a groove was cut through which redundant sand particles are sucked in and transported back to the the drum.

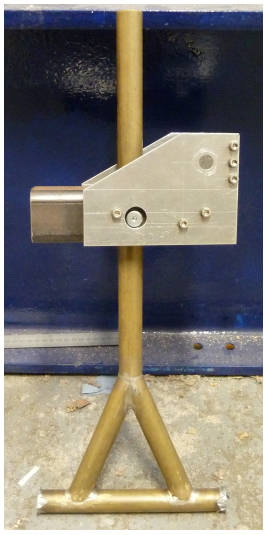

Figure 6.10.: T-shaped suction device

Usage

The arch backfilling procedure using the sand conveyance and pouring system involves the following steps:

(i) Select the replaceable aluminium plate for the pluviation box with the diameter of the openings providing the required backfill density. It is envisaged that this decision will be based on a parametric study that would determine the flow rate and the backfill density at a given drop height for various diameters of the openings.

(ii) Determine the velocity of the LMS that will provide the required thickness of sand layer deposited in one pass of the LMS for the chosen replaceable aluminium plate.

(iii) Prepare the text input file with the required sequence of LMS and electric actuator movements. The example backfilling plan, used in the backfilled masonry arch tests performed to date is shown in Figure 6.11 (20mm thick sand layers were assumed).

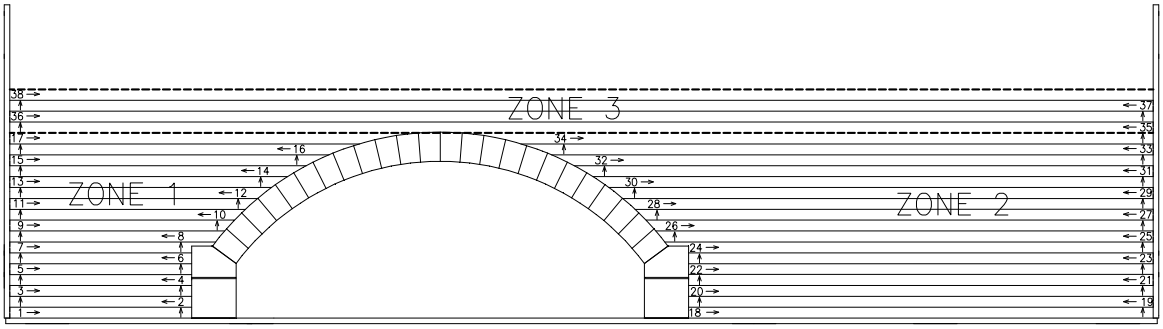

Figure 6.11.: Backfilling plan used in the tests conducted to date

(iv) Repeat stages one and two of the backfilling process, shown in Figures 6.8a and 6.8b respectively, until the test chamber is filled to the required level.

(v) Change the setup of the sand conveyance and pouring system for levelling, and level the top surface of the backfill with the T-shaped suction device.

6.2.6. Instrumentation

Displacement of the loading beam

The displacement of the loading beam is measured by the 150mm LVDT incorporated into the Kelsey actuator. The LVDT was calibrated using slip gauges; the same signal excitation, conditioning and logging devices as in the masonry arch tests were used during the calibration procedure.

Load

The load applied on the arch is measured by a $\pm$2.5kN tension/compression universal load cell (RDP RLU00250). In the default setup the load cell is connected to the Kelsey servo-controller which provides the signal excitation and conditioning required. The load cell was

calibrated with a Budenberg dead weight tester; the same signal excitation, conditioning and logging devices as in the masonry arch tests were used during the calibration procedure.

Arch displacement

The displacement of the arch barrel and the abutments is measured by five 15mm stroke LVDTs with spring return (RDP DCTH 300AG) positioned as shown in Figure 6.12a. A stand, shown in Figure 6.12b, currently bolted to the floor of the test chamber, was fabricated in order to allow for accurate positioning of the LVDTs.

The LVDTs were calibrated with an LVDT calibration rig featuring 50mm Mitutoyo digital micrometer head; the same signal excitation, conditioning and logging devices as in the masonry arch tests were used during the calibration procedure.

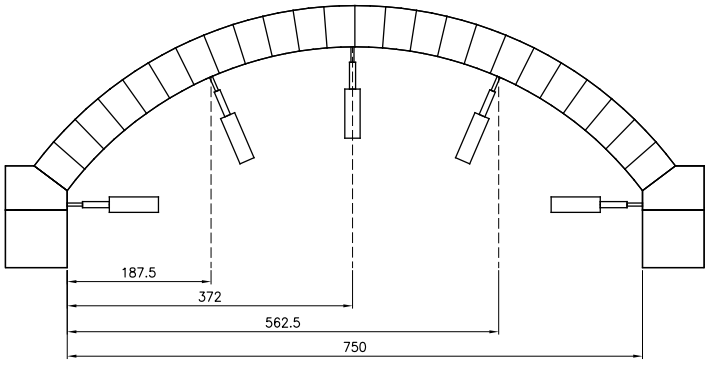

(a)

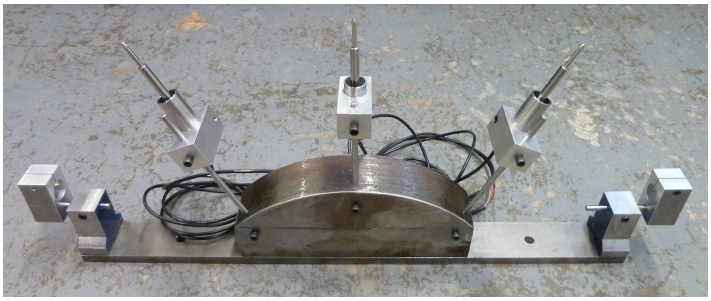

(b)

Figure 6.12.: Arch displacement: (a) layout of the LVDTs monitoring the arch; (b) LVDT stand

Soil pressure at the soil-arch interface

The pressure exerted by the backfill on the arch barrel is measured by the low cost ($<£50$) ceramic pressure sensors PC18-2G incorporated into each voussoir, as shown in Figure 6.13; the setup allows for easy removal of the sensors from the voussoirs when they have to be replaced or calibrated. The sensors have a 0-2 bar range and a 15mm diameter sensing membrane which, for the Leighton Buzzard sand fraction B used in the tests, satisfies the recommendation by Weiler and Kulhawy (1982) of $d/d_{50} > 10$ where d is diameter of the diaphragm and d_{50} is the median grain size of the soil used.

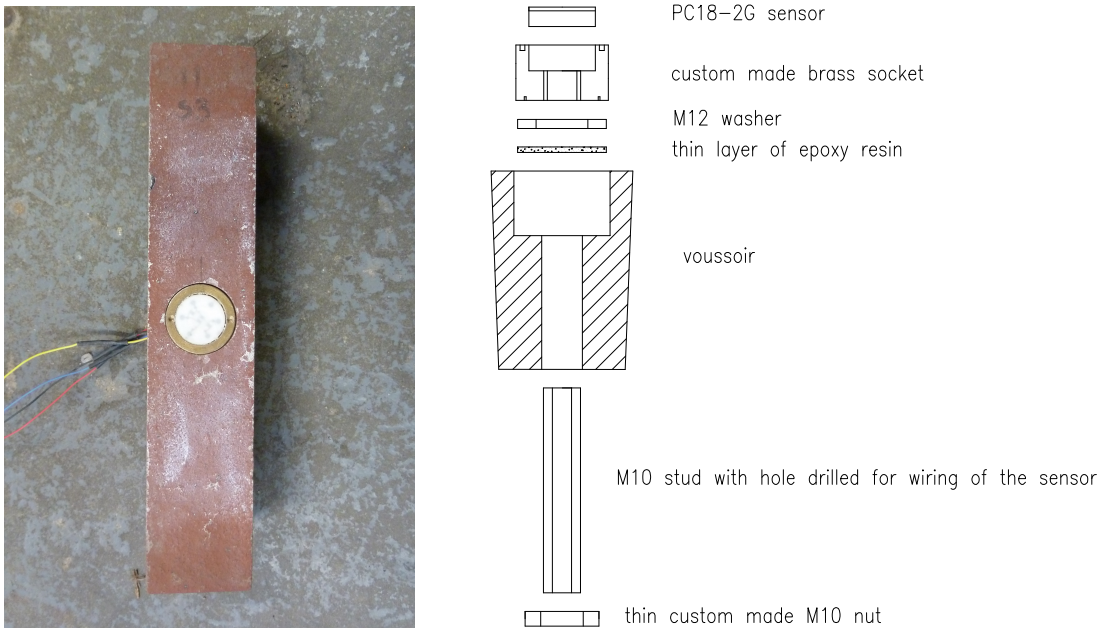

Figure 6.13.: Fixing of the soil pressure sensors: (a) top view; (b) exploded view of the cross section

It has to be noted that pressure measurement in a granular media is not a trivial task; for background reading see e.g. Weiler and Kulhawy (1982), Labuz and Theroux (2005) and Talesnick (2005). The PC18-2G is a diaphragm type pressure sensor; it deflects under the load and the magnitude of this deflection is effectively a measurement of the total load acting on the sensor. In granular media, such as sand, the deflection of the diaphragm relative to the rigid encasing causes soil particles to arch over the sensor; as a result the sensor will tend to under-register soil pressure. In order to account for the effect of soil arching, the sensors have to be calibrated in the soil of the same properties as in the main tests; an additional calibration in a fluid allows estimation of the scale of the under-registration and to evaluate the overall performance of the sensor.

The PC18-2G sensor was calibrated in a triaxial cell in water and in the Leighton Buzzard sand fraction C. Calibration in water was conducted in a triaxial cell with the base plate modified in order to house the brass socket with the sensor. The sensor was excited with 4V DC; the readings were taken with a digital voltmeter with resolution of 0.1mV and the pressure setting system had an accuracy of $\pm$0.3kPa. The calibration in the sand was conducted with the same apparatus, signal excitation and signal measuring device; the sand sample, compacted to an approximate unit weight of 16.5kN/m^3, had a diameter of 100mm and a height of 20mm. The sample was contained within a silicone sleeve and the load was applied by the means of confining pressure in the triaxial cell (i.e. the deviatoric stress was zero throughout the test). The results of two calibration tests in sand, showing part of the first loading-unloading cycle, and the calibration in water averaged over three repetitions, are shown in Figure 6.14a. The sensor readings have very good repeatability in water with average fluid calibration factor c_f of 0.00875 mV/V/kPa (output of the sensor in mV per 1V of excitation per 1kPa of applied pressure) and relatively good repeatability in sand with an

average calibration factor c_s of 0.00444 mV/V/kPa + 0.225 mV/V. In the tests with sand, the sensitivity of the sensor gradually decreases as the applied pressure is increased; this is most likely due to the arching effect becoming more pronounced as the diaphragm of the sensor deflects more at higher pressure levels; the non-zero output of the sensor at 0kPa in the sand test 1 is most likely a result of stresses being locked-in during the sample preparation stage. As shown in Figures 6.14c and 6.14d, in both tests with sand the sensor readings are significantly different between the loading and unloading stages of a loading-unloading cycle and the readings during the loading stage might differ between the first and second loading-unloading cycle.

In general, as shown in Figure 6.14b, at low stress levels the arching effect is negligible and calibration factors derived from calibration in water would provide a reasonable accuracy in tests in sand; at higher stress levels calibration factors derived from calibration tests involving sand have to be used. The hysteretic behaviour is not particularly problematic in a monotonic masonry arch test but could affect the results in a potential cyclic test (although the hysteretic effects are likely to be much smaller if the sensor is subjected only to low pressures).

Note that the sand type used in the calibration process discussed here has a slightly smaller particle size than that used in the main tests (originally it was envisaged that the sensors in the arch tests would be covered by a thin layer of a finer material) and a lower density. Also the signal excitation, conditioning and logging devices used were not the same; this means that the results presented here are only indicative of the behaviour of the sensors in the main tests.

Calibrating sensors in a triaxial cell apparatus is a relatively time consuming process and a special calibration device, shown in Figure 6.15, was constructed to allow calibration of nine sensors at a time. All the sensors were calibrated with this device in water, using the same signal excitation, conditioning and logging devices as in the masonry arch tests. The calibration device was designed to allow for calibration in both sand and water but the full details of the sand setup were not resolved (an additional collar and a latex membrane have to be added and the device will have the same functionality as the calibration chamber described in Talesnick (2005)).

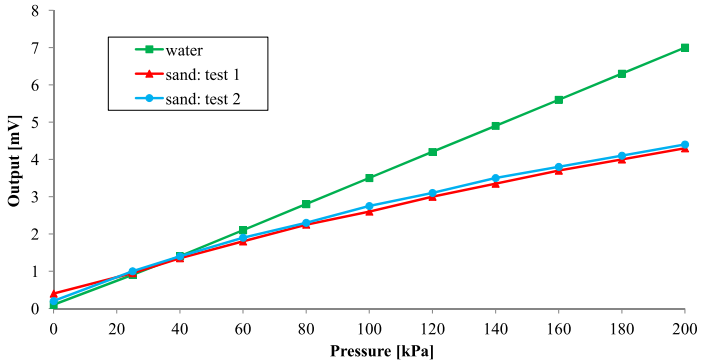

(a)

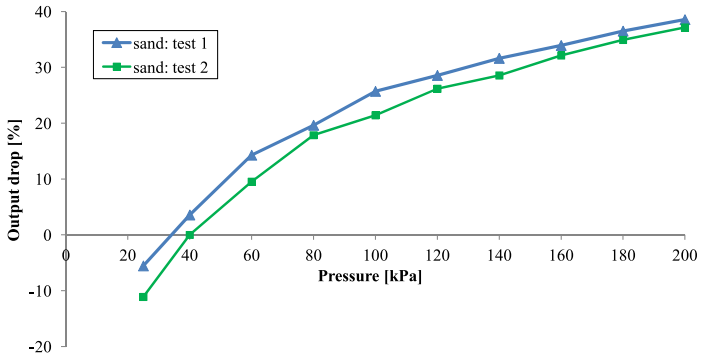

(b)

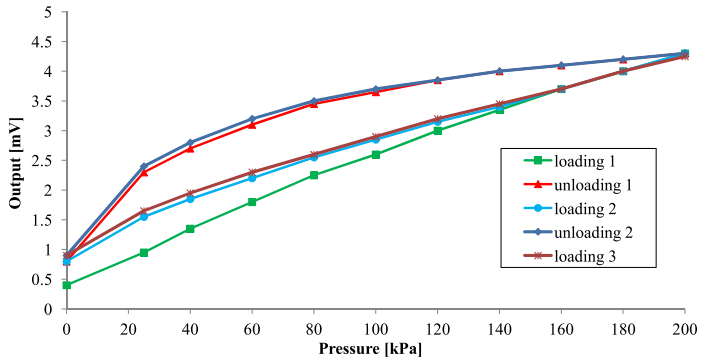

(c)

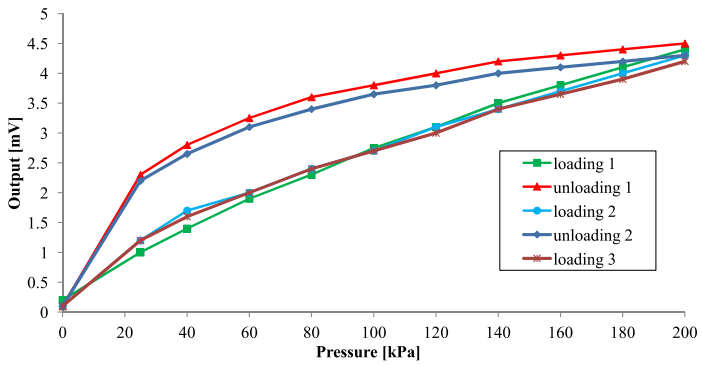

(d)

Figure 6.14.: Calibration of the pressure sensor in a triaxial cell apparatus: (a) loading part of the first load/unload cycle; (b) output drop in the sand compared to water (loading part of the first load/unload cycle); (c) sand: test 1; (d) sand: test 2

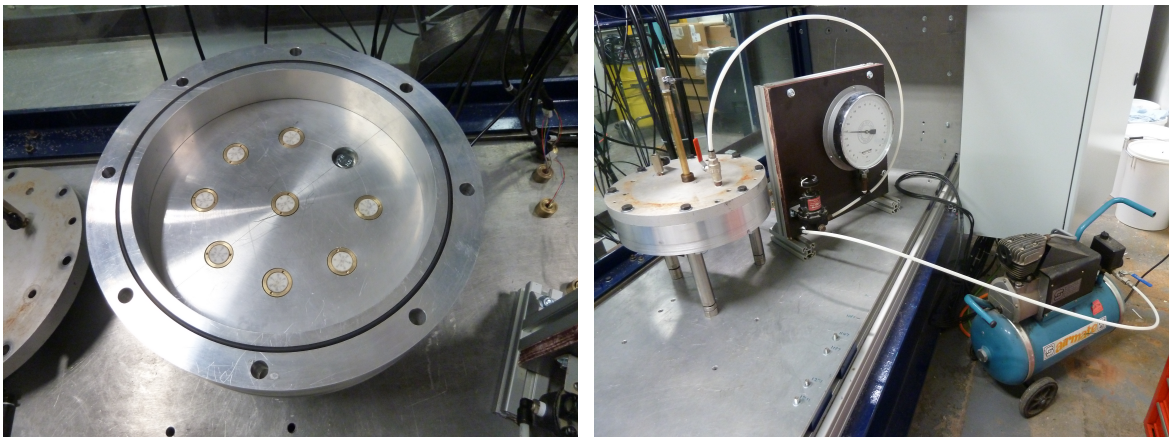

(a) (b)

Figure 6.15.: Pressure sensor calibration device: (a) calibration chamber; (b) full setup of the calibration system

Soil kinematics

Soil kinematics is derived by the means of particle image velocimetry (PIV) (White et al., 2003); the method allows creation of a vector map of displacements of patches of soil between a pair, or a series, of digital images.

Soil deformations in the initial tests were captured using a Canon EOS 5D Mark II camera equipped with a fixed focal length lens (Canon EF 50mm f1.8 II); the camera allows images to be taken at a resolution of 21.1 megapixels. During the tests the camera is attached to a heavy stand, made of welded steel sections and featuring a Manfrotto 338 levelling base and a quick release system. The shutter is controlled remotely using a computer, with the trigger signal sent by a LabView program (the LabView program is also used to log sensor data and thus the images can be easily cross-referenced with the instrumentation output).

When using PIV, it is very important that the lighting conditions are good and as constant as possible throughout the tests, with no reflections appearing in the images. In order to provide these conditions, the laboratory windows were fitted with blinds and the tests conducted with light provided by two LED floodlights positioned at sides of the test rig (heat produced by halogen type floodlights, which were used initially, can potentially affect sensor readings and would also prove very problematic in tests involving clay where moisture content is of major importance to the soil behaviour).

In order to extract from a PIV analysis not only the patterns of soil movement but also the physical magnitudes of the soil deformations, several markers positioned across the model with known relative positions are required; although not of primary interest in the study presented here, three sheets with a total of 17 markers were attached to the front glass wall, from the inside so they would be on the same plane as soil captured on the images, permitting quantitative data on soil deformations to be derived from the tests if required in the future.

Temperature

In order to log ambient and model temperatures, the test rig features five LM135-type temperature sensors. The temperature is not of major importance when undertaking tests involving dry sand but it was envisaged that in the future a series of tests with clay backfill might be conducted; in a clay, a variation in temperature between the tests and across the model might affect the distribution of moisture and therefore mechanical properties of the material.

Data acquisition system

Data acquisition is performed by two National Instruments DAQ modules (NI USB-6218 and NI USB -6008). The process is computer controlled via a LabView program; the average signal from each sensor is logged once a second into a text file.

6.2.7. Friction between the glass walls and the sand mass

In order to maintain plane strain condition in the tests, there should be no friction between the glass walls and the sand mass. In the test facility described here the two methods commonly used in geotechnics to actively reduce friction at the soil-wall interface, namely (i) silicone grease and a thin layer of latex sheet (Tatsuoka and Haibara (1985), Fang et al. (2004)) and (ii) multiple layers of thin plastic sheets (Fang et al., 2004) could not be used; the former is counterproductive at very low normal stress levels and the latter is not suitable for models with non-uniform soil displacements. However, the coefficient of friction of a glass-sand interface is naturally low and providing the model has sufficient width, the testing conditions should be close to plane strain.

The coefficient of friction between annealed glass and Leighton Buzzard sand fraction B was determined experimentally by the means of a shear box apparatus. Three tests with a 60x60mm sand sample slid on a 99x99mm annealed plate were conducted; in each test the coefficient of friction was determined for 42, 82 and 165 kPa normal stress levels. The sand samples had an initial mean unit weight of 14.4kN/m^3 and were slid by the apparatus at a rate of 0.24mm/min; the influence of these two parameters on the results was not investigated as according to Fang et al. (2004) it is negligible.

The mean coefficient of friction determined in the tests was 0.12, which is marginally higher than he results reported in Tatsuoka and Haibara (1985) for Toyoura sand and PYREX glass. The magnitude of variation in the results between the three normal stress levels was relatively low and appeared to be random in character; the coefficient of variation on all the results was 13.8%.

6.3. Testing

6.3.1. Bare arch tests

Test setup

The primary initial focus of the test rig development was on ensuring the automated backfilling process functioned effectively, and produced uniform backfill properties. However, following tests on a number of backfilled arch bridges repeatability issues (significant variation in the load-displacement behaviour of the arch, including the collapse load) not related to the backfill became evident. Consequently bare arch tests were conducted to investigate this issue further. In these tests the load was applied at the quarter span, in a displacement control mode at the rate of 0.5mm/min, via the loading saddle shown in Figure 6.16b; the test setup is shown in Figure 6.16a. In total, three tests on a bare arch with clayey sand joints and one test on a bare arch with mortar joints were conducted.

The arches with clayey sand joints were constructed according to the procedure described in Section 6.2.1.

In the test on arch with mortar joints, the dry mortar mix consisted of five parts of Leigthon Buzzard sand fraction D to one part of Lafarge rapid hardening cement mixed together; the cement was Portland cement based with addition of calcium aluminate to provide rapid setting and hardening properties. According to the specification, in normal conditions, after 1 day of setting time the mortar should have compressive strength of 10 to 19N/mm^2. The construction sequence was as follows:

(i) Treat sides of each voussoir with a release agent. This was required to prevent a strong bond forming between the voussoirs and the joints

(ii) Build the arch with voussoirs separated by steel shims

(iii) Feed dry mortar mix into each joint to fill approximately 30% of the volume of the joint after densification

(iii) Feed water into each joint; approximately 1ml of water per 1g of dry mix was required to moisten all the material; the water to cement ratio was therefore twice of the values typically used in the construction industry

(iv) Densify the material in each joint by tamping

(v) Repeat the steps (ii) to (iv) twice in order to finish the joints

(vi) Remove the steel shims

The arch with mortar joints was tested 70 hours after construction. Inspection of the joints after the test revealed that the material was slightly stronger than the clayey sand mix but significantly weaker that what might be expected of such a mortar; this can be attributed to the comparatively large quantity of water used to moisten the material, coupled with absorption of the release agent, used to treat the voussoirs, into the joints.

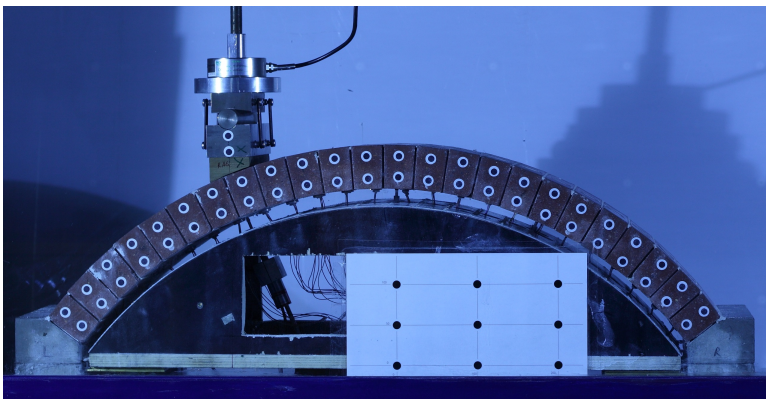

(a)

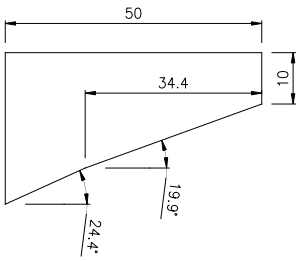

(b)

Figure 6.16.: Bare arch tests: (a) test setup; (b) wooden saddle

Results

All four tested arches failed by reduction to a four hinge mechanism; the load-displacement curves and the location of plastic hinges are given in Figures 6.17a and 6.18 respectively. It is evident that the variation in load capacity between the nominally identical arches with clayey sand joints is very large, with the arch in test 1 failing at 93N and the arches in tests 2 and 3 failing at 143N. The location of the third plastic hinge from the left is different in all the tests. The arch with mortar joints had load capacity of 169N, higher than any of the arches with the clayey sand joints but still significantly lower than the capacity of a rigid body arch of this geometry (computed to be approximately 240N). The low capacity of the arches in all the tests can be attributed to the very low compressive strength of the joints. At hinges, where the compressive force is transmitted through only a small portion of the joint, local crushing failure occurs and the thickness of the arch barrel is effectively reduced. The effect of the very low compressive strength of the joints is similar to the effect of mortar loss, a defect common in real masonry arch bridges.

Numerical parametric study

In order to investigate the influence of the crushing strength of joints on the capacity of the bare arches, a parametric study was carried out using the LimitState:GEO software. The LimitState:GEO model had the same geometry as the physical prototype arch, though its height and length were both increased by a factor of 10 to avoid encountering tolerance problems due to the small size of the model (since LimitState:GEO models are two-dimensional, the width of the numerical model was effectively equal to 1m which is approximately 5 times as large as the width of the prototype arch; the scaling factors on load and stress were therefore equal to $10 \times 10 \times 5 = 500$ and 10 respectively). The voussoirs were modelled using a rigid material type with the unit weight set to 21.48kN/m^3, the same as the average unit weight of the prototype voussoirs with the pressure sensors inserted and the clayey sand joints taken into account. The masonry arch joints were modelled with a mixed material consisting of a cutoff type material with limiting tensile stress set to 0 and the limiting compressive stress taken as the parameter under investigation. A Mohr-Coulomb material type

with angle of friction set to a high value of 45° was also used in order to prevent sliding of the voussoirs, which did not occur in the laboratory tests. The loading beam was modelled with a rigid weightless material. The model was solved with the target number of nodes set to 2000 and the baseline nodal spacing on the arch joints set as 0.1. The accuracy settings were judged to be sufficient as the difference in the collapse load between simulations with 2000 and 1000 nodes was below 1%.

The variation of the collapse load with joint compressive strength within the range of 0.075N/mm^2 to 5N/mm^2 is shown in Figure 6.17b (the values of the stress and collapse load from the LimitState:GEO simulations were scaled down, using factors of 1/10 and 1/500 respectively, and are directly applicable to the prototype arch). The influence of compressive strength of joints on the load capacity of the arch increases with the decrease in their strength in an exponential manner; at about 0.08N/mm^2 where the load capacity of the model matches those obtained in the laboratory tests on arches with clayey sand joints, a very small further drop in the strength of the joints leads to a very significant drop in the capacity of the arch; this could explain the large difference in the collapse load between the test 1 and tests 2 and 3 with clayey sand joints. It has to be noted that this issue is relevant to real structures; for example in the full-scale arch test described in Wang et al. (2011) the structure was four times larger than the model considered here and had joints made of mortar of compressive strength of 1.9N/mm^2; assuming scaling factor on stress of $1/n$, this is equivalent to the compressive strength of joints in the LimitState:GEO model of 0.475 N/mm^2 and at this value the strength of joints would decrease the load capacity of the arch from the theoretical value for rigid body voussoirs by about 10% (although this probably somewhat overstates the actual reduction in capacity as the strength of the composite masonry material (i.e. masonry units plus mortar) is usually greater than the strength of the mortar alone, due to lateral confinement of the latter within the joints).

Discussion

In the backfilled arch tests, at least in the initial stage of the research, the influence of compressive strength of joints on the results is undesirable; the clayey sand joints are clearly not suitable for the models as their very low and variable strength would be difficult to account for. Ideally the joints would have a high compressive strength so that any minor variation would have negligible influence on the results; the mortar joints constructed using the procedure described in this section do not fulfill this requirement either. The best solution may be to either cast all the voussoirs in one form from concrete, so there is no need to construct the joints at all, and the density of voussoirs and their frictional properties are still realistic, or build the arch with mortar joints but constructed in a traditional manner; the latter would add curing time and might even require employment of a professional bricklayer.

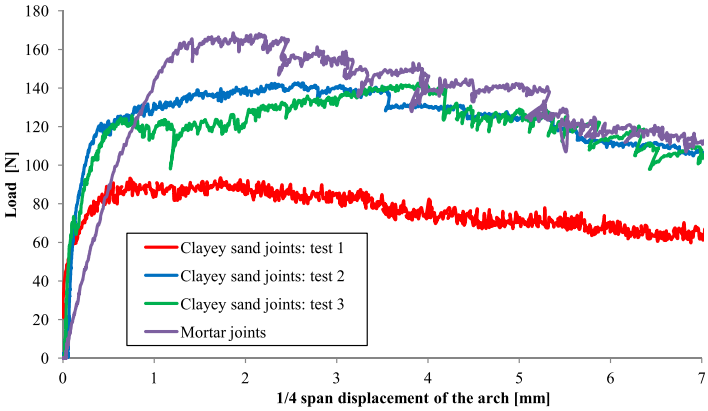

(a)

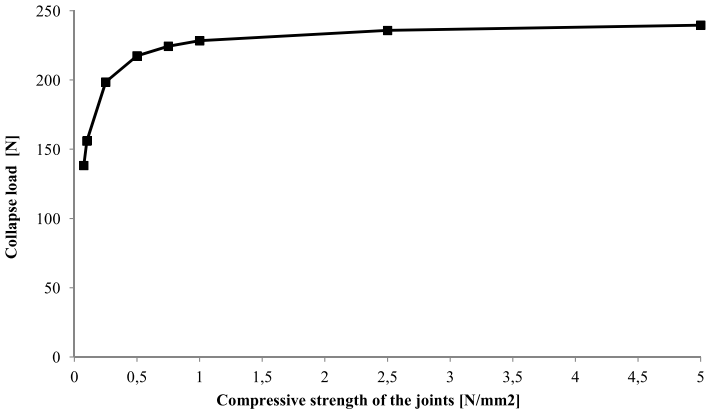

(b)

Figure 6.17.: Bare arch tests: (a) laboratory tests; (b) parametric study in LimitState:GEO

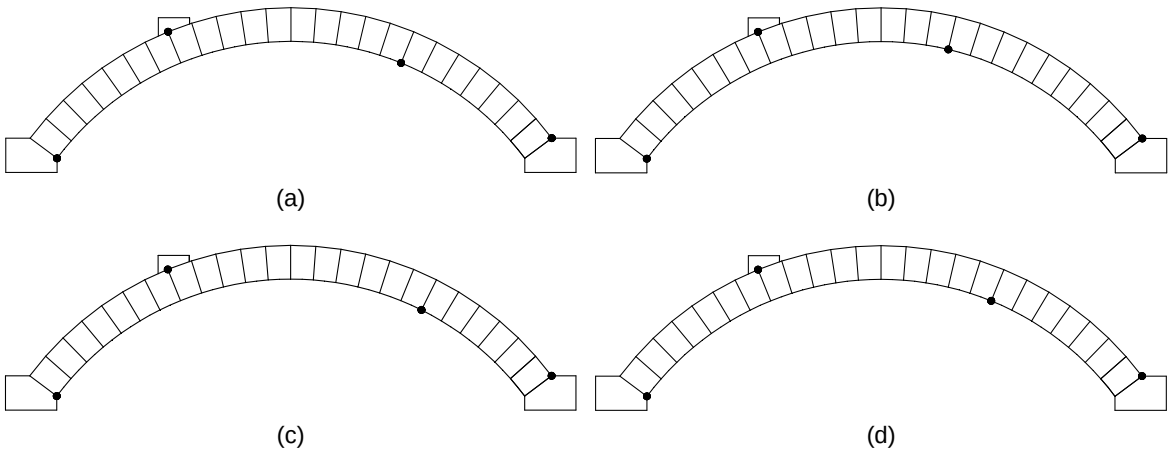

(a) (b) (c) (d)

Figure 6.18.: Location of plastic hinges in the bare arch laboratory tests (the position of the first hinge from the left is assumed as it was not visible in any of the tests): (a) clayey sand joints test 1; (b) clayey sand joints test 2; (c) clayey sand joints test 3; (d) mortar joints

6.3.2. Backfilled arch tests

In total thirteen exploratory tests involving sand backfill were conducted; in all the tests the arch barrels employed clayey sand joints. The first four tests were used to prove the equip-

ment and the testing procedure with the main focus on fine tuning of the sand conveyance and pouring system. The next nine tests were designed to explore the issue of lack of repeatability and unexpectedly low capacity of the arch-soil system; once the cause of the problem was narrowed down to the arch joints it was further investigated by the means of bare arch tests as described in Section 6.3.1. Due to time limitations, no further backfilled arch tests were subsequently conducted. The lack of information on compressive strength of joints, a crucial property when its value is so low, means that the data collected is of limited value for the analysis of backfilled masonry arch bridges. However it does prove that all the main elements of the newly developed testing facility work as expected.

In this section, sample results are presented and key practical aspects associated with using the test rig are briefly discussed.

Turnaround

Approx. 30 to 40 hours of one person's work, from preparation to clean up of the test facility, were found to be required to conduct one test. The most time consuming stages of the test are construction of the arch and the backfilling process; the former is currently very labour intensive but if the arch is to be constructed from concrete voussoirs without the need to construct the joints, as suggested in Section 6.3.1, the process would be simplified significantly. The backfilling process is currently semi-automatic and just requires several minutes of human input about 8 to 9 times during the process; it could be fully automated but the extra effort required to fine tune such system so it could work without any human supervision was judged not to warrant the additional expense required.

Backfill density

In the nine tests for which the data on backfill density was collected, the replaceable aluminium plate used in the pluvation box had 7mm diameter openings positioned at 28mm spacing and the drop height, measured from the bottom sieve of the pluvation box, was approximately 520mm. The average bulk unit weight of backfill for these tests was 17.3kN/m^3 which is significantly higher than the bulk unit weight of the same material of 16.5kN/m^3, achieved also by pluviation, from a similar height, in the small-scale masonry arch tests reported in Callaway (2007). The coefficient of variation across the nine tests was 0.75% which can be considered to be a good result and could be better in the future tests as the backfilling procedure was continually being improved until the test number twelve.

Sample results

In order to present capabilities of the testing facility in terms of collection of the test data, sample results from the last backfilled arch test conducted are given in Figures 6.20, 6.21 and 6.22. The arch in this test was backfilled to the level of 55mm above the crown; the loading arrangement is shown in Figure 6.19. In this test the loading beam was buried in order to prevent a local soil failure and the abutments were released. The load was applied in displacement control mode at the rate of 0.5mm/min

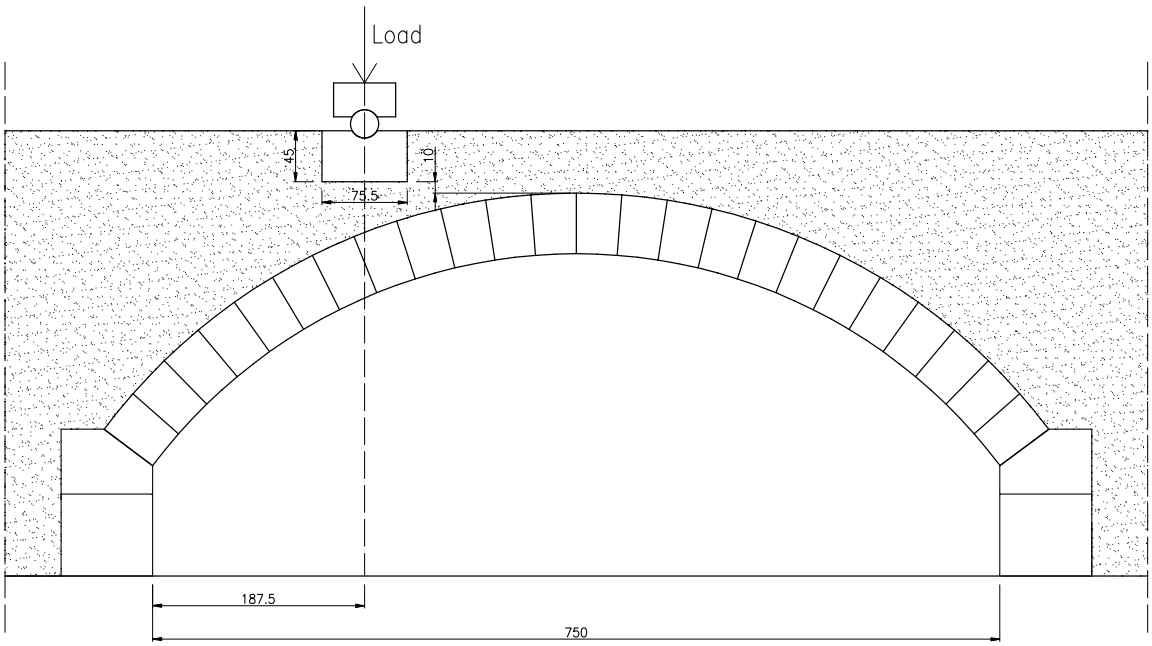

Figure 6.19.: Sample results: loading arrangement

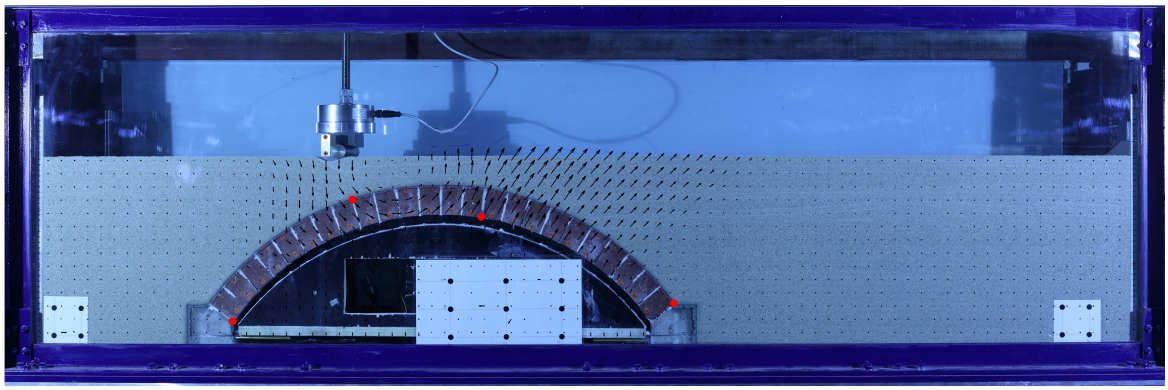

Figure 6.20.: Sample results: initial arrangement of the model with vector displacements at 5.22mm displacement of the loading beam and position of the plastic hinges superimposed; the vectors are scaled up by a factor of five

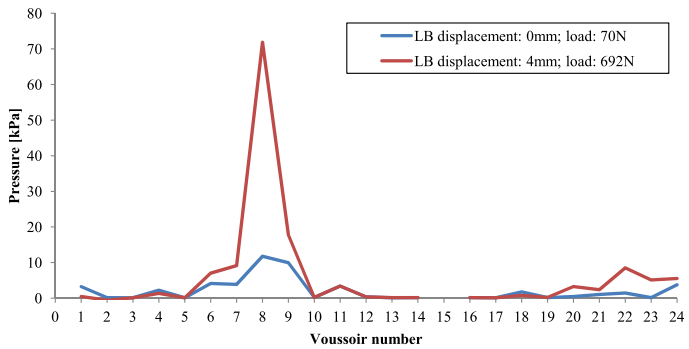

Figure 6.21.: Sample results: pressure exerted by the soil on the the arch barrel

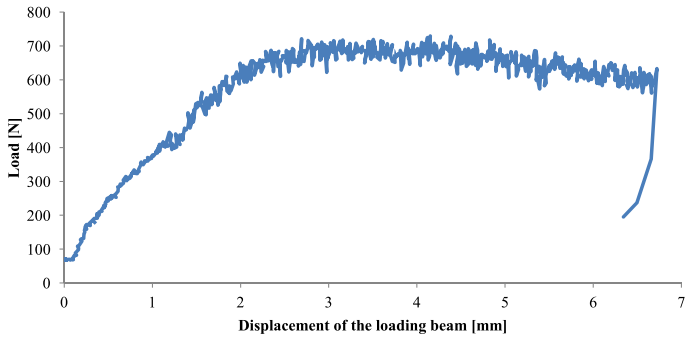

(a)

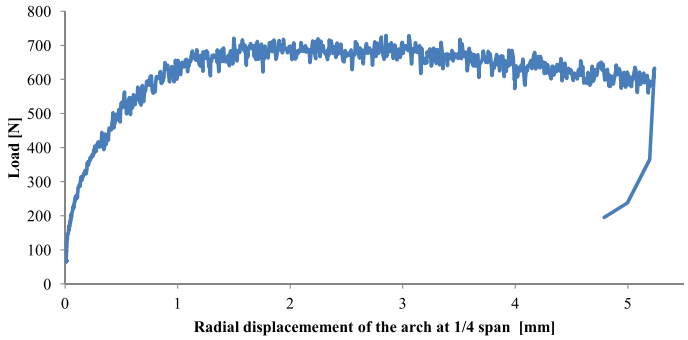

(b)

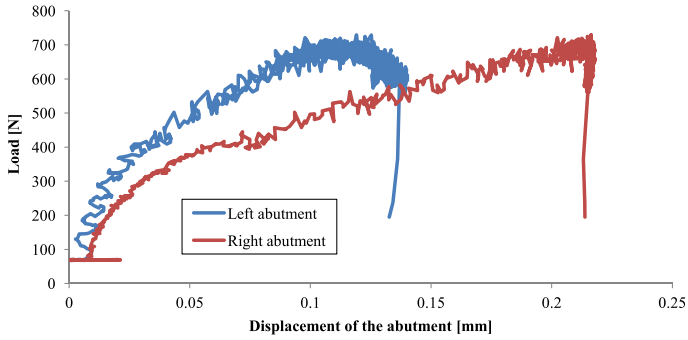

(c)

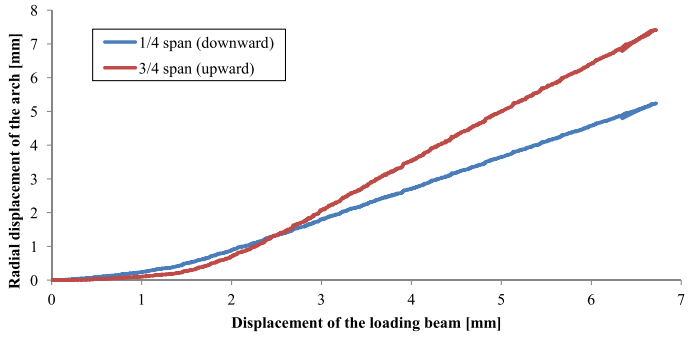

(d)

Figure 6.22.: Sample results: load-displacement behaviour of the system: (a) load v. displacement of the loading beam; (b) load v. displacement of the arch; (c) load v. displacement of the abutments; (d) displacement of the arch v. displacement of the loading beam

6.4. Summary

An innovative facility for testing of masonry arch bridges backfilled with sand was developed. The facility features instrumentation for collecting load-displacement test data, soil kinematics data and details of the pressure exerted by the soil on the arch barrel. The sand conveyance and pouring system developed for the facility allows for very good control over the backfill deposition process and requires little human input; the system makes the facility a versatile tool for testing of not only masonry arch bridges but also different types of problems involving frictional soils.

A high sensitivity of the behaviour of the model to the strength of the clayey sand arch joints used in the tests was detected; the observed behaviour could be representative of masonry arch bridges with very weak mortar joints.

Before the facility can be used for conducting further tests, it will be necessary to calibrate the soil pressure sensors using the actual backfill material used in the tests, and also to improve the arch construction procedure so that the joints have repeatable high compressive strength. In relation to the latter, the recommendation is to cast all the voussoirs from concrete, in one form, using a geometry that ensures they fit perfectly together to create an arch without additional material in the joints between them.

7. Conclusions

Over the centuries masonry arch bridges have proven to be extremely versatile and sustainable structures, with many of them far surpassing the original design assumptions, both in terms of lifespan and in terms of load capacity. Yet, in order to cope with material deterioration and ever increasing demands on performance, the existing stock requires careful management. Specifically, considering the continuing crucial role of masonry arch bridges in the UK's transport networks, the large number of spans still in service, and the limited budgets available for repair and maintenance, it is very important that engineers have access to reliable assessment methods, capable of identifying which bridges require attention.

It was identified that, with regard to the soil-structure interaction, none of the current commonly used methods of analysis provides a truly direct way of modelling the backfill and that the existing laboratory test data does not permit thorough validation of existing and proposed future methods of analysis. In order to address these problems, this study was concerned with development of new tools for numerical and physical modelling of soil-filled masonry arch bridges. This chapter summarizes outcomes and key findings from the research presented.

7.1. New numerical modelling tool

The novel contribution to knowledge of the numerical modelling part of the present study is summarized below:

(1) A novel modelling method utilizing the Box2D physics engine was proposed. The method is similar in capabilities to the traditional DEM distinct element method approach, but has two advantages with regards to modelling of the backfill: a more intuitive contact model with only one relevant contact parameter, the coefficient of friction (μ defined in Section 3.1.4), which directly represents a physical property of the soil being modelled and, potentially, much lower run times.

(2) A full description of the simulation method used in Box2D was presented, information previously not available in the literature.

(3) Box2D was validated against a range of problems for which analytical or experimental solutions exist. The physics engine was found to be capable of accurately simulating disc and block interaction dynamics.

(4) It was shown that particulate media can be faithfully modelled using the Box2D physics engine. Soil is to be modelled as an assembly of rigid bodies with its macro-scale deformation accommodated by interparticle sliding and rolling. A soil model with particles

modelled as randomly shaped polygons was developed and its macro-scale properties were determined with the developed 'biaxial compression test' program. It was demonstrated that a Box2D based simulation tool can successfully capture the critical state response of granular media.

(5) Modelling masonry arches using the Box2D physics engine was discussed. The barrel can be idealized as an assemblage of rigid bodies which allows the most common failure modes to be captured, including the formation of plastic hinges and sliding. It was demonstrated that a Box2D based simulation tool is capable of simulating load tests to failure on voussoir type arches; the simulation accuracy in all tested scenarios was found to be excellent.

(6) It was shown that Box2D simulation tools are capable of accurately simulating load tests to failure on masonry arches backfilled with frictional soil; the validation tests conducted showed that the phenomena of passive and active soil pressure mobilization can be faithfully modelled without the drawbacks of the alternative methods of analysis such as mobilization factors (limit analysis method), extensive tuning of the simulation input parameters (distinct element method) or the need for highly complex constitutive soil models (finite element method).

(7) In order to accommodate work on (4), (5) and (6) a number of C++ computer programs were developed. The overview of the programs is provided below. Programs (i), (ii), (iii) and (iv) are are essentially Box2D projects which, when compiled, accept simulation input parameters from a batch file, and run on Windows and Unix operating systems. The drawingWriter is a stand-alone Windows program with a text user interface. The source code of the developed programs is given in Appendix C.

   (i) Biaxial compression test

   A virtual equivalent of the triaxial laboratory test. It is used to determine the macro-scale properties of virtual soil materials.

   (ii) Bare arch test

   A simulator of load tests to failure on voussoir type bare masonry arches with load applied in load control mode. The program is used to test and validate new models of masonry aches before they are used in the tests with backfill.

   (iii) Simplified backfilled arch test

   A simulator of load tests to failure on masonry arches backfilled with frictional soil with load applied directly to the arch in a load control mode. This program is used when direct modelling of live load distribution can be sacrificed for the sake of speed. It is envisaged that this tool could be fitted with industry standard uniform and Bousinesq distribution models and therefore provide an alternative to the 'full backfilled arch test' program.

   (iv) Full backfilled arch test

A simulator of load tests to failure on masonry arches backfilled with frictional soil with load applied via a loading beam in displacement control mode. This tool replicates typical laboratory test settings.

(v) drawingWriter

Program for processing the output data from the programs described in (i), (ii), (iii) and (iv). It can produce figures showing the state of the model for a chosen time step with colour maps of accumulated rotations or accumulated displacement of the individual bodies superimposed; it can also produce a map of vector displacements for a chosen time step and calculate the void ratio in a specified circular region of the model. All the drawings are produced in the Asymptote format.

(8) A novel concept of a 'virtual laboratory' was proposed. The virtual soil material can be engineered using the 'biaxial compression test' program so that it has the desired macro-scale properties, i.e. matching this of the backfill from a real bridge under consideration. The developed virtual soil is then used in the backfilled arch test programs to simulate the behaviour of the arch-soil system. This concept was tested for a simple virtual soil model with particles modelled as random shaped dodecagons and it was demonstrated that the macro-scale properties of the virtual soil model are independent of the simulated scenario.

(9) A standardized procedure for determining appropriate accuracy settings for use in Box2D based simulations was proposed and tested. The procedure can be automated and guarantees that a set of Δt and N_i providing an accurate solution is found.

(10) A technique to decrease the runtime of quasi-static, Box2D based, simulations was proposed. The technique increases the accuracy of a simulation for a given Δt and N_i settings by making the problem more 'static'. This effect is achieved by increasing the density of bodies, with gravitational acceleration decreased proportionally in order to preserve the physical correctness of the simulation. Using the bare arch test program as an example, it has been demonstrated that this technique can decrease simulation runtime by a factor of 9.

(11) A technique to determine the number of soil particles required in the model to accurately replicate the desired backfill behaviour in the backfilled arch test programs was proposed and tested. The technique, originating from DEM studies (O'Sullivan, 2011), relies on a parametric study of the particle size and can be automated.

A part of the study presented in this thesis, concerning modelling granular soil behaviour using the Box2D physics engine, was published in the Géotechnique Letters journal (Pytlos et al., 2015*a*). Earlier research on this topic conducted by the author, which includes a study involving modelling retaining walls and an angle of repose test, was published in the Proceedings of the International Symposium on Geomechanics from Micro to Macro held at the University of Cambridge in 2014 (Pytlos et al., 2015*b*).

7.2. New physical modelling tool

The main outcome of the physical modelling part of the present study is the development of an innovative facility for testing of soil-filled masonry arch bridges. The facility will allow the researchers using it in the future to conduct tests quickly, yet with very good control over the model properties and to collect high quality test data on soil kinematics and soil pressures; this makes the facility unique in terms of the ability to model soil-filled masonry arch bridges, and means that it has the potential to produce much needed validation data for current and future methods of analysis. Additionally, the information contained in Chapter 6 will be useful to researchers developing similar test facilities i.e. for testing of large models involving frictional soil (in particular the novel sand conveyance and pouring system might be of interest). The main outcomes from the laboratory tests conducted are as follows:

(1) The sand conveyance and pouring system was found to be capable of producing backfill of repeatable density and with very low human input. The dust control safety measures implemented in the system provide safe working environment without the need for additional respiratory protective equipment.

(2) The proposed arch modelling approach, with the voussoirs separated by joints made of the clayey sand material, was found to be very problematic; the very low and variable strength of the joints is thought to be the primary reason for the lack of repeatability of the collapse load in both, the backfilled and the bare arch tests; the results of a numerical investigation, conducted using the LimitState:GEO software, confirmed that the load capacity of the prototype arch is highly sensitive to the compressive strength of the joints if the joints are very weak. The modelling recommendation with regard to this issue is given in Section 8.2.1.

(3) The tests conducted indicate that the low cost ($<£50$) miniature ceramic pressure sensors PC18-2G are capable of relatively accurate measurement of soil pressures in static tests providing they are calibrated in the same conditions as in those tests.

(4) A detailed method statement for tests on arches backfilled with sand was prepared. A copy of the final version of the statement, iteratively improved after each test conducted, is given in Appendix A.

8. Recommendations for further work

The aim of the present study was to develop new tools for modelling soil-filled masonry arch bridges. Great effort was made to create tools that would address current numerical and physical modelling needs and to ensure that they were of the highest quality. It is therefore imperative that these tools are now used and further developed to make a tangible impact in the field, contributing to the development of improved assessment methods for masonry arch bridges. Below are the author's recommendations for further work on, and with, the tools developed in the present study.

8.1. Box2D based numerical modelling

(1) Realistic soil models

In order for Box2D based modelling tools to be useful in engineering practice, realistic soil models must be developed and ideally a database of those created maintained. It is expected that the relation between the micro-scale properties of a real soil and its macro-scale response described in Section 4.1.1 will also hold true in the Box2D based simulations. Note that in order to have realistic interlocking between individual particles in a simulation, the particles might need to be modelled as concave bodies; this can be achieved in Box2D for example by constructing particles from several triangles clumped together.

(2) Validation against laboratory test data

Before the developed programs can be used in an engineering practice, they have to be validated against laboratory test data. Assuming that the developed test facility will be used to produce such data, the first task would be to develop virtual model of the Leighton Buzzard sand fraction B. This should be done using the biaxial compression test program, by conducting parametric studies on the particle shape, particle size distribution and particle coefficient of friction with the default parameters resembling those determined for the real sand (see Senetakis et al. (2013*b*) for information on the inter-particle coefficient of friction of the Leighton Buzzard sand). Afterwards, the laboratory test should be replicated using the full backfilled arch test program; the comparison of the results should include load displacement behaviour of the arch barrel and soil kinematics and soil pressures logged at various stages throughout the tests (note that for such comparison, the recommendation (1) from Section 8.2.1 must be realized). The results presented in Chapter 5 indicate that this approach to modelling might be successful.

(3) Simulation speed of the Box2D physics engine

Providing the recommendations (1) and (2) from this section are realized, the simulation speed of the Box2D physics engine will be the next major concern; recommendations (4), (5) and (6) in this section address this problem but further improvements can be made to the physics engine itself. Box2D is a single threaded program which means that it uses only one CPU core to run the simulation. The simulation method implemented in Box2D, or more broadly DEM, is well suited to exploit parallel computing (O'Sullivan, 2015) and significant runtime reductions can be made by implementing concurrency in Box2D (i.e. as this would allow Box2D to use several CPU cores available in every modern desktop machine or be run on a supercomputer). However, the most exciting development avenue would be to allow Box2D to harness the power of a graphics processing unit (GPU), taking advantage of technology developed originally for the computer games industry (for example the Nvidia PhysX physics engine). A typical GPU is composed of hundreds of cores and can handle thousands of threads simultaneously; this means that, potentially, Box2D simulations involving thousands of bodies could be run in a matter of seconds rather hours whilst preserving the required accuracy. The speed benefits combined with a simulation engine firmly grounded in physics would offer a modelling capability for frictional soils unrivalled by any other method of analysis currently employed in geotechnics.

(4) Guidance on the choice of N_i in the proposed standardized procedure for determining the accuracy setting in Box2D based simulations

The optimum N_i for a given number of bodies in a model should be established by the means of a parametric study.

(5) Guidance on the use of the proposed technique for reducing simulation runtime

As discussed in Section 5.2.3, when using the proposed technique for reducing simulation runtime, there is an optimum density of bodies for a given type of problem; this optimum should be established for all four developed programs by the means of a parametric study.

(6) Particle size variation across the model

The results presented in Chapter 5 show that, compared to active and passive pressure mobilization phenomena, accurate modelling of live load distribution in a backfill requires much finer soil particles to be used. This means that, potentially, significant runtime reduction in the full backfilled arch test program can be achieved by using the very fine soil particles only in the vicinity of the loading beam; the potential of this technique should be explored.

(7) Practical use of the developed programs

Providing the recommendations (1) and (2) from this section are positively realized, it would be worthwhile to make the developed programs (i) much more user friendly by developing a common, user-friendly interface and (ii) more powerful by adding extra functionality, e.g. the Bousinessq and uniform live load distribution models to the

simplified backfilled arch test program, multi-ring arch models, a database of virtual soil models replicating behaviour of the most common soil types, guidance on how behaviour can be fine-tuned if required and inclusion of crushing strength into the masonry model, in a similar manner as in the LimitState:RING program (LimitState, 2014*b*).

(8) Wider perspective: geotechnics

Due to the potential significant advantages over the distinct element method discussed in Section 3.1.7, the physics engine based simulation tools might be very attractive in the broader field of geotechnics. There is a range of geotechnical problems which are traditionally modelled in plane strain (retaining walls, earth dams, footings, slope stability etc.) where Box2D can be used as a modelling tool and this opportunity should be explored (the author has already successfully modelled smooth retaining walls using Box2D (Pytlos et al., 2015*b*)).

(9) Three-dimensional analysis

Clearly, the long term goal would be to employ physics engine based modelling tools to three-dimensional analysis. Initial attempts at modelling soil with a 3D physics engine Bullet (Coumanns, 2012) were described by Izadi and Bezuijen (2015) with promising results but the technical report produced by LimitState (2013), which involved more fundamental studies, concluded that it does not currently model friction accurately when numerous objects are involved in the simulation. Perhaps the best approach would be to use an existing 3D open-source physics engine, such as Bullet, as a foundation and make an attempt to directly extend the sound simulation method implemented in Box2D, which was rigorously validated in the present study, into three dimensions.

8.2. Test facility

8.2.1. Further development

(1) Masonry arch joints

As discussed in Section 6.3.1, the clayey sand joints used in the tests conducted are not suitable for the models as their very low and variable compressive strength has significant influence on the arch behaviour and is difficult to account for. Instead of using the fabricated voussoirs which require joints to be constructed, it is therefore recommended that a new set of voussoirs is fabricated which have slightly modified geometry so there is no need to construct joints at all. This would remove the parameter of compressive joint strength from consideration and shift the focus of the tests to soil-arch interaction. Such voussoirs can, for example, be cast from concrete in one form as achieving the required tolerance on separately made voussoirs, for example cut from bricks, would be very costly and time consuming.

(2) Calibration of the pressure sensors in sand

The pressure sensors used in the tests were calibrated in water only. The relation between the sensitivity of the PC18-2G transducer in water and in sand was established in triaxial calibration tests but the material used did not have the same properties as that used in the masonry arch tests, and only one transducer was tested. However, the fabricated pressure sensor calibration device, currently used for calibration in water only, can relatively easily be adapted for calibration in sand (an additional collar and a latex membrane have to be added and the device will have the same functionality as the calibration chamber described in Talesnick (2005)). Such modification would make it possible to calibrate, with relatively low effort, all the pressure sensors in conditions similar to those present in the masonry arch tests.

8.2.2. Testing

(1) Validation data

It is recommended that, once the two issues described in Section 8.2.1 are resolved, a series of tests involving varying the height and density of the backfill are conducted. The results should be made publicly available so they can be used to validate existing and future methods of analysis for soil-filled masonry arch bridges.

(2) Density of sand deposited using the sand conveyance and pouring system

A series of tests with different replaceable aluminium plates for the pluviation box should be conducted in order to establish the relation between the diamater of the openings and the density of the deposited sand when using the developed sand conveyance and pouring system.

(3) Quantifying the effect of friction between the glass walls and the sand mass on the test results

The test facility was designed for tests on 200, 400 and 800mm wide models. A test on a 400mm wide model should be conducted and the results compared to those from a test on 200mm wide model, tested under the same conditions, in order to quantify the effect of friction between the glass walls and the sand mass on the test results.

(4) Further parametric studies

The developed test facility allows high quality test data to be collected, and for tests to be conducted quickly and with good control over the model properties. This make it an excellent tool to conduct multiple parametric studies that will deepen our knowledge in the area of soil-structure interaction in masonry arch bridges. It is hoped that researchers at the University of Sheffield will take advantage of this opportunity.

9. References

Ashby, J. (1971), *Sliding and toppling modes of failure in models and jointed rock slopes*, MSc thesis, Department of Mining, Imperial College of Science and Technology, London.

Azéma, E. and Radjaï, F. (2010), 'Stress-strain behavior and geometrical properties of packings of elongated particles', *Physical Review E* **81**(5), 051304.

Babiker, A., Smith, C., Gilbert, M. and Ashby, J. (2014), 'Non-associative limit analysis of the toppling-sliding failure of rock slopes.', *International Journal of Rock Mechanics Mining Sciences* **71**, 1–11.

Baraff, D. (1997*a*), *An Introduction to Physically Based Modeling: Rigid Body Simulation I-Unconstrained Rigid Body Dynamics*, SIGGRAPH '97 Course Notes, Carnegie Mellon University, Pittsburgh.

Baraff, D. (1997*b*), *An Introduction to Physically Based Modeling: Rigid Body Simulation II-Nonpenetration Constraints*, SIGGRAPH '97 Course Notes, Carnegie Mellon University, Pittsburgh.

Bender, J., Erleben, K. and Trinkle, J. (2014), 'Interactive simulation of rigid body dynamics in computer graphics', *Computer Graphics Forum* **33**(1), 246–270.

Bender, J., Erleben, K., Trinkle, J. and Coumans, E. (2012), Interactive simulation of rigid body dynamics in computer graphics, *in* 'EUROGRAPHICS 2012-Proceedings of State of the Art Reports, Cagliari, 2012', pp. 95–134.

Brown, M. J. (2004), *The rapid load testing of piles in fine grained soils*, PhD thesis, Department of Civil and Structural Engineering, University of Sheffield, Sheffield.

Burroughs, P., Hughes, T., Hee, S. and Davies, M. (2002), 'Passive pressure development in masonry arch bridges', *Proceedings of the ICE-Structures and Buildings* **152**(4), 331–339.

Callaway, P. A. (2007), *Soil-Structure Interaction in Masonry Arch Bridges*, PhD thesis, Department of Civil and Structural Engineering, University of Sheffield, Sheffield.

Callaway, P., Gilbert, M. and Smith, C. C. (2012), 'Influence of backfill on the capacity of masonry arch bridges', *Proceedings of the ICE-Bridge Engineering* **165**(3), 147–158.

Catto, E. (2006), 'Fast and simple physics using sequential impulses'. PowerPoint presentation. Presented at the Game Developers Conference, San Jose, CA, 2006.
URL: *https://code.google.com/p/box2d/downloads/*

Catto, E. (2009), ‘Modeling and solving constraints’. PowerPoint presentation. Presented at the Game Developers Conference, San Francisco, CA, 2009.
URL: *https://code.google.com/p/box2d/downloads/*

Catto, E. (2011), ‘Box2D: A 2D Physics Engine for Games’. software, version 2.2.1.
URL: *http://box2d.org/*

Catto, E. (2013), ‘Box2D v2.3.0 User Manual’.
URL: *http://box2d.org/*

Catto, E. (2014), ‘Understanding constraints’. PDF presentation. Presented at the Game Developers Conference, San Francisco, CA, 2014.
URL: *http://box2d.org/downloads/*

Catto, E. (2015), ‘Numerical methods’. PDF presentation. Presented at the Game Developers Conference, San Francisco, CA, 2015.
URL: *http://box2d.org/downloads/*

Cavicchi, A. and Gambarotta, L. (2005), ‘Collapse analysis of masonry bridges taking into account arch–fill interaction’, *Engineering Structures* **27**(4), 605–615.

Cho, G.-C., Dodds, J. and Santamarina, J. C. (2006), ‘Particle shape effects on packing density, stiffness, and strength: natural and crushed sands’, *Journal of Geotechnical and Geoenvironmental Engineering* **132**(5), 591–602.

Choo, B., Coutie, M. and Gong, N. (1991), ‘Finite-element analysis of masonry arch bridges using tapered elements’, *Proceedings of the ICE* **91**(4), 755–770.

Coumanns, E. (2012), ‘Bullet physics library’. software, version 2.80.
URL: *http://bulletphysics.org/*

Cundall, P. (2001), ‘A discontinuous future for numerical modelling in geomechanics?’, *Proceedings of the Institution of Civil Engineers: Geotechnical Engineering* **149**(1), 41–47.

Cundall, P. A. and Hart, R. D. (1992), ‘Numerical modelling of discontinua’, *Engineering Computations* **9**(2), 101–113.

Cundall, P. A. and Strack, O. D. (1979), ‘A discrete numerical model for granular assemblies’, *Geotechnique* **29**(1), 47–65.

Davies, M., Hughes, T. and Taunton, P. (1998), ‘Centrifuge testing of model masonry arch bridges’, *Proceedings of the ICE-Geotechnical Engineering* **131**(3), 141–145.

Erleben, K. (2005), *Stable, Robust, and Versatile Multibody Dynamics Animation*, PhD thesis (Revised version, April 2005), Department of Computer Science, University of Copenhagen, Copenhagen.

Fairfield, C. and Ponniah, D. (1994), ‘Model tests to determine the effect of fill on buried arches.’, *Proceedings of the ICE-Structures and Buildings* **104**(4), 471–482.

Fang, Y.-S., Chen, T.-J., Holtz, R. D. and Lee, W. F. (2004), 'Reduction of boundary friction in model tests', *Geotechnical Testing Journal* **27**(1), 3–12.

Fang, Y.-S., Ho, Y.-C. and Chen, T.-J. (2002), 'Passive earth pressure with critical state concept', *Journal of Geotechnical and Geoenvironmental Engineering* **128**(8), 651–659.

Garnier, J., Gaudin, C., Springman, S., Culligan, P., Goodings, D., Konig, D., Kutter, B., Phillips, R., Randolph, M. and Thorel, L. (2007), 'Catalogue of scaling laws and similitude questions in geotechnical centrifuge modelling', *International Journal of Physical Modelling in Geotechnics* **7**(3), 1–23.

Gilbert, M. (1998), On the analysis of multi-ring brickwork arch bridges, *in* 'Proceedings of the 2nd International Arch Bridges Conference, Venice, 1998', pp. 109–118.

Gilbert, M. (2007), Limit analysis applied to masonry arch bridges: state-of-the-art and recent developments, *in* 'Proceedings of the 5th International Conference on Arch Bridges, Madeira, 2007', pp. 13–28.

Gilbert, M., Casapulla, C. and Ahmed, H. (2006), 'Limit analysis of masonry block structures with non-associative frictional joints using linear programming', *Computers & structures* **84**(13), 873–887.

Gilbert, M. and Melbourne, C. (1994), 'Rigid-block analysis of masonry structures', *The Structural Engineer* **72**(21), 356–361.

Gilbert, M., Smith, C. C. and Pritchard, T. J. (2010), 'Masonry arch analysis using discontinuity layout optimisation', *Proceedings of the ICE-Engineering and Computational Mechanics* **163**(3), 155–166.

Griffiths, D. and Lane, P. (1999), 'Slope stability analysis by finite elements', *Geotechnique* **49**(3), 387–403.

Hammerlindl, A., Bowman, J. and Prince, T. (2014), 'Asymptote: the vector graphics language'. software, version 2.35.
URL: *http://asymptote.sourceforge.net/*

Hendry, A., Davies, S. and Royles, R. (1985), *Test on stone masonry arch at Bridgemill - Girvan*, Contractor report 7, Transport and Road Research Laboratory, Crowthorne.

Hendry, A., Davies, S., Royles, R., Ponniah, D., Forde, M. and Komeyli-Birjandi, F. (1986), *Load test to collapse on a masonry arch bridge at Bargower, Strathclyde*, Contractor report 26, Transport and Road Research Laboratory, Crowthorne.

Heyman, J. (1966), 'The stone skeleton', *International Journal of Solids and Structures* **2**(2), 249–279.

Highways Agency (2001*a*), *Highway Structures: Inspection and Maintenance. Assessment. The Assessment of Highway Bridges and Structures*, DMRB Volume 3 Section 4 Part 4 (BA 16/97), Highways Agency, London.

Highways Agency (2001*b*), *Highway Structures: Inspection and Maintenance. Assessment. The Assessment of Highway Bridges and Structures*, DMRB Volume 3 Section 4 Part 3 (BD 21/01), Highways Agency, London.

Hoek, E. and Bray, J. (1981), *Rock slope engineering*, 3rd edition, The Institution of Mining and Metallurgy, London.

Huang, X., Hanley, K. J., O'Sullivan, C. and Kwok, C. Y. (2014), 'Exploring the influence of interparticle friction on critical state behaviour using dem', *International Journal for Numerical and Analytical Methods in Geomechanics* **38**(12), 1276–1297.

Hughes, T. and Blackler, M. (1997), 'A review of the uk masonry arch assessment methods', *Proceedings of the ICE-Structures and Buildings* **122**(3), 305–315.

Hughes, T., Davies, M. and Taunton, P. (1998), 'Small scale modelling of brickwork arch bridges using a centrifuge', *Proceedings of the Institution of Civil Engineers. Structures and buildings* **128**(1), 49–58.

Hulet, K. M., Smith, C. C. and Gilbert, M. (2006), 'Load-carrying capacity of flooded masonry arch bridges', *Proceedings of the ICE-Bridge Engineering* **159**(3), 97–103.

Izadi, E. and Bezuijen, A. (2015), Simulation of granular soil behaviour using the Bullet physics library, *in* 'Proceedings of the TC105 ISSMGE International Symposium on Geomechanics from Micro to Macro, Cambridge, 2014', Vol. 2, pp. 1565–1570.

Jean, M. (1999), 'The non-smooth contact dynamics method', *Computer methods in applied mechanics and engineering* **177**(3), 235–257.

Jing, L. (2003), 'A review of techniques, advances and outstanding issues in numerical modelling for rock mechanics and rock engineering', *International Journal of Rock Mechanics and Mining Sciences* **40**(3), 283–353.

Ke, T.-C. and Bray, J. (1995), 'Modeling of particulate media using discontinuous deformation analysis', *Journal of Engineering Mechanics* **121**(11), 1234–1243.

Krabbenhoft, K., Lyamin, A., Huang, J. and da Silva, M. V. (2012), 'Granular contact dynamics using mathematical programming methods', *Computers and Geotechnics* **43**, 165–176.

Labuz, J. F. and Theroux, B. (2005), 'Laboratory calibration of earth pressure cells', *Geotechnical Testing Journal* **28**(2), 188–196.

LimitState (2011), *LimitState:RING Manual*, version 3.0, LimitState Ltd, Sheffield.

LimitState (2013), *Computationally Efficient Methods to Model Blast Effects on Masonry Walls*, Unpublished LimitState technical report LSR1-13.

LimitState (2014*a*), 'LimitState:RING'. software, version 3.1.b.
URL: *http://www.limitstate.com/ring*

LimitState (2014*b*), *LimitState:RING Manual*, version 3.1.b, LimitState Ltd, Sheffield.

LimitState (2015*a*), 'LimitState:GEO'. software, version 3.2.d.
URL: *http://www.limitstate.com/geo*

LimitState (2015*b*), *LimitState:GEO Manual*, version 3.2.d, LimitState Ltd, Sheffield.

McKibbins, L. D., Melbourne, C., Sawar, N. and Sicilia Gaillard, C. (2006), *Masonry arch bridges: condition appraisal and remedial treatment*, CIRIA.

Melbourne, C. and Gilbert, M. (1995), 'The behaviour of multiring brickwork arch bridges', *The Structural Engineer* **73**(3), 39–47.

Melbourne, C. and Walker, P. (1990), *Load test to collapse on a full scale model six metre span brick arch bridge*, Contractor report 189, Transport and Road Research Laboratory, Crowthorne.

Melbourne, C., Wang, J., Tomor, A., Holm, G., Smith, M., Bengtsson, P., Bien, J., Kaminski, T., Rawa, P., Casas, J., Roca, P. and Molins, C. (2007), *Masonry Arch Bridges Background Document D4.7*, Sustainable Bridges Deliverable D4.7, EU FP6.

Miura, S. and Toki, S. (1982), 'A sample preparation method and its effect on static and cyclic deformation-strength properties of sand', *Soils and Foundations* **22**(1), 61–77.

Morgan, J. K. (1999), 'Numerical simulations of granular shear zones using the distinct element method: 2. effects of particle size distribution and interparticle friction on mechanical behavior', *Journal of Geophysical Research: Solid Earth* **104**(B2), 2721–2732.

Morgan, J. K. and Boettcher, M. S. (1999), 'Numerical simulations of granular shear zones using the distinct element method: 1. shear zone kinematics and the micromechanics of localization', *Journal of Geophysical Research: Solid Earth* **104**(B2), 2703–2719.

Morrow, C. A. and Byerlee, J. D. (1989), 'Experimental studies of compaction and dilatancy during frictional sliding on faults containing gouge', *Journal of Structural Geology* **11**(7), 815–825.

Nielsen, J. H. (2009), *Tempered Glass-bolted connections and related problems*, PhD thesis, Department of Civil Engineering, Technical University of Denmark, Kongens Lyngby.

Nouguier-Lehon, C., Cambou, B. and Vincens, E. (2003), 'Influence of particle shape and angularity on the behaviour of granular materials: a numerical analysis', *International Journal for Numerical and Analytical Methods in Geomechanics* **27**, 1207–1226.

O'Sullivan, C. (2011), 'Particle-based discrete element modeling: Geomechanics perspective', *International Journal of Geomechanics* **11**(6), 449–464.

O'Sullivan, C. (2015), Advancing geomechanics using DEM, *in* 'Proceedings of the TC105 ISSMGE International Symposium on Geomechanics from Micro to Macro, Cambridge, 2014', Vol. 1, pp. 21–32.

O'Sullivan, C. and Bray, J. D. (2003), 'Modified shear spring formulation for discontinuous deformation analysis of particulate media', *Journal of Engineering Mechanics* **129**(7), 830–834.

Page, J. (1987), *Load tests to collapse on two arch bridges at Preston, Shropshire and Prestwood, Staffordshire*, Research report 110, Transport and Road Research Laboratory, Crowthorne.

Page, J. (1988), *Load tests to collapse on two arch bridges at Torksey and Shinafoot*, Research report 159, Transport and Road Research Laboratory, Crowthorne.

Page, J. (1989), *Load tests to collapse on two arch bridges at Strathmashie and Barlae*, Research report 201, Transport and Road Research Laboratory, Crowthorne.

Page, J. (1993), *Masonry arch bridges*, HM Stationery Office, London.

Pippard, A. J. S., Tranter, E. and Chitty, L. (1936), 'The mechanics of the voussoir arch', *Journal of the Institution of Civil Engineers* **4**(2), 281–306.

Ponniah, D., Fairfield, C. and Prentice, D. (1997), 'Fill stresses in a new brick arch bridge subject to heavy axle-load tests.', *Proceedings of the ICE-Structures and Buildings* **122**(2), 173–185.

Pytlos, M., Gilbert, M. and Smith, C. (2015*a*), 'Modelling granular soil behaviour using a physics engine', *Geotechnique Letters* **5**(4), 243–249.

Pytlos, M., Gilbert, M. and Smith, C. (2015*b*), Simulation of granular soil behaviour using physics engines, *in* 'Proceedings of the TC105 ISSMGE International Symposium on Geomechanics from Micro to Macro, Cambridge, 2014', Vol. 1, pp. 163–168.

Radjai, F. and Richefeu, V. (2009), 'Contact dynamics as a nonsmooth discrete element method', *Mechanics of Materials* **41**(6), 715–728.

Rothenburg, L. and Bathurst, R. (1992), 'Micromechanical features of granular assemblies with planar elliptical particles', *Geotechnique* **42**(1), 79–95.

Rowe, P. W. (1962), 'The stress-dilatancy relation for static equilibrium of an assembly of particles in contact', *Proceedings of the Royal Society of London. Series A. Mathematical and Physical Sciences* **269**(1339), 500–527.

Senetakis, K., Coop, M. R. and Todisco, M. (2013*a*), 'Tangential load–deflection behaviour at the contacts of soil particles', *Géotechnique Letters* **3**(2), 59–66.

Senetakis, K., Coop, M. R. and Todisco, M. C. (2013*b*), 'The inter-particle coefficient of friction at the contacts of Leighton Buzzard sand quartz minerals', *Soils and Foundations* **53**(5), 746–755.

Smith, C., Gilbert, M. and Callaway, P. (2004), Geotechnical issues in the analysis of masonry arch bridges, *in* 'Proceedings of the 4th International Conference on Arch Bridges, Barcelona, 2004', pp. 343–352.

Smith, C., Gilbert, M., Melbourne, C. and Wang, J. (2006), Full scale modelling of soil-structure interaction in masonry arch bridges, *in* 'Proceedings of the 6th International Conference on Physical Modelling in Geotechnics, Hong Kong, 2006', pp. 247–252.

Staron, L. and Hinch, E. (2007), 'The spreading of a granular mass: role of grain properties and initial conditions', *Granular Matter* **9**, 205–217.

Talesnick, M. (2005), 'Measuring soil contact pressure on a solid boundary and quantifying soil arching', *Geotechnical Testing Journal* **28**(2), 171–179.

Tatsuoka, F. and Haibara, O. (1985), 'Shear resistance between sand and smooth or lubricated surfaces', *Soils and Foundations* **25**(1), 89–98.

Thavalingam, A., Bicanic, N., Robinson, J. and Ponniah, D. (2001), 'Computational framework for discontinuous modelling of masonry arch bridges', *Computers & structures* **79**(19), 1821–1830.

Thornton, C. and Randall, C. (1988), Applications of theoretical contact mechanics to solid particle system simulation, *in* 'Proceedings of the U.S./Japan Seminar on the Micromechanics of Granular Materials, Sendai-Zao, 1987', pp. 133–142.

Tóth, A. R., Orbán, Z. and Bagi, K. (2009), 'Discrete element analysis of a stone masonry arch', *Mechanics Research Communications* **36**(4), 469–480.

Wang, J., Haynes, J. and Melbourne, C. (2013), A comparison between the MEXE and Pippard's methods of assessing the load carrying capacity of masonry arch bridges, *in* 'Proceedings of the 7th International Conference on Arch Bridges, Trogir-Split, 2013', pp. 589–596.

Wang, J. and Melbourne, C. (2010), 'Mechanics of MEXE method for masonry arch bridge assessment', *Proceedings of the ICE-Engineering and Computational Mechanics* **163**(3), 187–202.

Wang, J., Smith, C., Gilbert, M. and Melbourne, C. (2011), *Load Test to Collapse of a Backfilled Brickwork Masonry Arch Bridge*, Unpublished data report: Salford Soil Arch 0001.

Weiler, W. A. and Kulhawy, F. H. (1982), 'Factors affecting stress cell measurements in soil', *Journal of the Geotechnical Engineering Division* **108**(12), 1529–1548.

White, D., Take, W. and Bolton, M. (2003), 'Soil deformation measurement using particle image velocimetry (PIV) and photogrammetry', *Géotechnique* **53**(7), 619–631.

Wood, D. M. (1990), *Soil behaviour and critical state soil mechanics*, Cambridge University Press, Cambridge.

Wood, D. M. (2004), *Geotechnical modelling*, Spon Press, Abingdon.

Zhao, Y., Gafar, K., Elshafie, M., Deeks, A., Knappett, J. and Madabhushi, S. (2006), Calibration and use of a new automatic sand pourer, *in* 'Proceedings of the 6th International Conference on Physical Modelling in Geotechnics, Hong Kong, 2006', pp. 265–270.

Appendices

A. Method statement for static load tests to failure on medium-scale models of masonry arch bridges backfilled with sand

Test:

No	Task	Subtask	Notes I	Notes II
1	**Preparation**	Inspect the wiring of the pressure sensors	Check the crimps, sleeves on wires etc. If not OK, ask technical staff to repair	
		Check the output from each pressure sensor	DO NOT EXCEED 200 kPa! Complete the information on the broken sensors in the pressure sensors sheet. In tests with the arch loaded at 1/4 span, the positions 5-10 and 15-24 should feature working sensors; if required, swap bricks and make note of it in the pressure sensors sheet	requires 2 people
		Cover the pressure sensors with a masking tape	This is to protect the sensors from the ingress of water during the arch construction procedure	
2	**Abutment placement**	Insert the rods into the abutments	Secure the rods with the wooden swing plates	
		Position the top parts of the abutments		
3	**LVDT initial placement**	Mount the LVDTs on the stand	Lower the LVDTs so their tips will be well below the top of the centring; set the flat part of the LVDT3 to be 10mm above the holding block	
		Position the abutment LVDTs (1 and 5)	Set the LVDTs to ~14mm	
4	**Centring placement**	Seal the LVDT openings in the centring with an absorbent cloth	Use a masking tape to attach the cloth	
		Place the centring in the tank	The centring is not symmetrical! Make sure the LVDT openings are on the proper side of the tank	requires 2 people
		Insert the centring-to-abutment spacers	Make sure it will be possible to remove the spacers once the arch is constructed	

		Position the centring	Make sure the centring is parallel to the front glass; set the space between the centring and the glass to 2.0mm; set the height so the springer voussoirs align correctly with the abutments	requires 2 people
5	**Arch construction**	Put the glass protector sheets in place		
		Build the arch	The bricks are to be separated only by the spacers at this stage. Push the bricks lightly against the protector sheet so there is no gap between the bricks and the sheet	
		Connect the pressure sensors		requires 2 people
		Check the output from each pressure sensor	DO NOT EXCEED 200 kPa! Complete the information on the broken sensors in the pressure sensors sheet	requires 2 people
		Seal the joints from the back side	Use a duct tape	
		Feed approx 15 g of the clayey sand mix into each joint		
		Feed water into each joint		
		Lightly tamp the mix in each joint		
		Repeat the last 3 steps		
		Top up each joint with the mix		
		Feed water into each joint		
		Make sure the joints are not hollow	Use 1.5mm spacer for the check. If hollow, force in the mix; use damp material	
		Remove the spacers and the duct tape		
		Seal the gaps in the joints, made by the spacers, with the mix	Use damp material	
		Remove the centring-to-abutment spacers		

		Remove the masking tape from the pressure sensors		
		Brush off the excess mix from the arch		
		Remove the glass protector sheets		
		Remove the absorbent cloths from the centring		
		Position the barrel LVDTs (2, 3 and 4)	Make sure the tip of the LVDT 3 is positioned on a brick and not on the joint; Make sure the tips of the LVDTs 2 and 4 are on the lines marking 1/4 and 3/4 span respectively. Working range of the LVDTs: 0-15.0mm (fully retracted=15.0mm); LVDTs that will retract during the test are to be set to ~1mm; LVDTs that will extend during the test are to be set to ~14mm	requires 2 people
		Check the output of the pressure sensors	DO NOT EXCEED 200 kPa! Complete the information on the broken sensors in the pressure sensors sheet	requires 2 people
		For each of the pressure sensors: verify that the output is zero when the sensor is not loaded	If the output is outside -0.5 to 0.5 kPa range: write down the value and change the offset to bring the output to zero	
		Fill the gap between the arch and the front glass with the silicone grease	Make sure the abutments are sealed off too. Wipe off the excess.	
		Apply the silicone grease on the top of the brick joints	Treat joints between the following pairs of bricks: 14-15; 15-16; 16-17	
		Clean the floor of the tank		
		Clean the front glass from the inside	Use a floodlight to help with the inspection of the glass	

6	**Preparation for backfill placement**	Move the back glass wall to the specified position and secure it with bolts	Raise the wall -> move the wall to the specified position -> insert 2x top and 2x bottom spacers -> lower the wall -> push the bottom part of the wall using the spreaders so the tank width is as close to 200 mm as possible -> tighten bottom bolts on the frame -> push the top parts of the back and front walls apart using the spreaders -> remove the top spacers -> tighten top bolts; be careful to not scratch the glass	requires 2 people
		Seal the gaps between the glass walls and the side alu plates	This is to prevent sand leakage during the test. Use a duct tape	
		Seal the gaps between the arch and the back glass wall with the silicone grease	Make sure the abutments are sealed off too. Wipe off the excess.	
		Clean the inside of the tank		
		Clean the LMS rails	use a vacuum cleaner; make sure there is no sand below the saddles	
		Attach the sand box to the electric actuator	Set LMS to 1.8 -> set the electric actuator to 250 -> remove the cap from the hopper pipe (wear safety glasses during this task) -> attach the sand box to the actuator -> remove the handle from the bolt	requires 2 people
		Make sure the sand box will not scratch the glass during backfilling	Set the actuator to 440 and make sure the sand box is exactly in the middle between the glass walls-> set the actuator to 600 and check the sand box position between the glass walls	requires 2 people
		Connect up the sand conveyance system		
		Set up the 2D motion system for backfilling	set the electric actuator to 400 -> send LMS to the start pos -> set the electric actuator to 600 -> set the LMS speed to 0.014 -> set the LMS timer to 10000 -> set LMS WAIT to 3.6 -> select the input file	
		Complete the information in the density calcs sheet		
		Switch on the dust extractor		

7	**Backfilling (sand)**	Transport approx 15 kg of the sand to the hopper	When finished transporting the sand, immediately proceed to the next step	
		Run the automatic filling procedure	Make sure LMS is enabled -> press start -> switch off the vacuum	
		Complete the information in the density calcs sheet		
		Edit the input file (do this only if required)	write down the current height -> stop the LabView programme -> run the LabView programme -> move LMS to the required position -> close the LabView programme -> edit and save the input file -> run the LabView programme -> set up the LMS speed, WAIT and timer -> select the input file	
		Repeat the last four steps until the tank is filled to the specified level	in the default setting: 350mm height (10mm above the crown)	
		Dismount the sand box	Set LMS to 1.8m -> set the electric actuator to 250mm -> disconnect the feeder pipe -> attach the cap to the hopper's pipe -> dismount the sand box	requires 2 people
		Clean the LMS rails	Use a vacuum cleaner	
		Attach the T-suction device to the electric actuator	attach the T-suction device -> remove the handle from the bolt	
		Ensure that the T-suction device will not scratch the glass	move the electric actuator down and guide the T-suction device so it is exactly in the middle between the glass walls	
		Level the sand surface using the T-suction device	set the LMS speed to 0.005 -> remove no more that 10 mm of the backfill material at one pass	
		Remove the T-suction device		
		Complete the information in the density calcs sheet		
		Place the loading beam at the specified position	Quarter span = 603 mm from the side alu plate to the center of the beam. Space between the beam and the glass = 5mm on each side. Make sure the beam is perpendicular to the glass	requires 2 people

Attach the sand box to the electric actuator	Set LMS to 1.8m -> set the electric actuator to 250mm -> remove the cap from the hopper pipe (wear safety glasses during this task) -> attach the sand box to the actuator -> remove the handle from the bolt	requires 2 people
Connect up the sand conveyance system		
Set up the 2D motion system for backfilling	set LMS to the required position -> set the electric actuator to the required height -> set the LMS speed to 0.014 -> set the LMS timer to 10000 -> set LMS WAIT to 3.6 -> select the input file	
Complete the information in the density calcs sheet		
Switch on the dust extractor		
Transport the required amount of the sand to the hopper	In the default test: 10kg for the active side and 15+15 kg for the passive side	
Run the automatic filling procedure	Make sure LMS is enabled -> press start -> switch off the vacuum	
Edit the input file (do this only if required)	write down the current height -> stop the LabView programme -> run the LabView programme -> move LMS to the required position -> close the LabView programme -> edit and save the input file -> run the LabView programme -> set up the LMS speed, WAIT and timer -> select the input file	
Repeat the last three steps until the tank is filled to the specified level	The backfill surface is to be level with the top of the loading beam (395 mm in the default test)	
Dismount the sand box	Set LMS to 1.8m -> set the electric actuator to 250mm -> disconnect the feeder pipe -> attach the cap to the hopper's pipe -> dismount the sand box	requires 2 people
Attach the T-suction device to the electric actuator	attach the T-suction device -> remove the handle from the bolt	
Clean the LMS rails	Use a vacuum cleaner	
Ensure that the T-suction device will not scratch the glass	move the electric actuator down and guide the T-suction device so it is exactly in the middle between the glass walls	

		Level the sand surface using the T-suction device	set LMS speed to 0.005 -> remove no more that 10 mm of the backfill material at one pass	
		Remove the T-suction device		
		Complete the information in the density calcs sheet		
8	**Loading arrangement (static)**	Attach the PT load cell to the hydraulic actuator	DO NOT GO HOME WITH LMS WHILE THE LOAD CELL IS ATTACHED	
		Connect the cable to the PT load cell		
		Set the top part of the loading beam to be perpendicular to the glass	Use square	
		Roughly position the hydraulic actuator above the loading beam	DO NOT GO HOME WITH LMS WHILE THE LOAD CELL IS ATTACHED	
9	**Imaging arrangement**	Place the screen board at the back of the test rig		
		Mount the camera on the frame		
		Check the camera settings	Take a picture and check: RAW; 21.0 megapixels; ISO lowest possible (100 is normal); picture style = standard; aperture priority mode use f/5.6	
		Close the window blinds		
		Check the position of the camera	Make sure the camera is parallel to the rig; the camera is to be connected to the PC via a usb cable at this stage	
		Position the floodlights	Ensure there are no reflections on the images and the model is illuminated uniformly; switch off ceiling lights for this check	
		Set the camera focus	subject distance = 310 cm -> depth of field = 134.1 cm with near limit = 256.8cm and far limit = 390.9cm. Check whether an object 50cm in front of the model and an object 80cm behind the model both appear to be in focus	
		Clean the front glass from the outside		

		Ensure the camera's memory card is empy	If it is not: make sure there is a copy of the images on the PC hard drive-> delete all the images from the camera's memory card	
10	**Test**	Switch on the Kelsey controller and the control box	They have to stay on for at least 30 min prior to the LVDT reset step. This is because the instrumentation amplifiers need to warm up.	
		Accurately position the hydraulic actuator	Set the hydraulic actuator to be 0.1 mm above the loading beam	
		Set up the loading regime on the Kelsey controller	0.5mm/min: set gen-> test type: static | test mode: displ | test bias: set your target displacement (max = 70mm) | start/stop times -> static fade in -> time: set time in which the target displacement is to be reached | static fade out: how long it will take the actuator to return to the start position after the stop button is pressed (120s);	
		Check whether the instrumentation output is correct; check the calibration factors	If one of the DAQ devices is not responding: run NI MAX -> Devices and interfaces-> Choose your device-> self-test-> if it does not work, unplug and plug the usb cable	
		Check the LabView remote shutter	The usb cable must be unplugged for the shutter to work -> stop the LabView programme when finished	
		Switch off the ceiling lights		
		Take a benchmark image		
		Run the LabView programme	If the Kelsey controller and the control box were on for less than 25 min wait with this step	
		Inspect the load cell output	Observe for at least 3min. In case the output is not ~0 or the noise amplitude is > 5N: RESOLVE THIS BEFORE PROCEEDING WITH THE TEST	
		Reset the LVDTs in LabView		
		Lower the centring		
		Immediateley take a picture		
		Release the skewbacks if specified		
		Immediateley take a picture		

		Set up pictures to be taken automatically at 30 sec interval	Wait for at least 2 pictures to be taken before advancing to the next step	
		Start loading		
		Continue until large displacement	Press STOP on the Kelsey actuator to stop the test	
		Set the hydraulic actuator to -50mm -> then switch it off		
		Take pictures of the failure mechanism from the back side		
		Back up the calibration factors	Including the offset and gain set on the Kelsey controller	
		Back up the data	Copy the images to the PC hard drive; copy the images and sensor outputs to the external hard drive	
		Dismount the camera		
		Dismount the load cell	disconnect the cable -> move LMS away from the loading beam -> remove the load cell	
11	**Clean up**	Raise the centring		
		Remove the loading beam		
		Move the sand from the tank to the drum	Do not contaminate the sand in the drum with the arch joint material or with lumps of the silicone grease	
		Move the back glass wall to create a working space inside the tank	remove the duct tape from the back glass wall -> clean the alu bottom plate -> remove all the bolts -> raise the glass wall -> move it back -> lower it down	requires 2 people
		Check the outputs of the pressure sensors	DO NOT EXCEED 200 kPa! Complete the information on the broken sensors in the pressure sensors sheet	requires 2 people
		Clean the back glass wall		
		Lower the LVDTs		
		Disconnect the pressure sensors' cables		
		Remove and clean the voussoirs and the top parts of the abutments		

		Remove the centring from the tank		
		Remove the LVDTs from the tank	Place them in a bag under the rig	
		Secure the wires from the pressure cells	This is to prevent a short circuit	
		Clean the front glass wall		
		Clean the inside of the tank		

B. Test rig design drawings

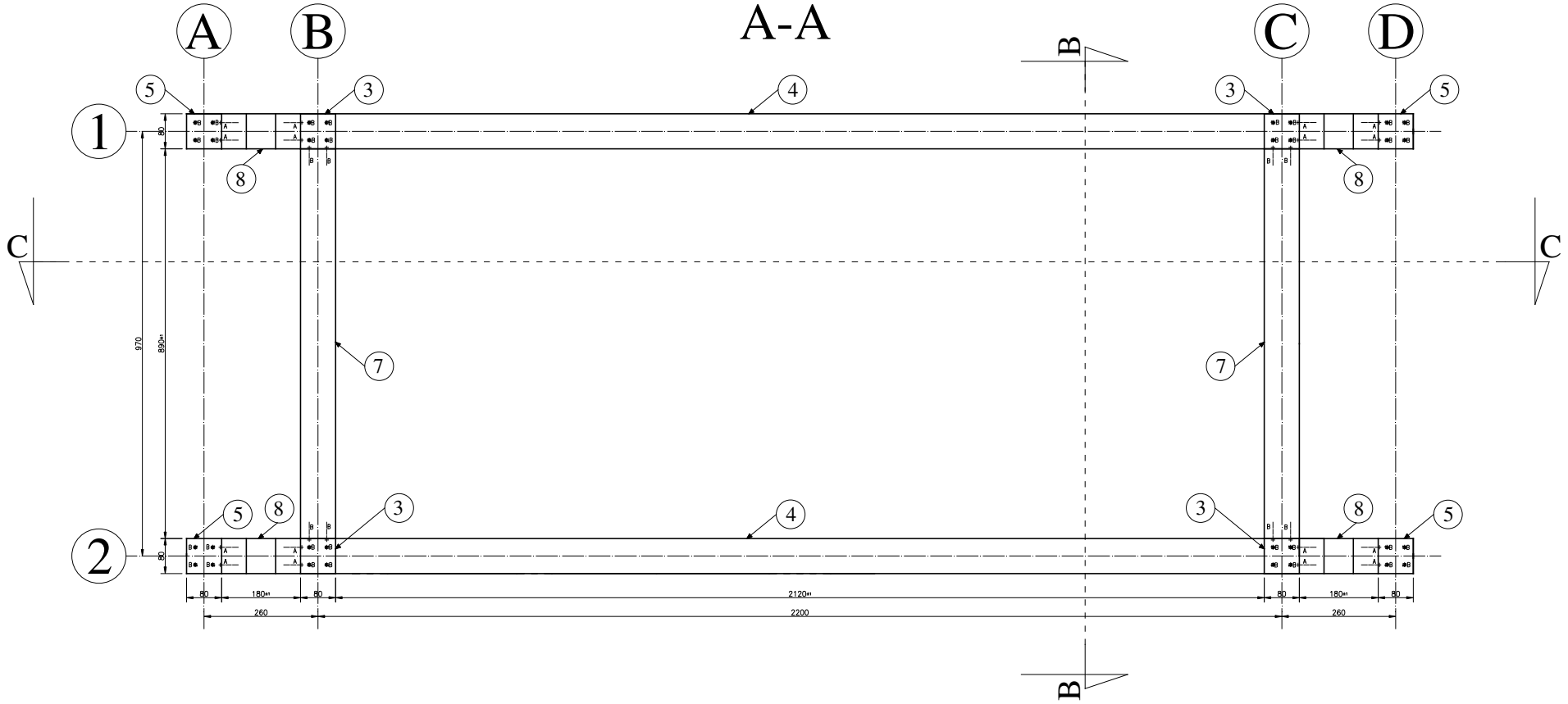

Title: Main frame: cross-section on A-A	
Designed by: Michal Pytlos	
Date: 17/01/2012	Drawing No. 1

B-B

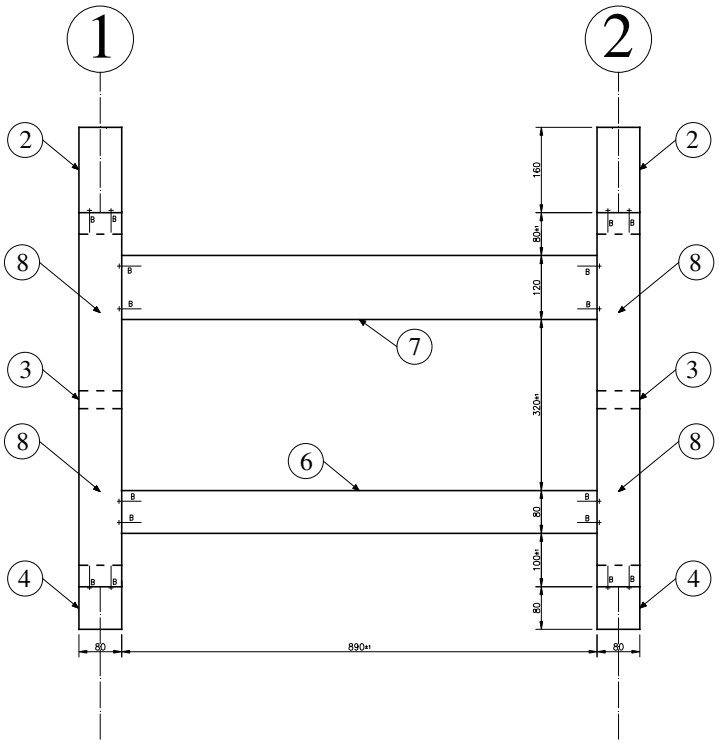

Item	Qty.	Description	Catalogue No.	Length [mm]
2	2	80x160	10.300	3160
3	4	80x80	10.240	700
4	2	80x80	10.240	2800
5	4	80x80	10.240	700
6	2	80x80	10.240	890
7	2	80x120	10.270	890
8	8	80x80	10.240	174.7*

Item	Qty.	Description	Catalogue No.
A	32	Angle Connector 40/80, 45°	093WS40245R
A	32	Angle Connector 40/80, 45° fixing set	
B	96	Bolt connector 80	
C	100	Nut 8 St M8 V Heavy	22.039.0
D	16	Angle Bracket 8 40x40	12.242.0
D	16	Angle Bracket Set 8 40x40	12.247.0
E	210	Nut 8 St M8 V	22.035.0

* approximate value

Title: Main frame: cross-section on B-B	
Designed by: Michal Pytlos	
Date: 17/01/2012	Drawing No. 2

C-C

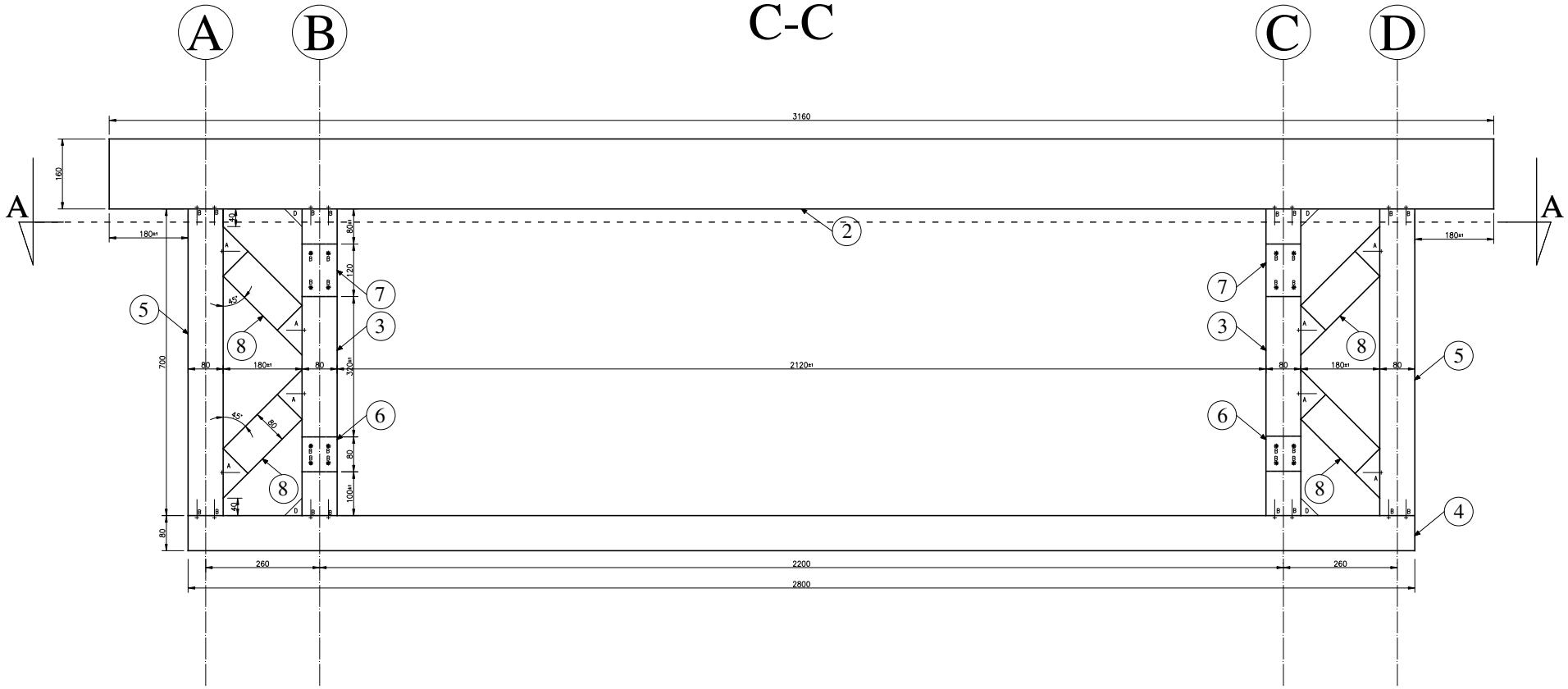

Title: Main frame: cross-section on C-C	
Designed by: Michal Pytlos	
Date: 17/01/2012	Drawing No. 3

C. Developed source code

The developed source code is available from: http://etheses.whiterose.ac.uk/